An *ab initio* approach to the historical modulation of cosmic rays

CP Wolmarans

orcid.org/0000-0003-0119-7354

Dissertation accepted in partial fulfilment of the requirements for the degree *Master of Science in Astrophysical Sciences* at the North-West University

Supervisor: Dr NE Engelbrecht

Graduation May 2021

25103695

An *ab initio* approach to the historical modulation of cosmic-rays

C. P. Wolmarans, B.Sc (Hons.)

Dissertation submitted in partial fulfilment of the requirements for the degree *Master of Science in Astrophysical Sciences* at the Potchefstroom Campus of the North-West University

Supervisor: Prof. N. E. Engelbrecht

November 2020

"The mystery of life isn't a problem to solve, but a reality to experience."
— Frank Herbert, Dune

Dedicated to Steven, Vera, Carma, my family and myself.

Abstract

The relationship between observed cosmic-ray intensities and the heliospheric magnetic field during the early space age is generally considered to be anomalous, relative to their relationship observed at later times. Various explanations for this behaviour have been proposed, but these do not take into account the influence of magnetic turbulence on the transport of cosmic-rays. The aim of this study is to take this into account, by analysing historic heliospheric magnetic observations in an appropriate manner to gain insight as to the behaviour of magnetic variances and correlation lengthscales during this period. These quantities are then used as inputs for an *ab initio* cosmic-ray modulation model, using theoretically-motivated expressions for cosmic ray diffusion and drift coefficients. Galactic cosmic-ray intensities computed with this model, when compared with neutron monitor observations, are found to be in qualitative agreement. From this it can be concluded that cosmic-ray modulation conditions during the early space age were not as anomalous as previously thought, and that it is essential to take turbulence into account in the study of historic cosmic-ray modulation.

Keywords: Cosmic-rays – Modulation – Turbulence

Abbreviations

The abbreviations used in this study are listed here. Most are also written in full when they first appear in each chapter, to remind the reader.

AU	Astronomical unit
CF	Correlation function
CR	Cosmic-ray
HCS	Heliospheric current sheet
HMF	Heliospheric magnetic field
MFP	Mean free path
NSE	Navier-Stokes equation
NM	Neutron monitor
PV	Partial variance
SSF	Second-order structure function
2D	Two-dimensional
3D	Three-dimensional

Contents

Chapter 1

Introduction

For most of the space age, a clearly anti-correlated relationship has been known to exist between the observed heliospheric magnetic field (HMF) magnitude and galactic cosmic-ray (CR) intensities, as observed at Earth via neutron monitors or in space, as function of changes in the solar activity cycle. One exception to this occurred at the very beginning of the space age, in the late 1960s during solar cycle 20. During this period, CR intensities behaved similar to those observed during other solar cycles (most notably during the 1980s), yet the observed HMF magnitude did not display its characteristic solar cycle dependent behaviour. During the 1960s, this quantity remained almost constant as function of time, and did not increase towards solar maximum like it did in the 1980s. The origin of this apparently anomalous behaviour has been the subject of much study, and various mechanisms have been proposed to explain it, ranging from variations in the dimensions of the heliosphere, to the action of particularly strong magnetic fields near the heliospheric termination shock [see, e.g., *Lockwood and Webber*, 1979; *Hatton*, 1980; *Exarhos and Moussas*, 1999; *Wibberenz et al.*, 2002]. These explanations, however, do not consider the influence of HMF turbulence on CR transport, which, through its influence on CR diffusion and drift coefficients, is known to be significant [see, e.g., *Caballero-Lopez et al.*, 2019; *Moloto and Engelbrecht*, 2020]. This study aims to investigate the influence of turbulence parameters on the transport of CRs in the 1960s, in an attempt to improve our understanding of the observed behaviour of the intensities of these particles relative to that of the HMF magnitude in this period.

To do so, spacecraft observations from this period need to be analysed. This task is rendered difficult due to the fact that such observations are typically of low resolution, and interspersed with many gaps. These characteristics do not lend themselves to analysis using the latest techniques employed in the study of HMF turbulence using more modern, high resolution data. Therefore, lower order data analysis techniques are used in this study to glean information as to turbulence quantities in the 1960s from existing data sets. These techniques are thoroughly tested using synthetic turbulence data, and their results are compared with analyses of similar data observed during the 1980s, so as to ascertain whether HMF turbulence during the 1960s was fundamentally different from turbulence during the 1980s. These results are then used as inputs for a set of diffusion and drift coefficients that have been successfully used to model the transport of CRs in numerical modulation models, to investigate potential differences in CR transport coefficients during these periods. Finally, these transport coefficients are used in the 3D stochastic CR modulation model of *Engelbrecht and Burger* [2015b] to compute CR intensities at Earth, which are compared with neutron monitor observations, to demonstrate whether the inclusion of more information as to HMF turbulence quantities would lead to computed CR intensities in qualitative agreement with the observed CR intensity profile as function of time.

This study is arranged as follows. In Chapter 2 a brief review of literature regarding the turbulent HMF and CR modulation, as well as an introduction to selected concepts relevant to the study of turbulence, is presented. The CR intensities and magnetic field measurements are shown together, and the period of interest to this study, as well as its break from the expected behaviour in terms of the relationship between the observed CR intensities and HMF magnitude, is discussed. The turbulence analysis techniques discussed in this Chapter are the second-order structure function (SSF) and the construction of partial variances (PV), that both provide a measure of the integrated power spectrum of turbulent fluctuations, and the two-point autocorrelation function (CF), as well as a CF based on the SSF, which can both be used to investigate the correlation lengthscale of turbulence. This chapter closes with a discussion of the results of selected previous studies devoted to the study of magnetic turbulence in the heliosphere.

Chapter 3 provides a preliminary analysis of turbulence quantities by use of synthetic data that allow for the investigation of the effects of data sparsity and resolution on the turbulence analysis techniques introduced in Chapter 2 and the reliability of the results that can be obtained from their application to historic spacecraft data with such limitations. This chapter also provides an investigation as to how the placement of omissions in such data-sets may effect turbulence analysis techniques. The chapter concludes with the discussion of the selection of the analysis techniques most appropriate for use in the rest of this study.

The turbulence quantities obtained by an appropriate turbulence analysis on historic spacecraft observations is presented in Chapter 4. Observations taken during the 1960s and during the 1980s are compared, motivated by the consideration that CR observations during both periods behaved in a similar manner, as opposed to observations of the HMF magnitude. These results and the methods by which they were obtained were presented at the 64th Annual Conference of the South African Institute of Physics. Furthermore, a detailed analysis of *Pioneer 6* and *7* observations is presented here. This analysis is motivated by the the fact that the periods of observation for both these spacecraft overlapped during the period of time of interest to this study.

Chapter 5 presents the effect on galactic CR transport coefficients made by the use of the turbulence quantities obtained in Chapter 4 and a comparison of the transport coefficients of the two $A < 0$ periods analysed there. These coefficients, and the turbulence quantities they are calculated from, are then used as inputs for a numerical CR modulation model. The galactic CR differential intensities so computed are then compared with neutron monitor observations

Finally, Chapter 6 briefly summarises the conclusions drawn from the results obtained in this study, some of which have been published in *Engelbrecht and Wolmarans* [2020].

Chapter 2

Cosmic-Ray Modulation from a Turbulence Perspective

2.1 Introduction

The heliosphere is the region dominated by all manner of effects of solar origin. The turbulent solar wind (SW) plasma flows outward to the furthest reaches of the heliosphere and carries the solar magnetic influence along with it. Charged particles originating inside and outside this domain encounter not only the outward steam of particles ejected by the the Sun, but also the heliosperic magnetic field (HMF) [see, e.g., *Quenby*, 1984; *Potgieter et al.*, 2001; *Kóta*, 2013; *Moraal*, 2013]. These particles, called cosmic-rays (CRs), experience changes in their motion and energy while traversing the heliosphere, the study of which is called the modulation of CRs. The transport of CRs in the heliosphere is influenced by magnetic diffusion and charged particle drift in the HMF, as well as the outward convection and adiabatic cooling of the expanding SW [e.g. *Kóta*, 2013]. The investigation of SW turbulence provides key inputs to diffusion and drift coefficients, and it is imperative to glean sufficient information on the conditions of the underlying turbulence of the SW in order to construct reliable CR modulation models [see, e.g, *Engelbrecht and Burger*, 2013; *Moloto and Engelbrecht*, 2020]. This chapter briefly outlines the concepts relevant to the transport of CRs throughout the heliosphere from a SW turbulence perspective, as well as a discussion of CR observations during the earliest period of spacecraft measurements. Special attention is given to the subject of turbulence to provide context for, and to introduce, the eventual calculation of turbulence quantities by the analysis techniques pertinent to this study.

2.2 The Solar Modulation of Cosmic-Rays

Here, cosmic-rays refer to charged particles traversing the heliosphere that are of galactic and solar origin, accelerated to high energies due to various processes [*Kallenrode*, 2001; *Caballero-Lopez et al.*, 2004b; *Balogh and Izmodenov*, 2005; *Agarwal and Mishra*, 2008; *Strauss et al.*, 2012a; *Moraal*, 2013; *Caballero-Lopez et al.*, 2019]. The name for these particles reflects their original conception as high energy photons until the confirmation that they were, in fact, charged particles (primarily atomic neuclei, such as protons) mostly of galactic origin. Today the topic of CRs is a subject allowing inquiry to the nature of the heliosphere and consists of the study of particles that reach the heliosphere from galactic and intergalactic sources, anomalous CRs accelerated to relevant speeds inside the heliosphere, solar energetic particles originating from the Sun and Jovian electrons coming from the magnetosphere of Jupiter [see, e.g., *Ferreira et al.*, 2001; *Strauss et al.*, 2017; *Vogt et al.*, 2018].

The discovery and observation of CRs is of great significance to the study of the heliosphere, in addition to the regions at which such particles are accelerated, both within and outside the Sun's influence. The existence of CRs of various and extreme energies allows insight to be gained about physical processes from which they are produced, as well as into new physics [e.g. *Lin et al.*, 2019; *Cuoco*, 2020]. Changes in CR intensity and their motions within the heliosphere allows direct observation of the Sun's influence on interplanetary space through the SW. It has been theorized that the Earth's weather may be affected by CRs entering the atmosphere as correlations between neutron monitor (NM) counts and cloud formation data have been seen, although recent studies [*Pierce*, 2017] have shown that the influence is weak. In addition to this, high energy CRs could conceivably be a health risk to astronauts and provide a barrier to the usefulness of refined electronics aboard spacecraft [see, e.g., *Schwadron et al.*, 2010].

Galactic CRs originate from outside the heliosphere and make up the majority of CR particles. Later in this study the term CR will be used when these particles are spoken of. This type of CRs is a population that ranges in energies up to the order of 10^{20}eV [e.g. *Kallenrode*, 2001], and such particles observed at energies ranging from a few MeV to a few 100GeV, according to *Jokipii and Kóta* [2000], experience modulation in the heliosphere. These types of CRs are thought to be accelerated by high energy phenomena, such as the shocks of supernovae remnants and pulsars. Galactic CRs fill local interstellar space quite uniformly and consist mainly of ionised atomic nuclei ($\sim$ 98%), with the rest being electrons, antiprotons and positrons ($\sim$ 2%) [e.g. *Kallenrode*, 2001; *Langner and Potgieter*, 2004; *Boschini et al.*, 2017]. Cosmic-rays of even higher energies are considered to be of extragalactic origin. Galactic CRs that enter the heliosphere encounter the turbulent SW and the embedded HMF in a manner that is described by the *Parker* [1965] transport equation [see, e.g., *Quenby*, 1984; *Moraal*, 2013], which will be discussed later in Chapter 5. Anomalous CRs are typically of lower energies and are pick-up ions accelerated to those energies upon encountering the termination shock [e.g. *Jokipii and Kóta*, 2000], while solar energetic particles are a CR species accelerated by solar flares [*Kallenrode*, 2001; *Reames*, 2020]. The intensity changes of CRs observed, or rather, the changes in their motion due to their interaction with the features of the heliosphere, is called the solar modulation of CRs [*Potgieter et al.*, 2014]. The processes encompassed by the study of CR modulation are: convection, adiabatic energy losses, diffusion and drift [*Potgieter and Ferreira*, 2001]. The modulation of CRs is dependent on the time-dependent behaviour of the solar influence-sphere, such as the solar activity cycle and thus the SW, the HMF and the heliospheric current sheet (HCS) [see, e.g., *Caballero-Lopez et al.*, 2019; *Moloto and Engelbrecht*, 2020]. Although the *Parker* [1958] transport equation, along with the various CR modulation mechanisms, will be discussed in more detail in Chapter 5, this chapter aims to briefly introduce observational aspects of time-dependent CR modulation relevant to this study.

2.3 The Sun and Heliosphere

The Sun is a G2V main-sequence type star of an approximate age of 4.6 billion years, with nuclear fusion processes as its source of energy [*Kallenrode*, 2001]. The solar core is where nuclear fusion occurs, this region is enveloped in the region where energy transport takes place radiatively; the aptly named radiative zone, followed by the convection zone and photosphere, which is the visible solar surface [*Kallenrode*, 2001]. Beyond the solar surface lie the chromosphere, transition region and corona that make up the solar atmosphere

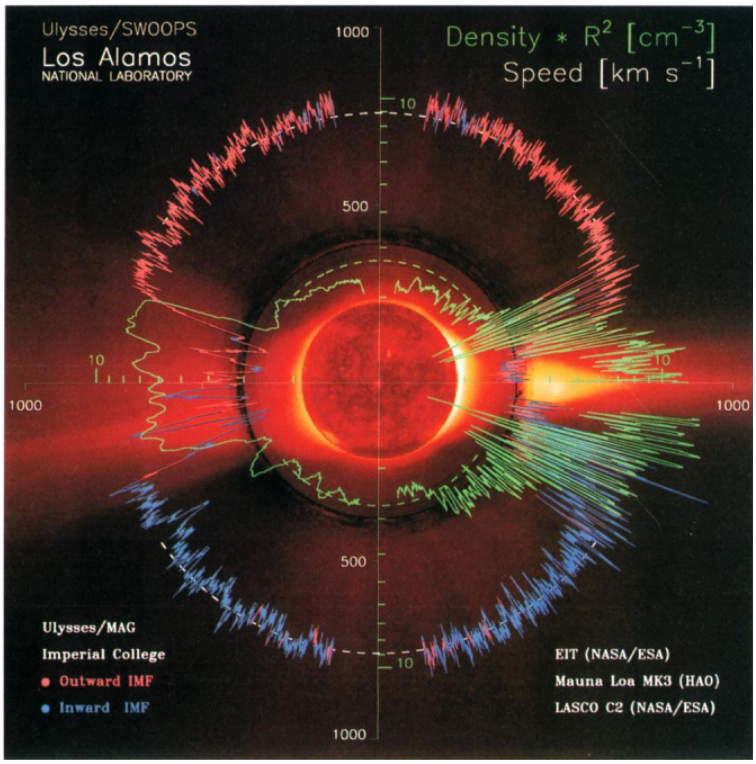

FIGURE 2.1: A representation of the results of the *Ulysses* spacecraft's first orbit showing latitude dependence of the SW speed and density, taken from *McComas et al.* [2000]. The image shows solar rotation averaged density of protons in green along with hourly averages of SW speed observations. The red and blue traces show SW speeds for outward and inward parts of the HMF, respectively, while the green traces show SW density.

[*Parker*, 1958; *Owens and Forsyth*, 2013]. The SW, originally called *solar corpuscular radiation*, is a charged particle plasma emerging from the solar corona due to the instability of the solar atmosphere. The mass lost from the Sun to the SW is supersonic and travels at around 400km/s radially outward in the equatorial plane [*McComas et al.*, 1998; *Kallenrode*, 2001; *Balogh and Izmodenov*, 2005]. The speed of the SW is not uniform with heliolatitude and may double (to around 800km/s) near the poles of the Sun. The fast solar wind emerges at the coronal holes of the Sun where open field lines dominate a region of the corona, SW plasma ejected here range in speeds between $\sim 400-800$km/s, while the slow SW ranges between $\sim 250-400$km/s and emerges near the Sun's magnetic equator [*Kallenrode*, 2001; *McComas et al.*, 2000; *Opher*, 2016]. The SW speed is also dependent on the Sun's ~ 11-year magnetic polarity cycle and activity, where the differential rotation of the solar surface causes magnetic effects that may cause events such as coronal mass ejections which can drastically influence SW plasma bulk speeds and composition [*Kallenrode*, 2001]. During conditions consistent with solar maximum the SW speed displays a more complex profile where alternating fast and slow SW speeds can be seen at all latitudes [*Meyer-Vernet*, 2007], while it displays a strong latitudinal dependence during solar minimum [e.g. *McComas et al.*, 2000], visible in Figure 2.1 taken from that study. The *Ulysses* spacecraft data show that the SW speed is largely constant all through the high-latitude SW observations, as opposed to the greater variation at low latitudes [see, e.g., *Phillips et al.*, 1995]. Figure 2.1 shows hourly averages of *Ulysses* SW speed observations with the red and blue traces indicating the outward and inward magnetic field polarities respectively. The green trace indicates SW density observations as described by *McComas et al.* [2000] and effectively shows that the SW density is low for regions of high SW speed and vice versa.

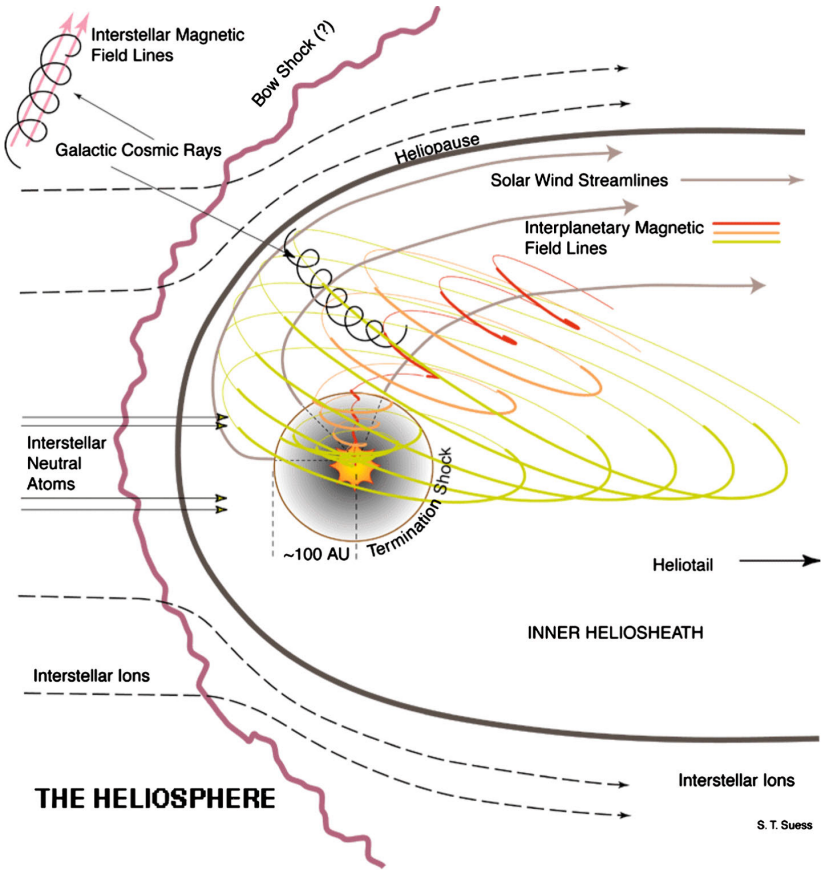

FIGURE 2.2: A basic illustration of the heliosphere and its features. SOURCE: Jet propulsion Laboratory (1999a), courtesy of S. T. Suess as taken from [*Opher*, 2016].

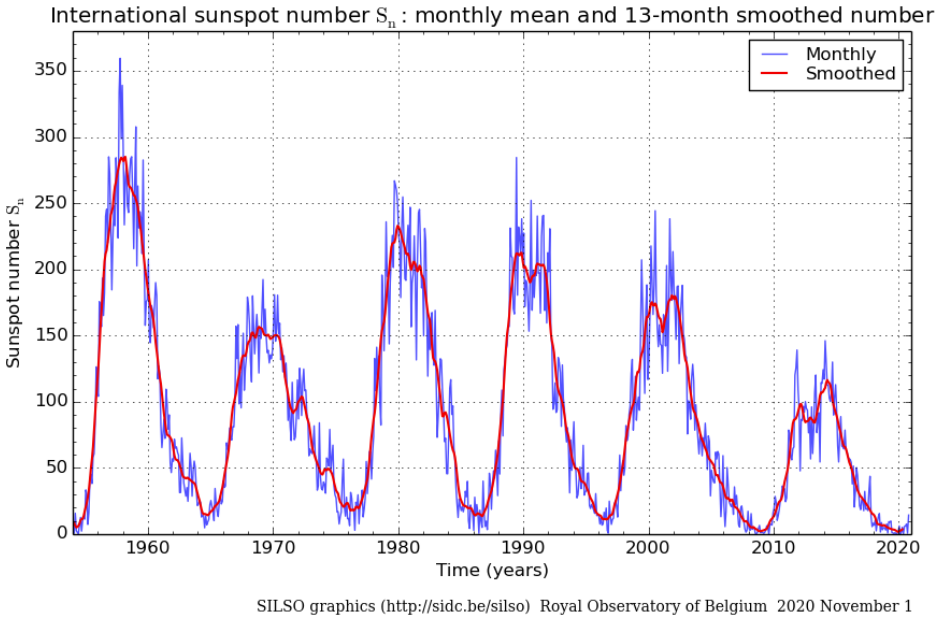

FIGURE 2.3: Mean monthly (blue) and 13-month smoothed (red) international sunspot numbers made available by *SILSO World Data Center*.

The Sun and heliosphere travel at a speed of around 26km.s^{-1} through the local interstellar medium, which interacts with particles of heliospheric origin and the HMF [*Balogh and Izmodenov*, 2005; *Potgieter et al.*, 2011]. The Sun's passage through this plasma causes its direct interaction with the radial SW. The outward push of the SW against the local interstellar medium forms a pressure balance, to some extent shielding the inner heliosphere from the inward flow of interstellar plasma. The heliosphere can be described as an asymmetrical bubble which is compressed in the forward direction, whilst the reverse is extended into a longer tail [*Potgieter et al.*, 2011; *Opher*, 2016; *Pogorelov et al.*, 2017]. The heliosphere comprises a few major features: the termination shock, the heliosheath, the heliopause and a possible bow shock. The termination shock is the region where the supersonic SW transitions to subsonic speeds [*Strauss et al.*, 2012b; *Opher*, 2016]. The SW plasma encounters the termination shock and is slowed, compressed and heated, which results in increased magnetic field measurements and plasma temperatures [see, e.g., *Richardson and Stone*, 2009; *Opher*, 2016]. The heliopause separates the warmer SW plasma and the cooler interstellar plasma [*Opher*, 2016]. The inner heliosheath is bound by the termination shock and the heliopause with the outer heliosheath the region beyond that [*Potgieter et al.*, 2011]. Figure 2.2 is an illustration of the features of the heliosphere, as discussed above, taken from *Opher* [2016]. The heliopause constitutes the end of the heliosphere beyond which lies a hypothesized bow shock or wave in the forward direction of the Sun's motion where interstellar plasma is thought to be compressed, the existence of which is still disputed [see, e.g., *Balogh and Izmodenov*, 2005; *Potgieter et al.*, 2011; *Strauss et al.*, 2012b; *Opher*, 2016; *Pogorelov et al.*, 2017; *Opher et al.*, 2020]. At all regions of the heliosphere the modulation of charged particles like galactic CRs occurs, but a detailed treatment of these regions is beyond the scope of this study.

2.4 The Heliospheric Magnetic Field and Solar Cycle Changes

The magnetic field within the heliosphere is a complex structure, one which is key to understanding the modulation of CRs. Some of the observable features on the photosphere of the Sun are called sunspots, which are visibly darker regions caused by intense local magnetic fields. These darker regions have localized reductions in temperature due to the local magnetic field strength limiting heat conduction. *Hale* [1908] observed that sunspots occur in pairs of positive and negative polarity, and in the northern hemisphere, are ordered along with the direction of the Sun's rotation, and that the ordering is inverse in considering the southern hemisphere. The number of sunspots varies with a mean period of ~ 11 years, and the magnetic polarities of binary pairs are reversed with each cycle. As sunspots are associated with the solar magnetic field, the conclusion was made that the solar magnetic field changes polarity every 11 years and has a mean period of oscillation of around ~ 22 years that switches around the period of highest solar activity [e.g., *Potgieter*, 2014; *Shen and Qin*, 2018; *Moloto and Engelbrecht*, 2020]. Figure 2.3 shows monthly mean and 13-month smoothed international sunspot numbers, produced by *SILSO World Data Center*, illustrating the times of high and low solar activity. Figure 2.4 shows monthly NM counts from various long term observations. Neutron monitor counts, representing the observed CR intensity at Earth, clearly show the 11-year cycle that is generally anti-correlated with solar activity, and therefore sunspot numbers, over the years. Figure 2.5 shows 27-day averaged magnetic field magnitudes that constitute the *OMNI* data-set which, upon comparison with Figures 2.3 and 2.4, clearly correlate with solar activity and are thus anti-correlated with NM observations.

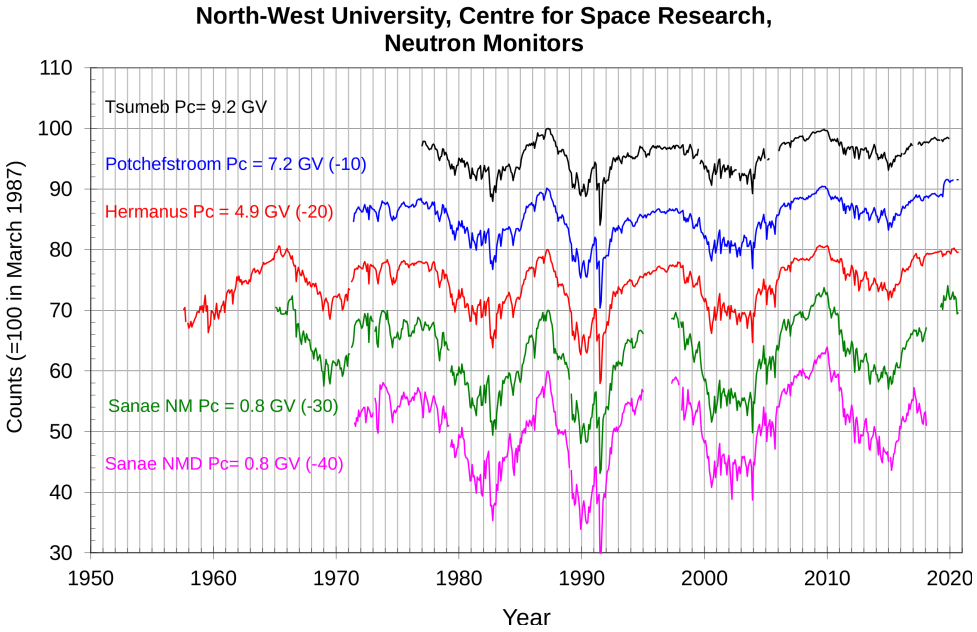

FIGURE 2.4: Various monthly averaged NM observations provided by the North-West University Centre for Space Research at http://natural-sciences.nwu.ac.za/neutron-monitor-data.

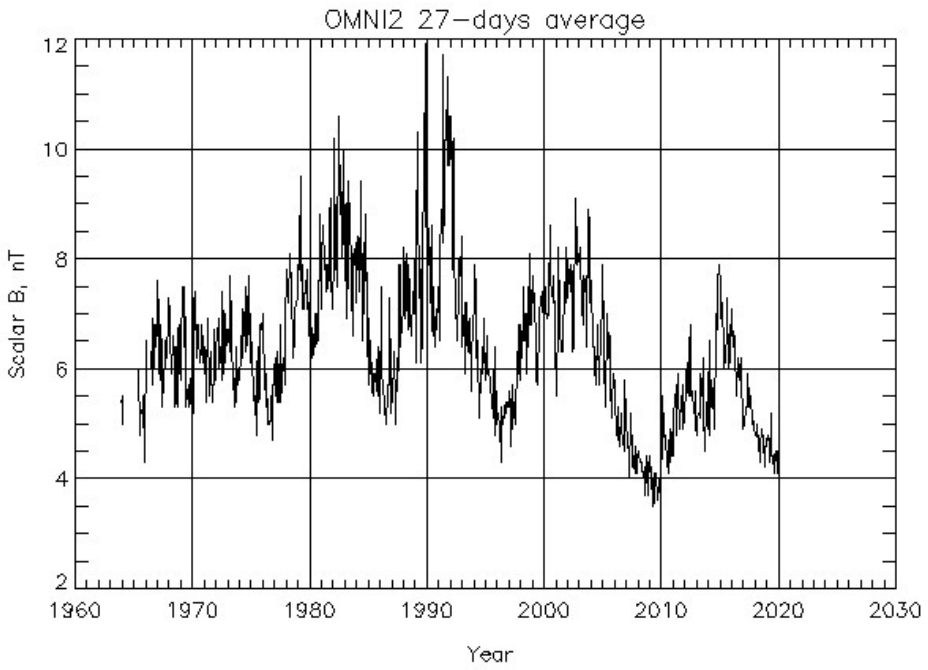

FIGURE 2.5: 27-day averaged magnetic field magnitudes, as observed by participant spacecraft of the *OMNI* data collection, available at https://omniweb.gsfc.nasa.gov/.

Parker [1958] derived the earliest and most basic model of the HMF. In heliocentric spherical coordinates the Parker field is [see, e.g., *Smith*, 2001; *Krüger*, 2005; *Engelbrecht*, 2008; *Nel*, 2015],

$$\mathbf{B} = A\left(\frac{r_e}{r}\right)^2 \left[\mathbf{e}_r - \frac{\Omega(r - r_{ss})}{V_{SW}} \sin\theta \mathbf{e}_\phi\right], \tag{2.1}$$

where $|A|$ is the magnetic field magnitude at earth, r_e and r_{ss} are heliocentric distances to Earth (1AU) and the source surface location respectively, V_{SW} is the solar wind speed and Ω is the solar rotation rate when the assumption is made that the Sun rotates rigidly between the inner solar corona and the Alfvén radius at which the plasma β (ratio of thermal and magnetic pressures [*Bieber et al.*, 1994]) exceeds unity. The source surface is set up to be the surface of origin for the Parker field and is assumed to be where the field is radial in the high corona. Spherical symmetry of the SW outflow is also assumed, along with an alignment of solar magnetic and rotational axes. The solar magnetic polarity is indicated by the sign of A for which a positive sign corresponds to an outward field direction in the northern hemisphere and inward in the southern hemisphere, with the opposite being true for a negative sign. These coordinates are obtained from the SW velocity in a rigid co-rotating frame of reference, such that [*Krüger*, 2005; *Engelbrecht*, 2008; *Nel*, 2015],

$$\mathbf{U} = V_{SW}\mathbf{e}_r - \Omega(r - r_{ss})\sin\theta\mathbf{e}_\phi, \tag{2.2}$$

In this configuration, since the HMF is frozen into the SW, the SW velocity and field lines are parallel, causing the theta component of the field to be zero, leading to Eq. 2.1. By $\mathbf{B} \times \mathbf{U} = 0$, then

$$B_\phi = -B_r \frac{\Omega(r - r_{ss})}{V_{SW}} \sin\theta, \tag{2.3}$$

and,

$$\tan\psi = -\frac{B_\phi}{B_r} = \frac{\Omega(r - r_{ss})}{V_{SW}} \sin\theta, \tag{2.4}$$

which introduces the winding angle or Parker spiral angle so that the Parker field is then

$$\mathbf{B} = A\left(\frac{r_e}{r}\right)^2 \left(\mathbf{e}_r - \tan\psi\mathbf{e}_\phi\right), \tag{2.5}$$

and is graphically illustrated in Figure 2.6, with the Sun at the center and different coloured lines representing different initial latitudes. The field lines are essentially spirals on cones of constant latitude. Other, more complex models for the HMF exist, such as Fisk and Fisk-Parker hybrid fields [see, e.g., *Fisk*, 1996; *Schwadron*, 2002; *Burger et al.*, 2008; *Hitge and Burger*, 2010; *Steyn and Burger*, 2020], but the introduction of the Parker field is sufficient for the purposes of this study.

The solar magnetic axis varies with solar cycle. The angle at which it is misaligned relative to the Sun's rotational axis is called the tilt angle and its behaviour correlates positively with solar activity. The change in tilt angle warps the largest feature of the heliosphere, the heliospheric current sheet (HCS). Along the HCS the HMF changes direction and the gradient that forms across it causes current to flow, which is where the feature gets its name. Figure 2.7 shows the variation in solar tilt angle as the maximum inclination of the HCS from 1975 to the present. The tilt angle is clearly dependent on the level of solar activity, as shown by 2.7, with larger tilt angles causing a complex current sheet structure, whereas solar minimum conditions provide very small tilt angles and simpler structures observed

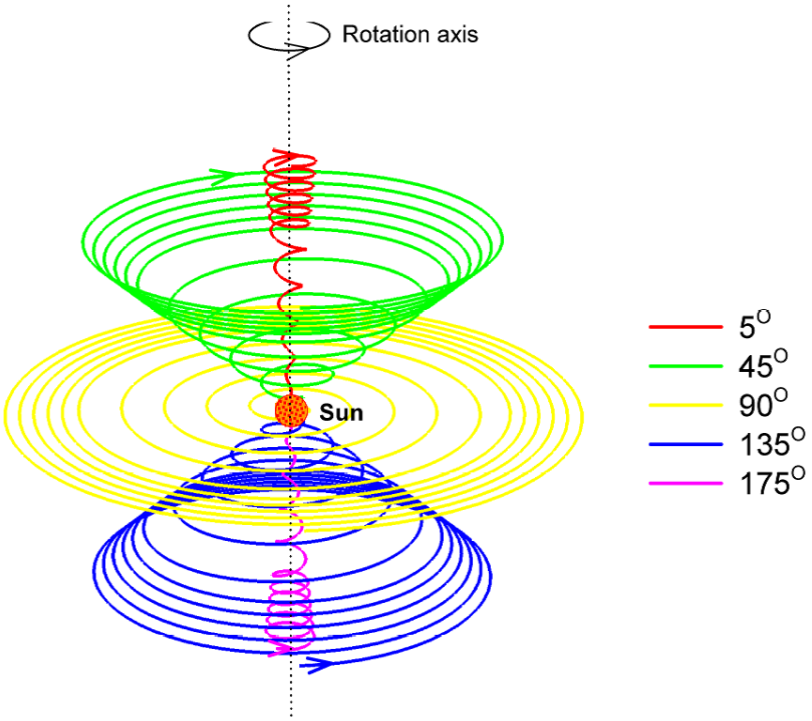

FIGURE 2.6: A representation of the Parker heliospheric magnetic field for an $A > 0$ polarity cycle and various polar angles, taken from *Manuel* [2013]. Here the field lines tighten as they move outward representing the slowed SW beyond the termination shock assumed to be around 90AU [*Richardson and Stone*, 2009]. It should be noted that the Parker field's radial component scales as r^{-2} while the azimuthal component scales as r^{-1}, implying tighter winding of field lines with radial distance.

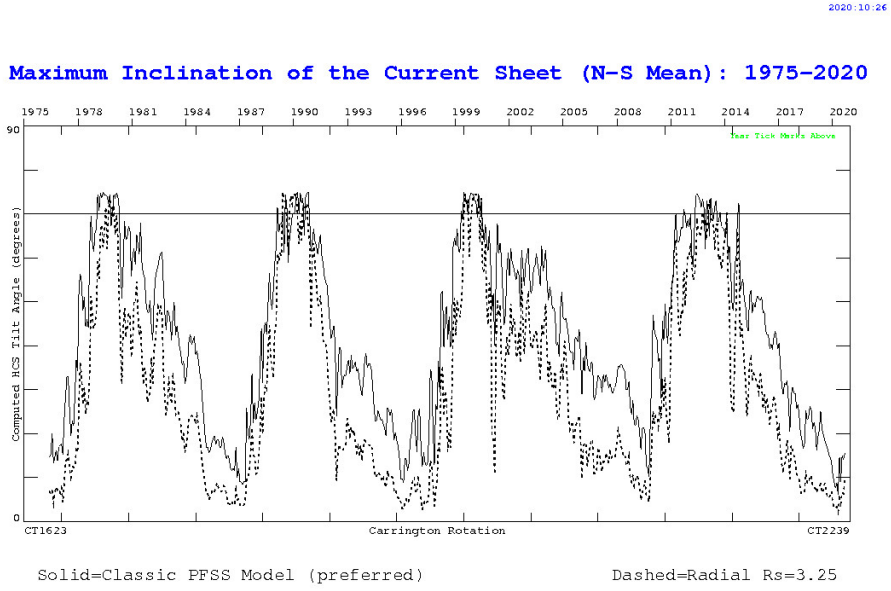

FIGURE 2.7: Solar magnetic axial tilt angles with solar cycle, that are observed to be high at solar maximum conditions, produced by *Hoeksema* [1992] and available at `http://wso.stanford.edu/`.

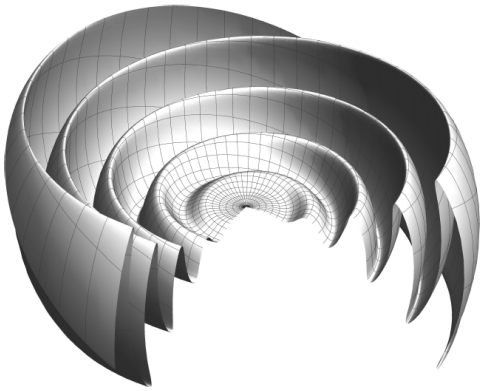

FIGURE 2.8: Heliospheric current sheet representation with tilt angle 20^o at around 30 AU with a cut-out to display the waviness of this structure [*Moloto*, 2015].

for the current sheet [see, e.g., *Smith*, 2001]. In CR modulation models, the HCS is often modelled as function of tilt angle α, using [see, e.g., *Jokipii and Thomas*, 1981; *Kota and Jokipii*, 1983; *Burger et al.*, 2008; *Raath et al.*, 2015]

$$\theta = \frac{\pi}{2} - \tan^{-1}\left[\tan\alpha \sin\left(\frac{\Omega r}{V_{SW}}\right)\right]. \tag{2.6}$$

again in heliocentric spherical coordinates and using the same variables as in the Parker field equations. Figure 2.8 illustrates the three-dimensional structure of the HCS and its waviness, as calculated using Eq. 2.6 by *Moloto* [2015] for a tilt angle of 20°, which corresponds to a intermediate level of solar activity. During solar minimum, the current sheet will be considerably flatter.

2.5 The CR-B Relation in the Early Space Age

Figure 2.9 shows monthly NM counts from Hermanus plotted with 27-day averaged HMF magnitudes from the *OMNI* data collection. The vertical blue lines form pairs that signify the 12-month period surrounding the accepted minimum months as taken from *Hathaway* [2015]. In NM data such as in Figure 2.9 there are sharp peaks followed by flat-topped increases following a 22-year alternation between them. The sharp peaked regions correspond to $A < 0$ solar magnetic polarity epochs, where positively charged particles drift inward along the HCS and outward at the poles, and the flat-topped ones to $A > 0$ epochs, where positive charged particles drift inward at poles and outward along the current sheet [*Reinecke and Potgieter*, 1994; *Le Roux and Potgieter*, 1995; *Jokipii and Kóta*, 2000; *Potgieter and Ferreira*, 2001; *Strauss et al.*, 2012b; *Potgieter*, 2014; *Moloto and Engelbrecht*, 2020]. The difference between the epochs seen in the data is interpreted as a result of drift and tilt variation in the HCS, for $A < 0$ positive particles flow in along the current sheet and are influenced by its wavy nature, whilst for $A > 0$ the particles drift inward at the poles and have their motion unaffected by the waviness of the HCS [e.g., *Kota and Jokipii*, 1983], forming flat-topped temporal profiles as in Figure 2.9. Current sheet drift is a major influence in time-dependent modulation during solar minimum conditions, due to alterations in the HCS in $A < 0$ cycles, while drift becomes less influential towards solar maximum [e.g., *Manuel et al.*, 2014; *Engelbrecht et al.*, 2019].

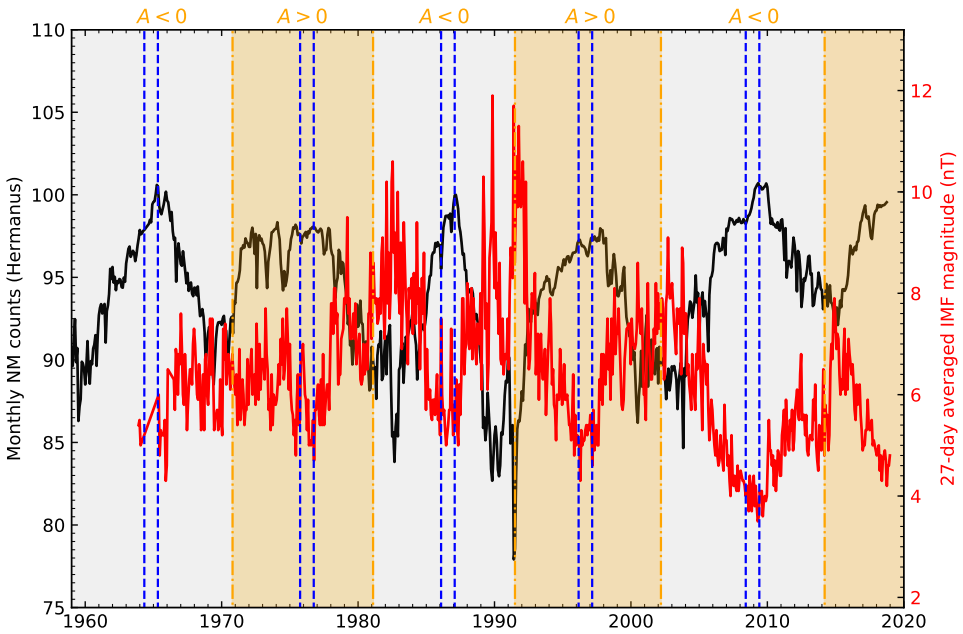

FIGURE 2.9: Monthly NM counts and 27-day averaged magnetic field magnitudes. With NM data taken from the NWU website: `http://natural-sciences.nwu.ac.za/neutron-monitor-data` and HMF data taken from *OMNI* (`https://omniweb.gsfc.nasa.gov/`).

The monthly NM counts displayed in Figure 2.9 are accompanied by 27-day averages of magnetic field magnitudes taken from *OMNI* data, so both correspond to behaviour at ~ 1AU. The anti-correlation between energetic particle counts by NMs and solar activity, mentioned before, is clearly displayed over the last few solar cycles in Figure 2.9. This anti-correlation is however not apparent in the earliest period of these spacecraft data observations and this behaviour is generally regarded as atypical [*Ahluwalia*, 2000; *Agarwal and Mishra*, 2008; *Caballero-Lopez et al.*, 2019]. During the 1960s the spacecraft data show a near consistent magnetic field magnitude at Earth, while the NM counts show the behaviour expected during a period of negative heliospheric polarity ($A < 0$) between the mid 1960s and mid 1970s (solar cycle 20), when compared to the more typical, anti-correlated behaviour observed between the mid 1980s to mid 1990s (solar cycle 22). Possible explanations of this behaviour have been proposed by many over the years. *Exarhos and Moussas* [1999] postulated that the magnetic fields at the termination shock were elevated during the period between the mid 1960s and mid 1970s which then had a greater role in CR modulation [see also *Ahluwalia*, 2000; *Agarwal and Mishra*, 2008]. *Hatton* [1980] simulated observed CR intensity through the number of important solar flares observed during that period and relate the behaviour to changes in the dimensions of the heliosphere. The force field approach of [*Gleeson and Axford*, 1968] was used by *Lockwood and Webber* [1979] to relate modulation effects observed between the mid 1960s and mid 1970s to alterations in the effective diffusion coefficient for CRs. *Wibberenz et al.* [2002] postulated slower transition between solar magnetic polarity in solar cycle 20 and relate the deviation from the expected CR-B relation to drift effects. The current study aims to investigate this early period in terms of turbulence quantities that directly influence CR transport coefficients [e.g. *Schlickeiser*, 2002; *Shalchi*, 2009, 2020a], to ascertain their influence on the transport of CRs.

2.6 Early Spacecraft Observations

The spacecraft measurements of the HMF relevant to this study are the compound *OMNI* data-set and those of the *Pioneer 6* and *7* [*Corliss*, 1972; *King and Papitashvili*, 2005] magnetometer experiment (available at `https://omniweb.gsfc.nasa.gov/`). These data-sets feature observations as far back as the mid 1960s and at or near 1AU. Early observations of the SW are characterised by the presence of data omissions and are typically of low resolution when compared to modern-day spacecraft data collections. These characteristics present a challenge for more refined techniques better suited to modern data-sets, and as such the effects of these two properties will need to be quantified in the context of the turbulence analysis techniques presented later in this chapter, before they are applied to spacecraft data. *Fraternale et al.* [2016] give several reasons for the presence of omissions in *Voyager 2* data, such as interference from other instruments, tracking gaps due to the spacecraft's position, temporary errors in the measurement of data, and re-positioning or alterations in trajectory of the spacecraft. Although these reasons might not precisely explain the features of early space age observations, they nevertheless provide insight as to potential reasons for these gaps. Regardless, any analysis of the observations is hampered by their low, usually hourly, resolution and the fact that they display large observational gaps. The available *Pioneer* data are hourly averaged magnetometer measurements that seem to follow a trend of 10 hours of observations followed by a gap of several days. The *OMNI* data is a collection of observations near 1AU, taken from several different spacecraft, while *Pioneer 6* and *7* were at average heliocentric distances of 0.88AU and 1.06AU respectively during observations. The overlapping portion of available *Pioneer 6* and *7* data, along with *OMNI* data from the same span of time, may yield further insights as to what was happening near Earth at different radial distances and longitudes. In what is to follow, to compare the results of *OMNI* and *Pioneer* data, the same resolution of 1 hour measurements will be used later in Chapter 4.

2.7 Turbulence

The physical phenomenon of turbulence in the context of fluid dynamics can be described as the continual decomposition of eddies or vortices into smaller ones, which typically persists until energy becomes dissipated due to fluid viscosity at sufficiently small scales [*Batchelor*, 1953; *McDonough*, 2007; *Ditlevsen*, 2010]. Turbulence is disorganized behaviour which facilitates rapid diffusion and dissipation throughout fluids/gases and is typically observed in fluids of low viscosity and high flow rates [*McDonough*, 2007; *Davidson*, 2015]. According to *Frisch* [1995] the motions governing turbulence should be implicitly included in the Navier-Stokes equation (NSE) which generally describes the motion of fluids [see, e.g., *Foias et al.*, 2001; *Zank*, 2014]. For ordinary fluids under no external forces, the general form of the NSE is then

$$[\delta\vec{u}/\delta t + (\vec{u}\cdot\nabla)\vec{u}] = -\nabla p + \nu\nabla^2\vec{u} \tag{2.7}$$

where p, ν and $\vec{u}$ are the fluid pressure, kinematic viscosity coefficient and fluid velocity respectively [*Frisch*, 1995]. A fluid's resistance to shear flow is represented by the dynamic viscosity μ and is proportional to the product of shear stress and the strain rate. The ratio between the dynamic viscosity and the density of the fluid is then the kinematic viscosity (ν) in Eq. 2.7.

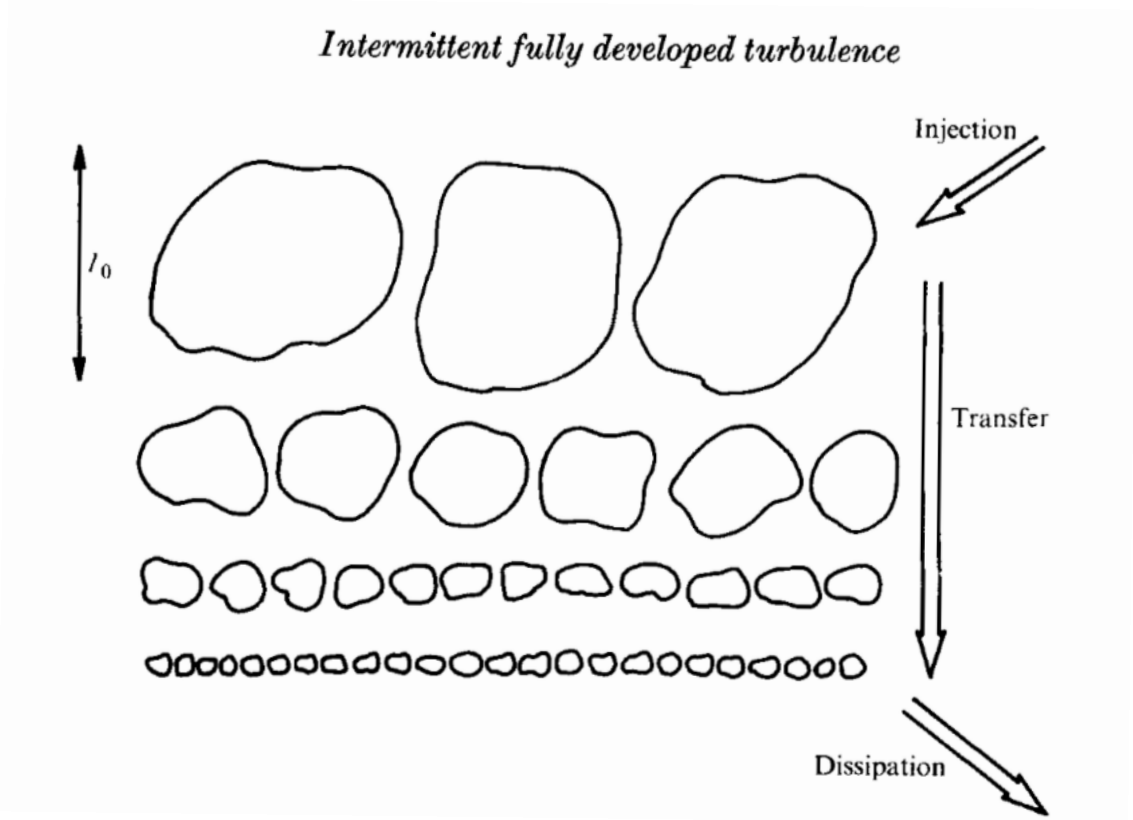

FIGURE 2.10: Diagram representing the sequential energy transfer from large to small scale structures and its accompanying phases. Energy injected at large scales causes the formation of substructures that progressively fragment into smaller structures. At intermediate scales, inertial forces dominate the transfer of energy, before the eventual dissipation at sufficiently small scales [*Frisch*, 1995].

The Reynolds number is the ratio between the inertial and viscosity terms of Eq. 2.7. High degrees of turbulence are associated with fluids of high Reynolds numbers [*Frisch*, 1995; *McDonough*, 2007; *Zank*, 2014; *Davidson*, 2015]. Through dimensional analysis, the Reynolds number can then be given as

$$[(\vec{u}\cdot\nabla)\vec{u}]\cdot[\nu\nabla^2\vec{u}]^{-1}\sim UL/\nu\equiv Re, \tag{2.8}$$

where U is the characteristic velocity or flow velocity of the fluid and L a typical or characteristic length scale [*Frisch*, 1995; *Davidson*, 2015; *Zank*, 2014]. For a fluid of a consistent viscosity at high characteristic velocity, or one of negligible viscosity for a given characteristic length scale, the dimensionless Reynolds number grows large and approaches infinity. Observations from turbulence experiments relate fluids of higher Reynolds numbers to higher degrees of erratic and turbulent behaviour. At extreme Reynolds numbers certain statistical symmetries are established and fully developed turbulence is thus observed in fluids of sufficiently large values of Re [*Frisch*, 1995]. The application of fluid turbulence to magnetohydrodynamic (MHD) flows then relates to SW turbulence [*Matthaeus and Velli*, 2011; *Bruno and Carbone*, 2013; *Zank et al.*, 2018]. The description by *Matthaeus et al.* [2012] of MHD turbulent plasmas is then that of conductive fluids and gasses that can be influenced by electromagnetic and mechanical forces. *Matthaeus et al.* [2012] show that the introduction of a Lorentz force term to the NSE, provided above, allows for the calculation of a magnetic Reynolds number. The SW, discussed in Section 2.3, is a turbulent plasma

with a fluctuating magnetic field [*Matthaeus et al.*, 2012; *Bruno and Carbone*, 2013]. The magnetic field observations made by different spacecraft have long been used to study SW turbulence [see, e.g., *Hedgecock*, 1975; *Matthaeus and Goldstein*, 1982; *Bruno and Carbone*, 2013].

According to *Davidson* [2015] in order to build an understanding of the phenomenon of turbulence, investigation as to the statistical properties inherent to turbulence observations, is required. Furthermore, it is clear by what has been presented here, that turbulence is inherently involved with the transfer of energy between large and small scales. The progressive energy transfer from large scale structures to smaller ones within a fluid is referred to as the energy cascade of turbulent flows [*McDonough*, 2007; *Davidson*, 2015]. In rare situations the flow from small to large scale structure can be observed, but this will not be considered in this study [*McDonough*, 2007]. Energy injected into a fluid produces large scale disturbances which propagate and proceed to transfer energy to undisturbed regions within the fluid, causing smaller disturbances there. A diagram of this process is shown in Figure 2.10 where an injection phase sees external energy being added to the fluid causing large eddies to form that lose their energy to smaller eddies as they break. At intermediate scales, the forces between eddies are purely inertial and function to further the transfer of energy to even smaller structures, but no additional energy is added at these scales. From Eq. 2.8, at length scales small enough that the viscosity begins to dominate the flow, there is a rapid dissipation of energy from the system, which usually ends up in the form of heat [*Ditlevsen*, 2010; *Davidson*, 2015].

For fluid turbulence, the flow velocity $\vec{u}(x,t)$ as function of position and time can be considered to be a combination of a fluctuating component and a uniform background quantity [e.g. *Davidson*, 2015]. In the rest of this section angle brackets will denote a suitable average of a variable. If the uniform background flow velocity in a fluid is given by $\vec{u}_0(x,t)$, so that $\langle \vec{u}(x,t) \rangle = u_0$, and the fluctuating component is $\vec{u}'(x,t)$ so that $\langle \vec{u}'(x,t) \rangle = 0$, then

$$\vec{u}(x,t) = \vec{u}_0(x,t) + \vec{u}'(x,t). \tag{2.9}$$

According to *Frisch* [1995] if $\langle \vec{u}'(x,t) \rangle = 0$, then $R_{ij}(\vec{r}) = \langle \vec{u}'_i(\vec{x})\, \vec{u}'_j(\vec{x}+\vec{r}) \rangle$ is the correlation function (CF) for spatial fluctuations. This function relates the spatial correlation between two fluctuating components separated by $\vec{r}$ [*Davidson*, 2015]. When $\vec{r} = 0$ and, when considering only one fluctuating component of the flow velocity, the CF simply becomes the variance of the fluctuating component, so that $R_{ii}(0) = \delta \vec{u}_i^2$ [see, e.g., *Matthaeus et al.*, 1999; *Engelbrecht*, 2013; *Davidson*, 2015]. For the solar wind as an MHD turbulent plasma, Eq. 2.9 in terms of the turbulent magnetic field, is then the composition of the uniform background field B_0 and the fluctuating component $\delta\mathbf{B}$. In a right-handed Cartesian coordinate system, and for a uniform component assumed to be along the z-axis, the turbulent magnetic field can then be written as [see, e.g., *Bieber et al.*, 1994; *Engelbrecht*, 2008; *Nel*, 2015]

$$\mathbf{B}(x,y,z) = B_0 \mathbf{e}_z + \delta\mathbf{B}(x,y,z). \tag{2.10}$$

In considering the characterization and study of fluctuations in the solar wind, HMF turbulence has been observed to be a superposition of a dominant non-propagating two-dimensional (2D) fluctuating component and propagating Alfvénic fluctuations, referred to as the slab component [see, e.g., *Matthaeus et al.*, 1990; *Bieber et al.*, 1994; *Zank*, 2014]. The combination of 2D and slab turbulence models can then be used to describe turbulent fluctuations transverse to the uniform background field. This combination is then

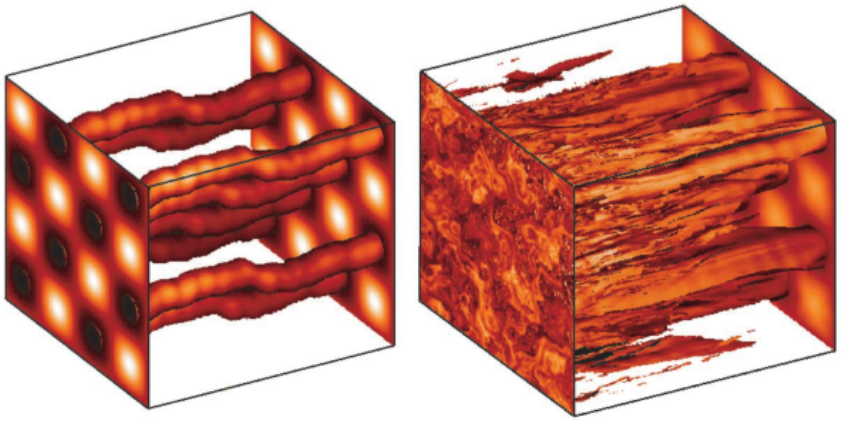

FIGURE 2.11: Slab and composite turbulence models of magnetic flux surfaces, on the left- and right-hand, respectively, taken from *Matthaeus et al.* [2003]. The composite model, which has a 80/20 contribution from 2D and slab turbulence energy, shows much more complexity in the direction transverse to the field and nearby field lines separate rapidly.

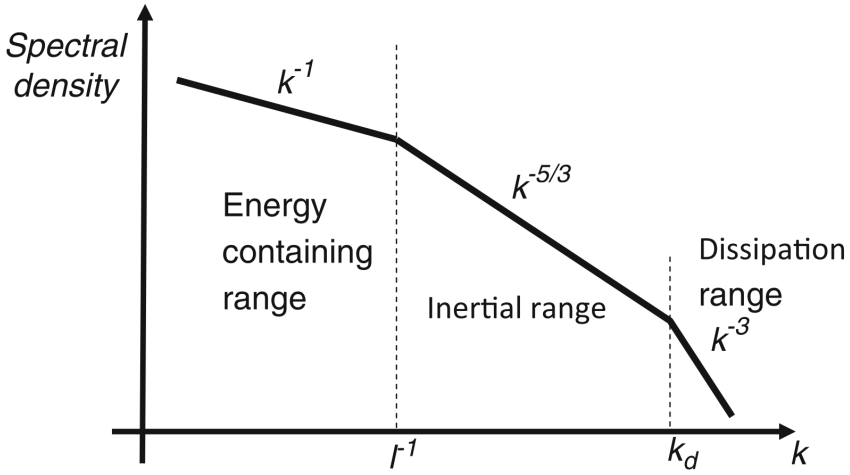

FIGURE 2.12: Schematic representation of the turbulence power spectrum, taken from *Zank* [2014].

$$\delta\mathbf{B}(x,y,z) = \delta\mathbf{B}_{2D}(x,y) + \delta\mathbf{B}_{slab}(z), \tag{2.11}$$

where subscripts '2D' and 'slab' denote 2D and slab turbulence quantities throughout this study. The slab turbulence term of Eq. 2.11 results from a one dimensional turbulence geometry where field fluctuations are a function of the z-coordinate along the background field, and remain unaffected by changes in the xy-plane. Therefore, since the fluctuating component only changes along z, flux tubes originating at specific (x, y) coordinates are well behaved as they propagate along the z-axis. This can be seen in the left panel of Figure 2.11, taken from *Matthaeus et al.* [2003], who plot such flux tubes in the presence of pure slab, and composite slab/2D turbulence (right panel). For 2D turbulence, where fluctuations are functions of coordinates x, y tranverse to z, the coherent motion of the flux tubes is quickly lost, and they experience significant 'shredding'. Solar wind turbulence at Earth has been observed to be anisotropic. That is to say, more power resides in the 2D fluctuations than in the slab fluctuations [see, e.g., *Bieber et al.*, 1996; *Oughton et al.*, 2015],

with corresponding differences in correlation lengthscales [e.g. *Weygand et al.*, 2011]. This anisotropy may vary as function of position in the heliosphere as well [e.g. *Oughton et al.*, 2011; *Adhikari et al.*, 2017].

The Fourier transform of the CF results in the turbulence power spectrum, a tool commonly used to understand the turbulent energy cascade. When integrating the power spectrum over over all frequencies, the total variance of the fluctuating component is returned [e.g. *Matthaeus et al.*, 2007a],

$$\int_0^\infty E(f)\,df = \delta B_T^2. \tag{2.12}$$

Figure 2.12, taken from *Zank* [2014], illustrates the typical behaviour of power spectra for HMF fluctuations and shows that they are divided into ranges, bounded by various scales [see also, *Goldstein et al.*, 1995]. Since these spectra can be in terms of frequency or wavenumber, which relate to temporal and spatial scales, and since $f \propto k \propto l^{-1}$, this implies that low wavenumber fluctuations represent large structures [*Frisch*, 1995; *Zank*, 2014; *Davidson*, 2015]. The turbulence power spectrum is related to the energy cascade in Figure 2.12 which shows that it can in general be divided into the ranges discussed for Figure 2.10 [*McDonough*, 2007; *Zank*, 2014]. Here, at low wavenumbers, external energy is injected and the power spectrum shows a spectral index of -1 in the energy containing range. Beyond this range, which ends at a wavenumber that corresponds to the turnover scale, the successive transmission of energy is done solely by inertial interactions. *Kolmogorov* [1941] showed, for high Reynolds numbers, that $\langle(\Delta u(l))^2\rangle$ (the mean of the squared fluctuating components), separated by the spatial scale l, is approximated by a $l^{2/3}$ power-law. Dimensional analysis shows a $k^{-5/3}$ law over the inertial range for the power spectrum of turbulence in this range [*Kolmogorov*, 1941; *Frisch*, 1995; *Oughton et al.*, 2006; *Zank*, 2014]. Finally, when fluid turbulence is considered, at sufficiently large wavenumbers in Figure 2.12 the viscosity of the fluid dominates, dissipating energy from the fluid in the form of heat [*Goldstein et al.*, 1995; *Leamon et al.*, 2000]. According to *Engelbrecht and Strauss* [2018], when concerned with plasma turbulence, wave-particle interactions can also act to dissipate energy. Figure 2.13 shows the turbulence power spectrum for HMF observations at Earth, complete with spectral indices for energy containing scales (-1) and the inertial range ($-5/3$) that show the values and shape as expected from Figure 2.12. There is a rapid decline of the spectrum at the highest frequencies in the figure, due to the time resolution of measurements. There are, however, spacecraft that allow for the investigation of the high frequency dissipation range [*Smith et al.*, 2006]. For more information on observations of turbulence in the SW, the interested reader is invited to consult, e.g., *Matthaeus and Velli* [2011], and *Bruno and Carbone* [2013].

2.8 The Calculation of Turbulence Quantities from Spacecraft Data

This study is concerned with the conditions of turbulence in the SW during the earliest periods of spacecraft observations of the SW. The primary reason for investigating turbulence conditions in this early period is the eventual study of CR modulation during this time. Various turbulence quantities are inputs for scattering theories that allow one to model CR diffusion and drift effects, which are the primary mechanisms by which the HMF influences the trajectories of galactic CRs. This section aims to introduce techniques relevant and useful for ascertaining turbulence quantities from early space age observations, introducing the limitations of early spacecraft data and evaluating what can be expected using current analysis techniques in the literature.

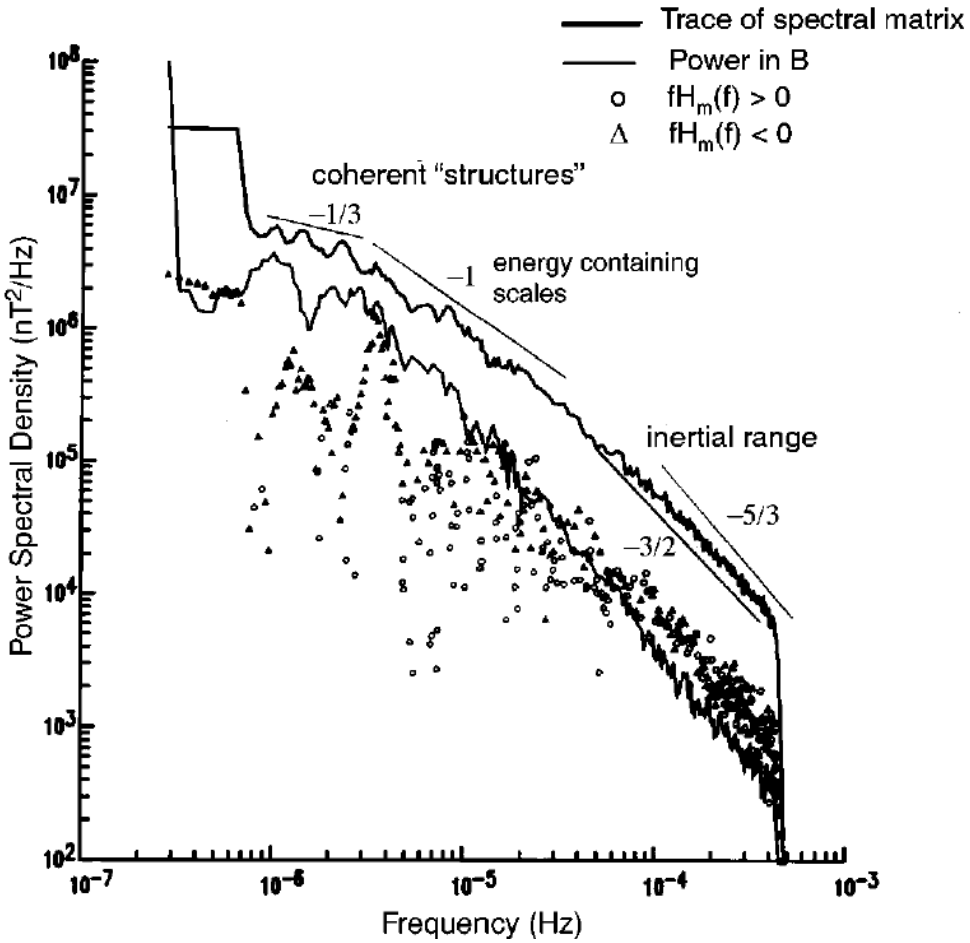

FIGURE 2.13: Energy spectrum as a function of frequency, over temporal scales of one month to a year for HMF data taken at 1AU [*Goldstein and Roberts*, 1999].

2.8.1 Methods

Diffusion and drift coefficients can be calculated from turbulence quantities (More detail as to these coefficients can be found in Chapter 5). The minimum quantities that are required as input for these coefficients are the magnetic field magnitude, a correlation scale of the fluctuations and the normalized variance of the N-component of magnetic field observations. This component is analysed, as the N-direction in a RTN-coordinate system closely corresponds to the direction of the θ-component of a vector in heliocentric spherical coordinates in the solar ecliptic plane. For a *Parker* [1958] HMF, this component is zero, with the implication that any spacecraft measurements of this component would represent measurements of turbulent fluctuations [see, e.g., *Smith et al.*, 2001]. The question that arises is whether the techniques that are presented here for determining the variances and correlation scales are trustworthy with regards to the limitations imposed by the characteristics of early spacecraft data. Provided that data are of a sufficient resolution and without significant omissions, signal processing via Fourier analysis would be useful to provide insight as to the behaviour of the underlying turbulence power spectrum, and is often used [see, e.g., *Bruno and Carbone*, 2013]. This is not possible for the data that will be analysed here. Of course certain approaches call on interpolation between data separated by omissions, but this is not necessarily always a viable approach when concerned with turbulent fluctuations and in data-sets with very high percentages of omissions and low

cadence. *Fraternale et al.* [2016] approached data sparsity by employing interpolation techniques on synthetic data with the same gap distributions as present in *Voyager 2* data. They found that the use of direct fast Fourier transform after linear interpolation resulted in overestimates for the slope of the power spectral density increasing with the length of gap sections that were filled by the interpolation. They also applied a windowing technique described by *Blackman and Tukey* [1958], which allows SW spectral analysis at 1AU with data omissions of less than 10% of the data, with higher data sparsity affecting the computation of correlations to higher degrees. In the present study the use of interpolation techniques was abandoned altogether, as well as the intent of using Fourier analysis due to the presence of omissions far exceeding the 10% acceptable for such analysis [*Blackman and Tukey*, 1958]. Instead this study will focus on alternative statistical techniques such as constructing magnetic variances and the two-point autocorrelation function that describes the degree to which points are correlated through a characteristic length scale of turbulent fluctuations. This section thus introduces alternatives to Fourier analysis in the context of finding suitable turbulence analysis techniques.

Nel [2015] utilized an analysis technique that relies solely on constructing averaged magnetic variances for increasing separation intervals for selected data. In the study by *Nel* [2015], the effects of data omissions was tested on this technique, which was then found to be robust enough to handle relatively high percentages of omissions present in data. Furthermore, *Nel* [2015] tested the same method for *Advanced Composition Explorer* (*ACE*) data for different resolutions, coming to the conclusion that higher resolutions of data yield better results, while the lower resolution data still appear to follow the same trend. The equation for the magnetic variance, as employed in the present study, is given by [see, e.g., *Forsyth et al.*, 1996]

$$\delta B^2 = \frac{1}{n}\Sigma_{i=1}^{n}(B_i - \langle B\rangle)^2 = \langle (B_i - \langle B\rangle)^2\rangle \tag{2.13}$$

where angle brackets denote an average, n is the number of data points in an interval and i denotes which point of the interval is considered. In the PV technique, variances for intervals of the size of a specific lag, the separation length or time between two data points, are determined and then averaged over all intervals with that lag as well. This then provides an indication of the change in average variances as the choice of lag increases and produces, in essence, a measure of the integrated turbulence power spectrum. When spacecraft data are considered, the magnetic field component used in the equations in this study is the N-component of HMF measurements, in RTN coordinates, as discussed above. Figure 2.14 shows the magnetic variance as a function of the lag frequency taken from *Nel* [2015]. This was done by a three-stage fit corresponding to an integrated turbulence power spectrum over the variance data, with the first and second vertical dashed lines, from the right, indicating the scales at which the transitions occur from the inertial range to the energy-containing range and then from the energy-containing range to the outer range at the lowest frequencies. *Nel* [2015] notes the increase in disorganised behaviour of variance data in 2.14 at low frequency, corresponding to the outer range, when compared to the relative smoothness of results around the energy-containing and inertial ranges at higher frequencies. It is therefore expected to see some disorganized behaviour at the highest of lag separations when determining magnetic variances in a similar way, as will be done in this study.

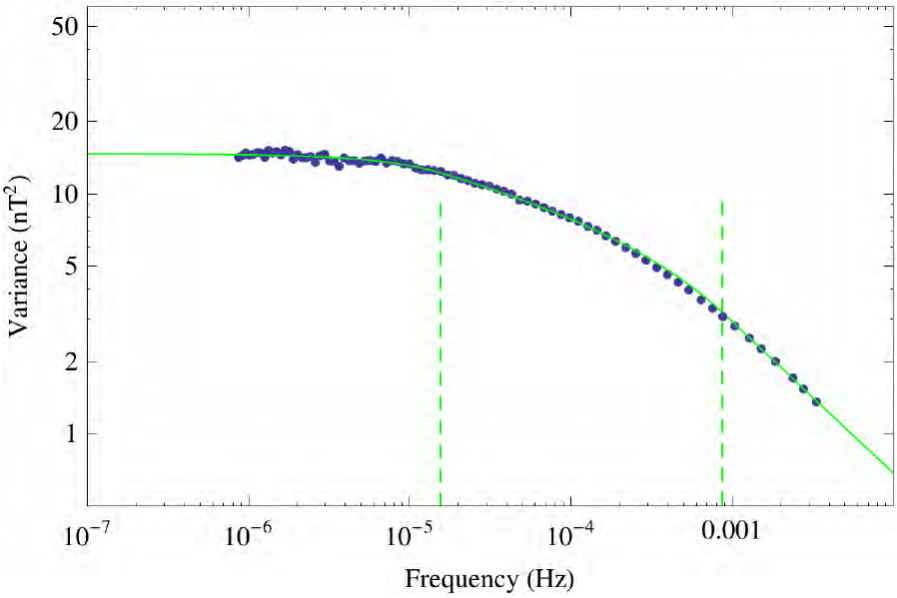

FIGURE 2.14: An example of the magnetic variance as a function of frequency produced by *Nel* [2015]. Vertical dashed lines, at high frequency and low frequency (right to left) indicate transition scales from inertial to energy-containing and later to outer scales, respectively. The solid line is a three-stage fit bound by the different transition scales of the results computed from synthetic data generated using the method of *Decker and Vlahos* [1986] and *Decker* [1993] detailed in that study.

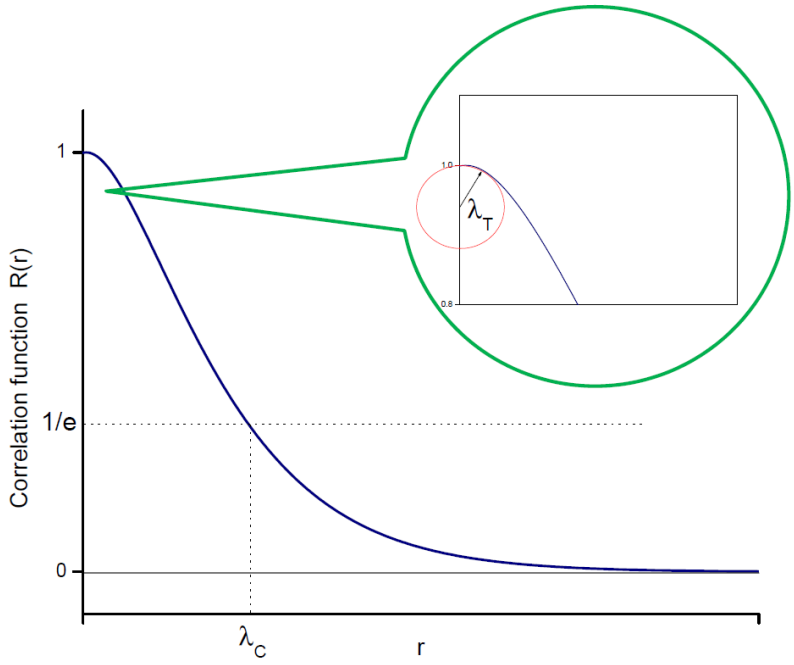

FIGURE 2.15: Generalized form of the two point CF from *Bruno and Carbone* [2013]. The inset shows the radius of curvature at the smallest of scales corresponds to the Taylor scale λ_T, the scale that marks the onset of viscous dissipation on eddies. The correlation scale of turbulent fluctuations is shown to be the scale at which the function $R(\tau)$ drops to $R(0)/e$.

An important feature of the underlying turbulence is the degree to which fluctuations are correlated. The two-point autocorrelation between data points serves to quantify this, and can be written as the average of the product between lag separated observations of the N-component of the field [see, e.g., *Batchelor*, 1953; *Matthaeus et al.*, 1999; *Bruno and Carbone*, 2013],

$$R_{CF}(\tau) \equiv \langle B_N(t) \cdot B_N(t+\tau) \rangle \tag{2.14}$$

This definition of the CF follows from the definition of the velocity CF described by *Batchelor* [1953], and CFs have the general form shown in Figure 2.15. The CF is an indicator of the degree of correlation between two points of a specific separation. A value of one relates to clearly correlated behaviour, a value of zero or near zero which is typical at large separations indicates that the effective behaviour between the two positions is unrelated. Before the function crosses the horizontal axis an exponential curve can be fit to the data. This motivates the approach whereby a large degree of correlation is quantified by the use of the e-folding value, the lag separation at which the CF reduces to $1/e$ of its initial value, as a characteristic scale in the data [see, e.g., *Matthaeus et al.*, 1999; *Smith et al.*, 2001; *Bruno and Carbone*, 2013; *Zhao et al.*, 2018]. The correlation scale of turbulence is assumed to be this characteristic length scale denoted by λ_c in Figure 2.15, at which fluctuations in the turbulence magnetic field of the SW can still be considered to be correlated to some extent. Beyond this value the fluctuations observed should no longer display a significant level of correlation. Note that the inset of this figure shows the Taylor scale λ_T, a scale that marks the onset of viscous dissipation on eddies. The analysis of turbulence at such small scales is beyond the scope of this study, given the high frequency spacecraft data needed to analyse the behaviour of such scales [see, e.g., *Matthaeus et al.*, 2007b]. Furthermore, such small-scale turbulent behaviour is not expected to influence the transport of CRs at NM energies [see, e.g., *Engelbrecht and Burger*, 2013; *Dempers and Engelbrecht*, 2020].

The second-order structure of the N-component of fluctuations has been employed in studies of correlation scales of SW turbulence [see, e.g., *Huang et al.*, 2010; *Burger and Engelbrecht*, 2018]. The SSF, in temporal lag terms, can be written as [*Huang et al.*, 2010]:

$$S_2(\tau) \equiv \langle |B(t+\tau) - B(t)|^2 \rangle \tag{2.15}$$

where $B(t)$ and $B(t+\tau)$ are magnetic field values at times t and $t+\tau$, respectively, where τ the aforementioned lag. Figure 2.16 shows the a SSF constructed from spacecraft data by *Burger and Engelbrecht* [2018], and clearly shows the expected shape and is comparable to the magnetic variances of Figure 2.14. The relationship between the second-order structure, the magnetic variance and the CF, as well as the function are shown in Eq. 2.16. This allows one to calculate the CF in a different way to Eq. 2.14, constructing an alternative CF for the N-component observations, the usefulness of which will be determined by the behaviour of the SSF with regards to data resolution and omissions. This CF can be written as [see, e.g., *Huang et al.*, 2010]

$$R_{CF}(S_2(\tau)) \equiv \delta B^2 - S_2(\tau)/2 \tag{2.16}$$

where δB^2 refers to the *total* magnetic variance over all of the data. For both these definitions of the CF (Eq. 2.14 and 2.16) the integration of the normalized CF can be used, as described by *Bruno and Carbone* [2013], to obtain a correlation length λ_c. In this study, the correlation scale of magnetic fluctuations will be determined from the normalized standard CF as well as the normalized SSF CF, using the e-folding definition. These normalized CFs can be written as

$$R(\tau) = \frac{R_{CF}(\tau)}{R_{CF}(0)} = \frac{\langle B_N(t) \cdot B_N(t+\tau) \rangle}{\langle B_N^2(t) \rangle} = \frac{\langle B_N(t) \cdot B_N(t+\tau) \rangle}{\delta B^2} \tag{2.17}$$

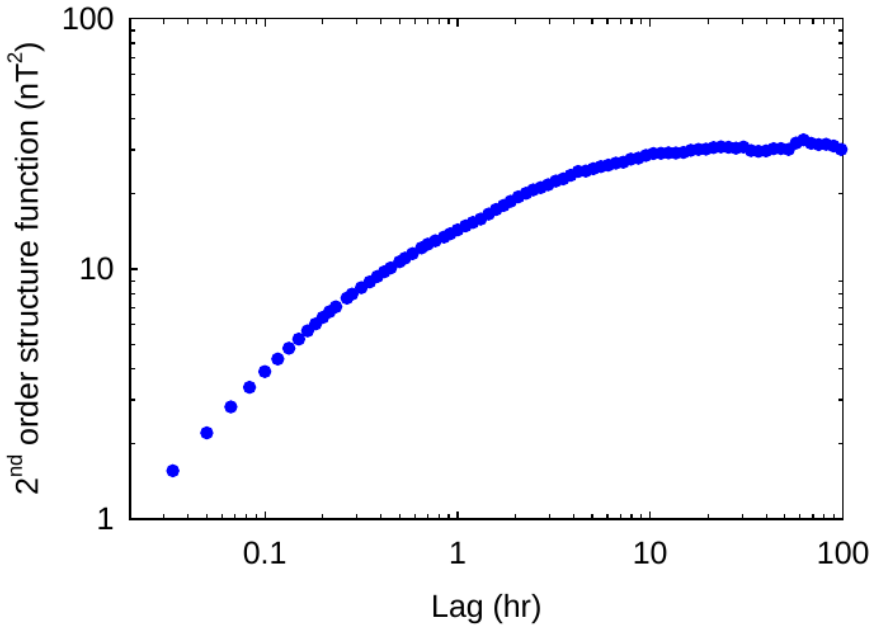

FIGURE 2.16: The SSF as a function of the lag for a section of *ACE* data in the former half of 2001, computed by *Burger and Engelbrecht* [2018] for a maximum lag of 240 hours to ensure the function approaches the expected value of twice the magnetic variance and that its CF approaches zero over large lag separations.

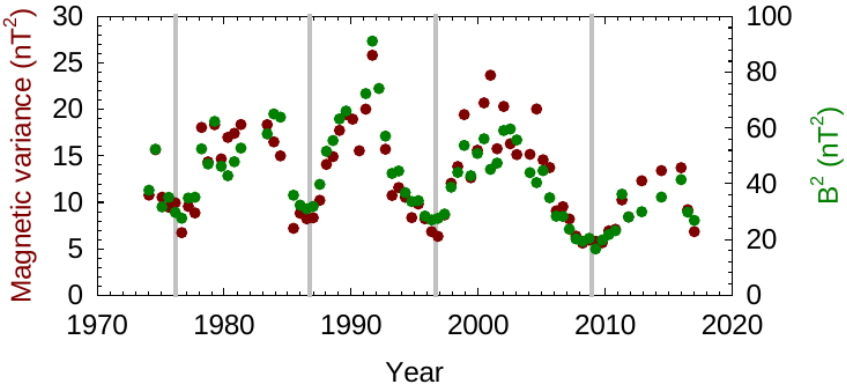

FIGURE 2.17: The correlated behaviour of N-component variances with the square of the field magnitude spanning from the mid seventies to 2018 [*Burger and Engelbrecht*, 2018].

and,

$$R(S_2(\tau)) = \frac{R_{CF}(S_2(\tau))}{R_{CF}(S_2(0))} = \frac{\delta B^2 - S_2(\tau)/2}{\delta B^2} \tag{2.18}$$

where the former is the normalized standard definition of the correlation function and the latter is the normalized SSF-based correlation function that will be plotted throughout the rest of the study. The effects of lowered resolutions and data omissions on the constructed SSF as required for this study are, however, unknown. These techniques are still affected to various degrees by lower data resolutions and omissions. Subsequently the extent to which the turbulence quantities so calculated are affected by these characteristics of the data must be determined in order to choose the best approach to analyse the data relevant to this study.

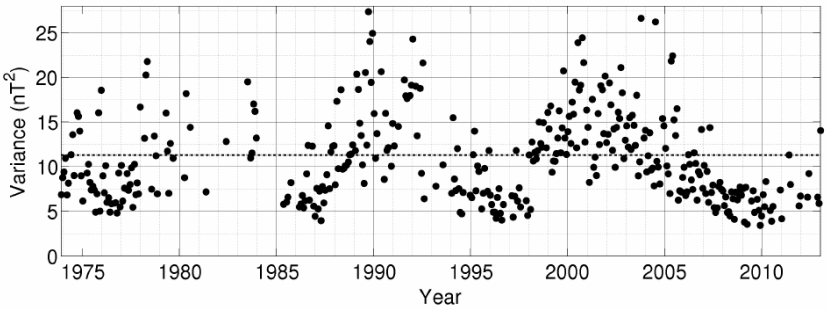

FIGURE 2.18: Magnetic variance averages for 27-day periods of 1-minute *IMP* and *ACE* data for a span of approximately 38 years calculated by [*Nel*, 2015].

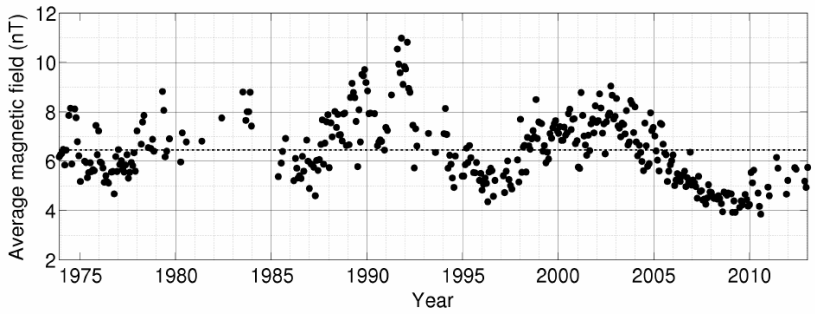

FIGURE 2.19: Averaged magnetic field magnitudes for 27-day periods of 1-minute *IMP* and *ACE* data for the same period as Figure 2.18, taken from [*Nel*, 2015].

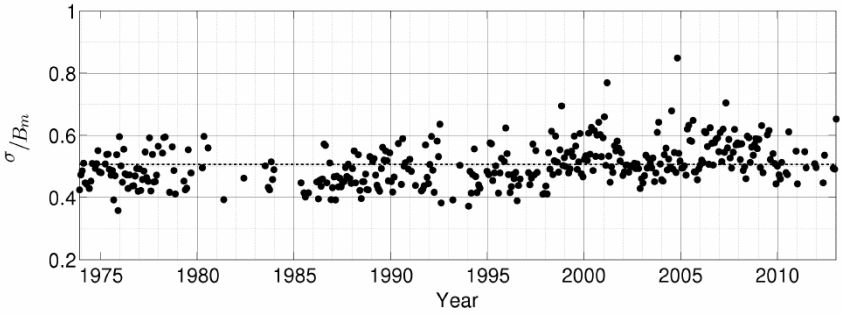

FIGURE 2.20: The square root of the magnetic variance normalized using the average field magnitude for the same 27-day period. The average value for the normalized variance is 0.5, taken from [*Nel*, 2015].

2.8.2 Expectations from Existing Studies

Previous studies of the solar cycle dependence of turbulence quantities allow for comparisons helpful in determining whether the low order statistical methods presented above are robust in the face of data limitations, and give a measure of their efficacy [see, e.g., *Nel*, 2015; *Burger and Engelbrecht*, 2018; *Moloto et al.*, 2018; *Burger and Engelbrecht*, 2018; *Zhao et al.*, 2018]. The study of SW turbulence during periods of solar minima and solar maxima and the trends that are seen as the HMF transitions between solar cycles allows one to quantify the expectations placed on low resolution, sparse observations in the early period of spacecraft investigations.

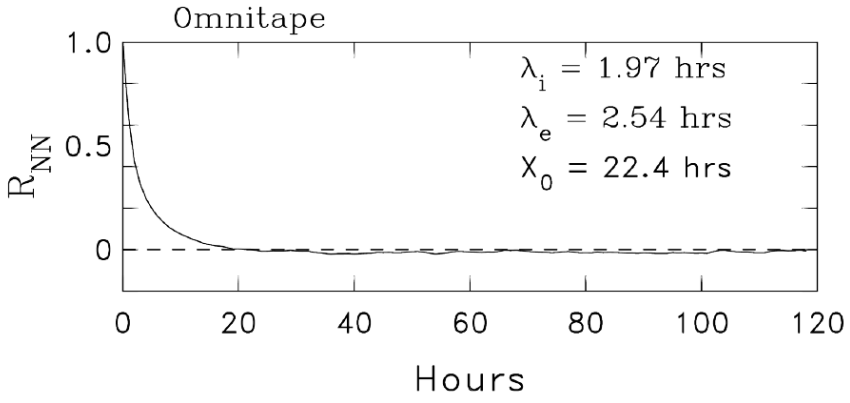

FIGURE 2.21: N-component CF from hourly *OMNI* data with the integral form (λ_i), *e*-folding scale (λ_e) and the first zero-crossing scale of the function being x_0 [*Matthaeus et al.*, 1999]

Magnetic Variances, Field Magnitudes and Normalized Variance

Figure 2.17 is from the study on *OMNI, Interplanetary Monitoring Platform* (*IMP*) and *ACE* data by *Burger and Engelbrecht* [2018], and serves to illustrate the correlated behaviour of the magnetic variance with the field magnitude. *Nel* [2015] also shows, from Lomb periodograms produced from the results shown in Figures 2.18 and 2.19, a possible periodicity of around 11 years. Variances are at a minimum around solar minimum and increase toward solar maximum.

The correlated behavior between the magnetic variance and the square of the magnetic field magnitude suggests that the ratio of the two values, the normalized variance, should remain relatively constant across solar cycles. The normalized variance is of particular importance to the calculation of parallel and perpendicular diffusion coefficients from scattering theory (see Chapter 5). Drift effects also depend on this value as well as the magnetic field magnitude due to the dependence of drift effects on the CR Larmor radius and due to the reducing influence of turbulence on these drift effects. Figure 2.20 shows the relatively constant behaviour of the normalized variance over a 38-year period. *Zhao et al.* [2018], using 1 minute resolution *OMNI* data for a span of 22-years, used Elsässer variables to calculate turbulence energies for which a clear dependence on solar cycle is reported for fluctuating magnetic energy density, residual energies and their corresponding correlation functions. Furthermore, the turbulent magnetic energy calculated in that study correlates with solar cycle and is larger at solar maximum than during minimum conditions. This reflects the time-dependent behaviour expected from magnetic variances presented in other studies

Correlation Functions and Lengthscales

Matthaeus et al. [1999] used the two-point autocorrelation function definition, as well as the *e*-folding and integral definitions for determining the correlation scale for 1 hour resolution *OMNI* data for more than 32 years' worth of data and the resulting correlation time, is shown in Figure 2.21. From this figure the CF by the *e*-folding definition is around 2.54 hours.

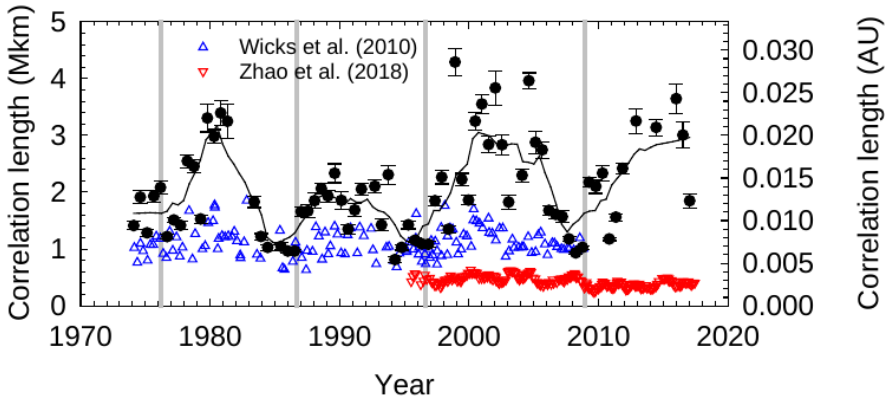

FIGURE 2.22: Possible solar cycle dependence in computed correlation lengths from the SSF applied to 1-minute resolution spacecraft data by *Burger and Engelbrecht* [2018] (black datapoints and line), from their study. These results are ompared with the 1-minute results taken from *Wicks et al.* [2010] (blue triangles) and *Zhao et al.* [2018] (red inverted triangles)

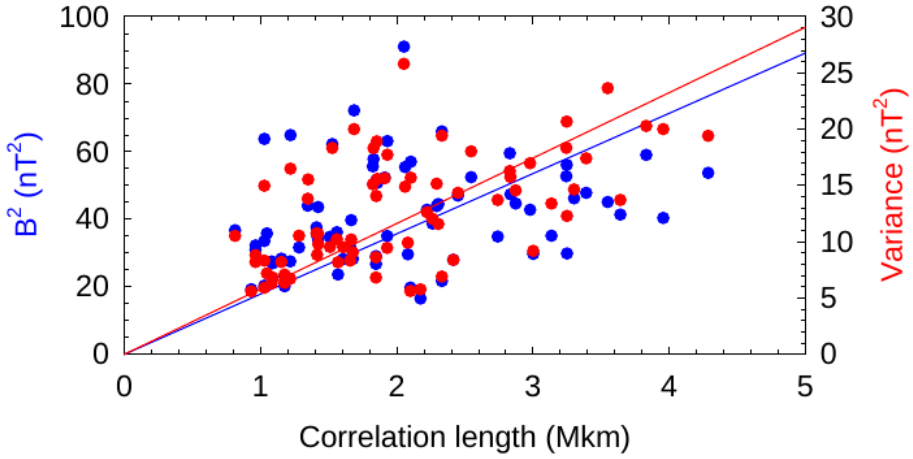

FIGURE 2.23: The correlation between the correlation scale and the magnetic variance of the data (red), as well as, the square of the field (blue), with average regression lines forced through the origin [*Burger and Engelbrecht*, 2018].

Zhao et al. [2018] determined turbulence quantities by an Elsässer variable analysis of higher resolution (1 minute) *OMNI* data, as well as the *e*-folding definition of the correlation scale of turbulent fluctuations, but do not report a significant variation in correlation lengths determined from this technique. *Burger and Engelbrecht* [2018] determined correlation scales in the N-component of the field by use of the SSF calculated from 1-minute *OMNI*, *ACE* and *IMP* data over a few solar cycles. Figure 2.22 shows the results calculated by *Burger and Engelbrecht* [2018] from the SSF of the data which the authors compared to quarterly-averaged results presented by *Wicks et al.* [2010], as well as monthly averages of the 2D correlation scale from the study of *Zhao et al.* [2018]. The notable differences between the results of the other studies may be due to the difference in their choice for the maximum lag separation (choice of two hours maximum by *Zhao et al.* [2018], and eight hours by *Wicks et al.* [2010]), most likely due to data resolution and choice of analysis techniques. Previous studies show that the choice of maximum lag interval over which the SSF is calculated systematically increases the calculated correlation length [see, e.g.,

Matthaeus et al., 1986]. The results of *Burger and Engelbrecht* [2018] also show a significant likelihood of an approximate 11 year periodicity in the correlation length of turbulence, with correlation scales being lower during solar minima and increasing by at least a factor of 2 towards solar maximum. The analysis presented in this study by the introduced techniques on low resolution spacecraft data should yield lower correlation scales near solar minima and comparatively higher ones during maxima in order to be comparable to these established results, given the low cadence of early spacecraft data. Figure 2.23 shows the possibility of a linear relationship between the correlation length and the magnetic variance from *Burger and Engelbrecht* [2018]), which they constructed to compare with a figure of the same kind presented by *Matthaeus et al.* [1986].

2.9 Summary

In this chapter, topics in heliospheric and CR physics relevant to this study were briefly and generally introduced. Furthermore, the data analysis techniques that will be used throughout the rest of the study to calculate turbulence quantities from observations were described and a framework was set in order to compare the results of these techniques with those from other studies. By the results presented that magnetic variances and correlation lengths increase from solar minimum to solar maximum, the expectation exists that the analysis techniques presented here should at least reproduce this behaviour to a certain degree. Before turning to the analysis of these spacecraft observations it is necessary to quantify the extent to which the analysis techniques presented here are affected by lowered data resolution and high percentages of omissions, as seen in early spacecraft data. An investigation into these effects is the subject of the next chapter.

Chapter 3

Testing Data Analysis Techniques

3.1 Introduction

Given the limitations inherent to the early space age spacecraft data-sets of interest to this study, it is necessary to test the various analysis techniques introduced in Chapter 2 so as to ascertain the reliability of the results they yield within this context. This can be done using synthetic turbulence data for which specific parameters are already known. The process of generating such a simulated data-set, to be used here while beyond the scope of this work, is detailed by *Nel* [2015] and follows a generalized approach by *Decker and Vlahos* [1986] and *Decker* [1993]. The data represent fluctuating magnetic field measurements and the entire set is generated so that the total variance is 10nT^2. The assumptions made in generating the synthetic data are that the mean field is approximately zero and that the spectral form of the data shows a flat energy-containing range and a Kolmogorov inertial range, similar to the spectral form employed by e.g. *Bieber et al.* [1994]; *Shalchi et al.* [2004]; *Minnie et al.* [2007a] and *Minnie et al.* [2007b]. Such a data-set allows for the application of the various techniques so as to verify under what conditions their results approach the set parameters. The analysis techniques that will be tested here, as discussed in detail in Section 2.8.1, are the construction of partial variances (Eq. 2.13) and the second-order structure function (Eq. 2.15), as well as the standard correlation function (CF, Eq. 2.14) for turbulence as opposed to an alternative correlation function based on the second-order structure function (see Eq. 2.16). The simulated data will be used to test the loss of information due to lowering resolutions by averaging data, as well as the effects brought about by data gaps through the omission of data points, both randomly and in a way similar to the gaps present in extant spacecraft data-sets. It can be noted from looking at these early data-sets that omissions seldom occur as isolated events and are, more frequently than not, packed together into blocks of omissions where data were not recorded for a period of time before normal recording was resumed. This may affect the results from analysis techniques in unexpected ways, and will be investigated here.

3.2 Approach to Testing the Effects on Analysis Techniques

The analysis of turbulence in general is concerned with the examination of correlations at a variety of different scales, as generated by, for example, the energy cascade present in turbulent motion. Restricting the resolution of a sample set may undermine the detail in which the turbulence in a fluid such as the solar wind plasma can be investigated. Heliospheric magnetic field (HMF) data are commonly found in various resolutions, and are often comprised of an averaged number of measurements over smaller intervals over that span of time. The question of how resolution affects the information obtained is therefore

to a degree analogous to how averaging data points effects the available techniques. The synthetic data-set considered here has values that range between −10nT and 10nT and consists of 4.194306×10^6 data points. The number of each data point, for the purpose of investigating the effects on averaging, will be taken as a proxy for real data cadence, such that, if each point were assumed to be equivalent to a 1s data point, a data-set generated from the original data by taking 60 point averages would represent minute resolution data, and so forth. In this chapter three resolutions corresponding to seconds, minutes and one hour, are presented.

Additionally, two methods of producing gaps in the synthetic data are tested. The quickest way is to randomly select indices for removal throughout the entire data-set, for gap percentages ranging from 5% to 95%. This is not how gaps appear in spacecraft observations, at least in such early data-sets. Instead, gaps in spacecraft observations tend to be grouped together to a higher degree, and appear as blocks of missing data of various lengths interspersed throughout the set. To replicate this, a list of gap block lengths was generated and given initial positions at random, and the positions of the gaps cut into the test data were recorded to be used in the higher percentage gap files. The used positions for the random gaps were also reused, as doing this allows one to compare results of different gap percentages with one another as though the gaps are compounded after each increase in percentage. After inserting gaps into the data files of differing resolutions for various omission percentages, the analysis of the data was done as for the resolution part, keeping the effects brought about by resolution in mind.

3.3 Effects on the Second-order Structure Function (SSF) and the Construction of Partial Variances (PVs)

To test these effects, the synthetic data were initially assumed to be taken at one second resolution. The data were then used to obtain the SSF and PV associated with increasing separation intervals. PVs were constructed for increasing separation intervals, starting from a minimum lag of two seconds and increasing up to half of the length of the data-set. For each choice in the time lag, the data-set was split into subsequent intervals each containing the same number of points corresponding to the current lag, over which subset variances were calculated and eventually averaged together. When the lag is sufficiently low, many sub-interval variances contribute to the final average, and thus sub-intervals containing remaining points considered too short to significantly affect this number were discarded. At larger lags, especially where interval lengths approach half the total number of data points, this can bring about scatter in the final result. By assuming homogeneous turbulence, this was remedied by starting consecutive intervals in the middle of the previous one, increasing the number of results contributing to the final average, and leaving fewer data points unused. The SSF was computed as discussed in Chapter 2. The data-set values were binned into 60s intervals and averaged to produce a new reduced set of one minute resolution data which would also be analysed following the same procedure. A logarithmic step was used following the approach used by *Nel* [2015] to reduce computing times whilst dealing with such a large number of data points in both the "one second" and "one minute" resolution cases. The synthetic data were also binned into 3600 second intervals and averaged to produce and subsequently analyse an hourly-averaged data-set. For now, only the results for one second and one minute data-sets will be shown, while the results for the hourly data will follow in their own section, as that resolution will be the

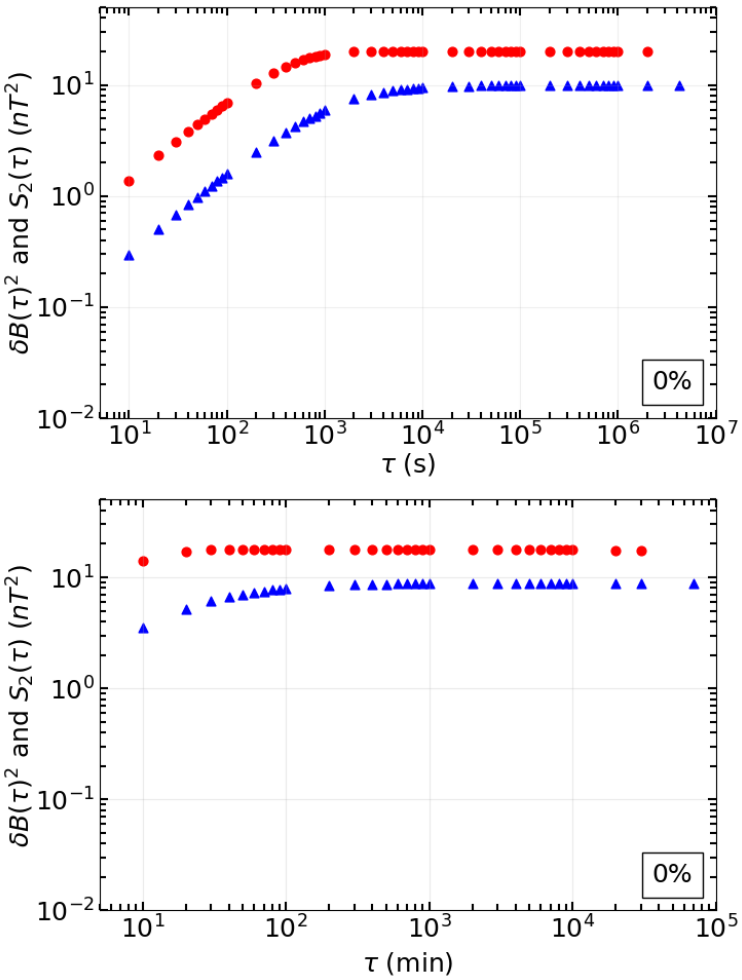

FIGURE 3.1: SSF (red) and PV (blue) results from one second (top) and one minute (bottom) resolution data, respectively.

same for the spacecraft data featured later in the study. The results of these techniques for the synthetic and minute resolution data are here compared, after which the correlation functions (CFs) were computed and the *e*-folding values determined, as will be discussed in the following sections.

Figure 3.1 illustrates the results from both the SSF and PV techniques for the unaveraged (assumed 1s resolution) data-set (top) and the results after prior averaging into one minute resolution. The top panel is the baseline for expected results from both techniques and will be the basis of comparison, in terms of these techniques during this chapter. The PVs approach the value of $10nT^2$ and the SSF goes to double this value at large lags, as expected from Eq. 2.15, after passing through a Kolmogorov inertial range into a energy-containing range, and are comparable with Figures 2.14 and 2.16. The SSF has a visibly sharper transition to the energy-containing range than the PVs. Comparing the one second resolution data results with those calculated from the one minute data it is apparent that prior averaging of the data to change the resolution greatly affects the appearance of results. Firstly, the total variance of the data-set is reduced slightly, causing a drop in the values that both functions approach. The effect was also reported by *Nel* [2015], who similarly analysed spacecraft data at various resolutions. These reductions in the PV and SSF results are due to sub-interval averages having less deviation between one another than the raw data points have between them. It is clear that this should directly affect the PVs, while the

second-order structure is affected by a tightening of the span of the averaged values that the reduced set points assume after averaging. Secondly, prior averaging seems to smooth the results at shorter separations, effectively causing the inertial ranges of both approaches to be abbreviated, making the detail in this range, and the shape of the underlying spectrum, less clear. The major result from this is the expectation of lower total variances and SSF values at all lags as the data resolution decreases.

The panels of Figure 3.2 show the PVs (blue) and SSFs (red) obtained from the synthetic data-set for different percentages of omissions. The lefthand figures show the results for 50%, 70%, 80% and 85% gaps, for randomly placed omissions in the one second resolution data-set. The righthand panels show the same results for the same percentage omissions, but with the gaps placed in a manner so as to replicate the gap distribution in spacecraft data. Figure 3.3 displays the same results as in Figure 3.2, computed for one minute resolution data after applying omissions in the same manner. When compared the left columns of Figures 3.2 and 3.3 show that, when regarding randomly placed omissions in the data, both PVs and SSFs are relatively insensitive to gaps until very large percentages of the data are missing. The major effects are changes in the inertial range results due to averaging rather then the placement of gaps, as well as an increase in fluctuations in the SSF with increasing gaps. The right-hand side shows that the PV technique is affected to a larger extent for spacecraft-like data gaps, with the computed results becoming even more sensitive to the effects of prior averaging.

The increase in gap-percentages influences the SSF by increasing fluctuations in the function results as the maximum lag is neared. The PV technique suffers in shape as the lower and intermediate lag results are lower with increased data-sparsity. The higher resolution results presented in Figures 3.2 and 3.2 show that the SSF approach yields the expected results somewhat better than the PV technique. A major result from Figures 3.2 and 3.3 is the increase in fluctuations for the techniques at larger separations as resolutions decrease and the percentage of gaps increases. The scatter occurring in the SSF would conceivably affect a CF computed from it adversely, therefore the use of the PV technique may be more useful when handling lower resolution data. Both techniques once again show that the values that they approach at high lag, decrease with lowered resolution. Furthermore, the degree to which both the SSF and PV techniques final values decrease is the same, regardless of the sparsity of data or the method by which the gaps are placed.

3.4 Effect on The Correlation Function

Here the logarithmically spaced results for the computed CFs are given for the one second and one minute resolution data, corresponding to Figures 3.2 and 3.3, respectively. Figure 3.4 shows the effects of decreased resolution by prior averaging on the two techniques used here to determine the CF. The standard CF is computed throughout this study in a similar way to the SSF due to the use of two lag separated values that contribute to produce a single result for both Eq. 2.14 and Eq. 2.15 in Chapter 2, causing data sparsity to be of greater concern. For the standard CF the products of every pair of data points separated from each other by the current time lag are averaged to form the value of the function. Whereas the second CF is calculated by using SSF values, and are simply the difference between the total variance of the entire data-set and the half of the value of the computed SSF at the current choice of lag. The top panel of Figure 3.4 shows that the two normalized

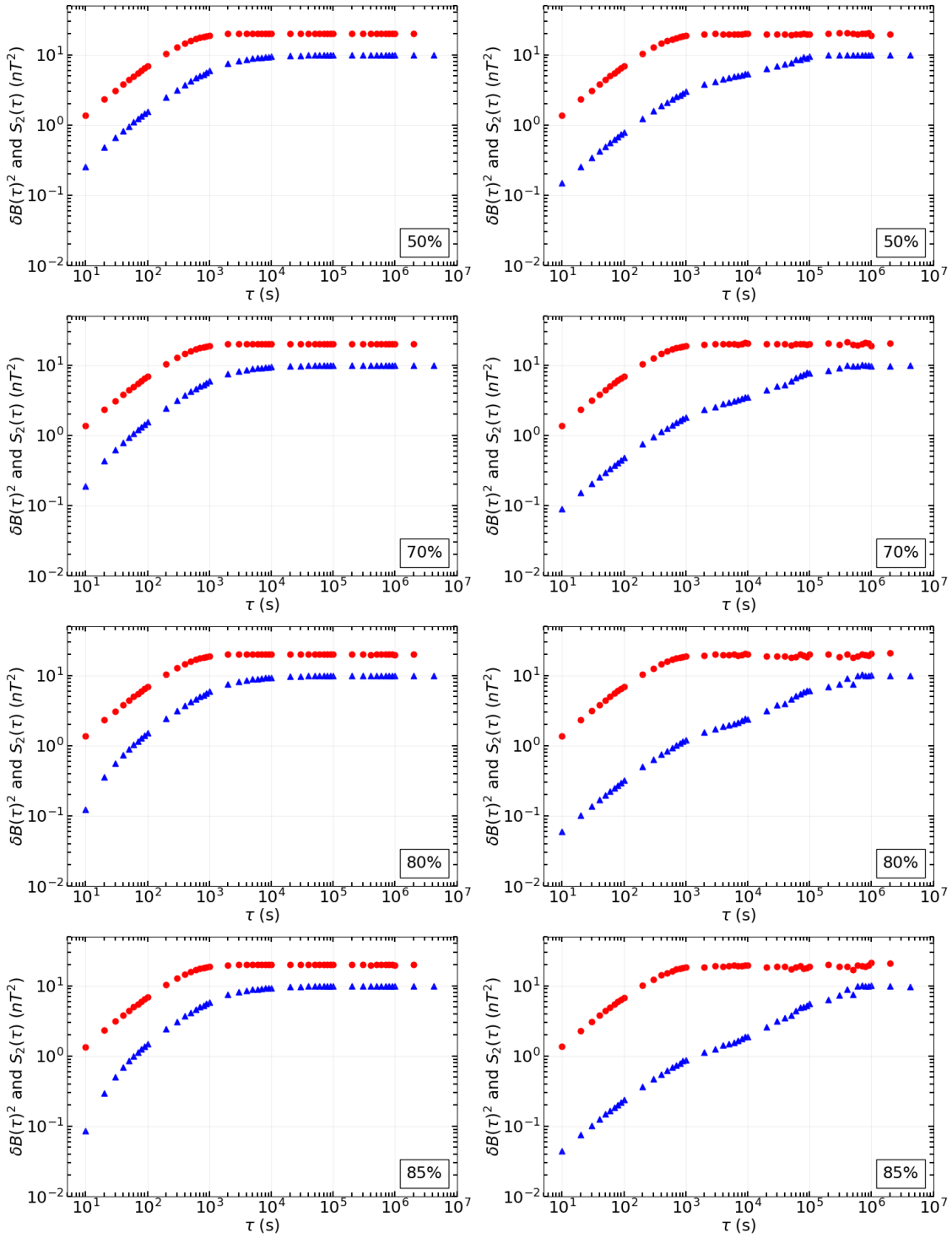

FIGURE 3.2: SSFs (red) and PVs (blue) for random data omissions in increasing percentages (left column), and for spacecraft-like omissions (right column) using one second resolution data. See text for details.

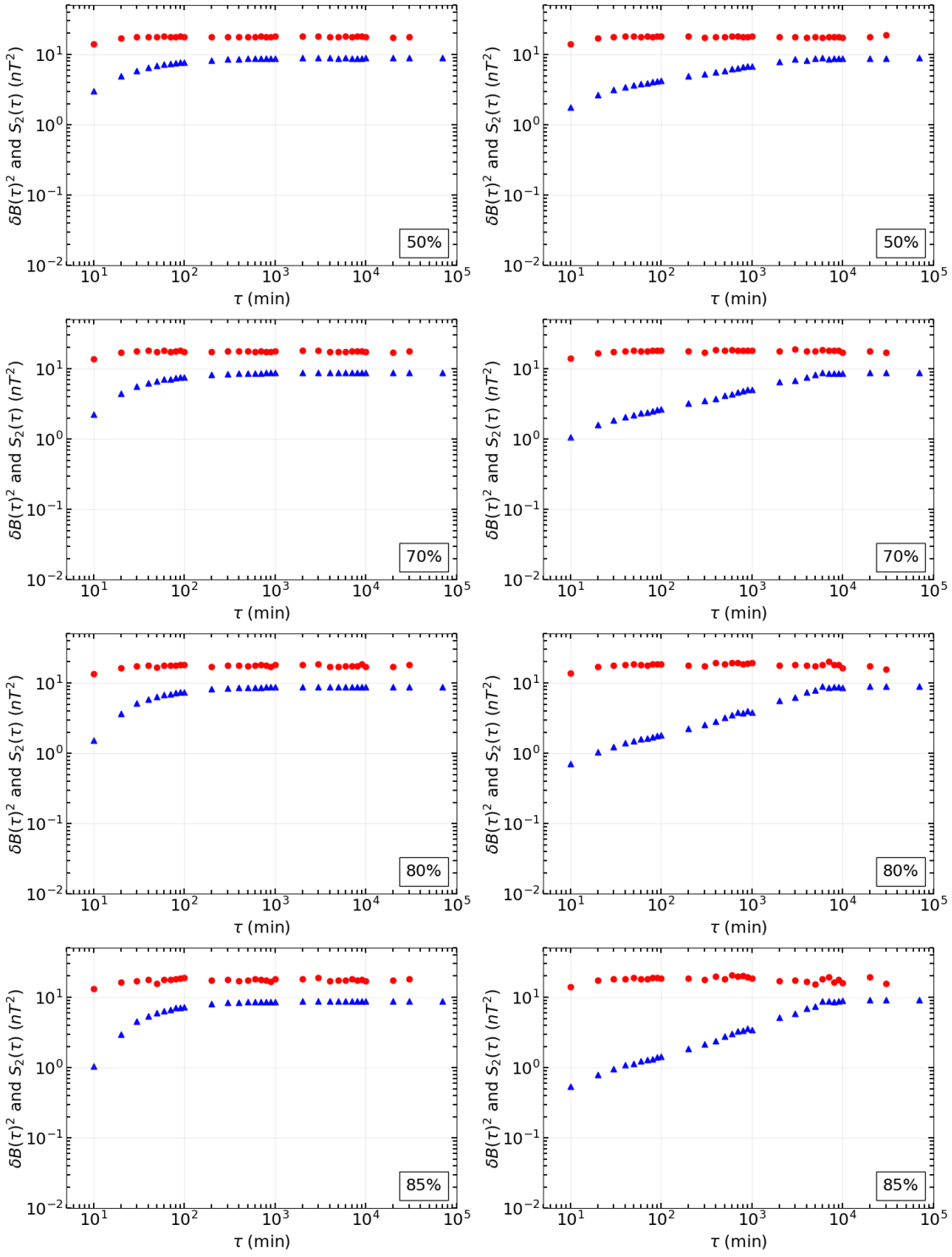

FIGURE 3.3: SSFs (red) and PVs (blue) using minute averaged data, following the same configuration as the previous figure (Figure 3.2). See text for details.

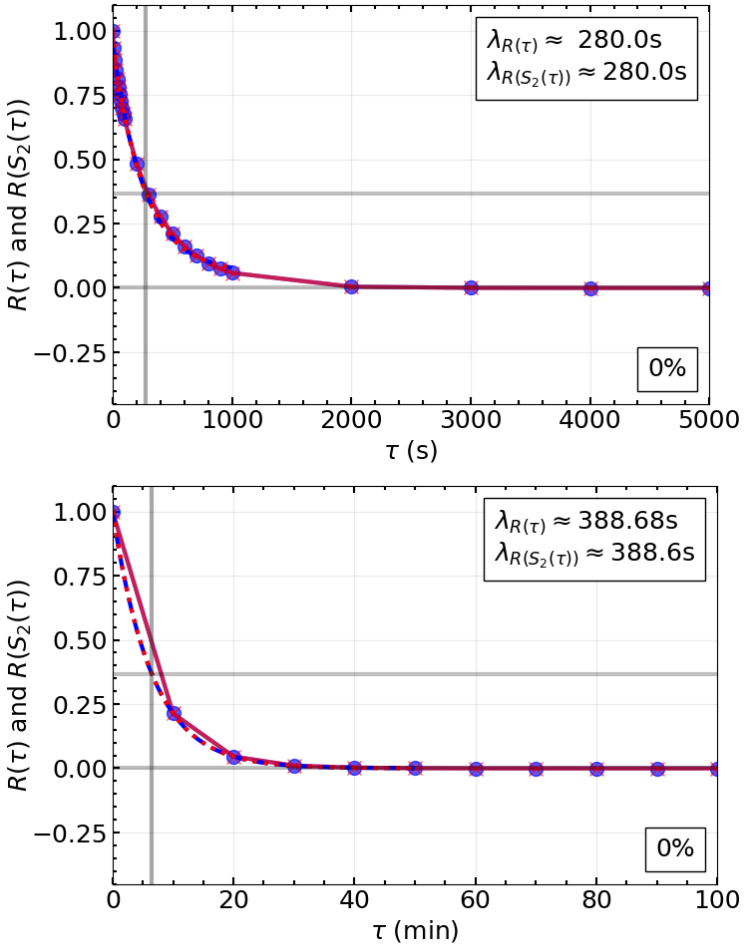

FIGURE 3.4: Normalized standard (blue) and SSF (red) definition CFs for one second (top panel) and one minute (bottom panel) resolution data in the absence of omissions, respectively. The top panel shows a correlation time (*e*-folding value) of 280s, while the bottom panel results in a correlation time of around 389s.

CFs yield the same results, even for different resolutions in the case of 0% gaps, as expected from Eq. 2.14. From the panels it can be seen that the CF drops exponentially towards zero at large lags and for the one second resolution data has an *e*-folding value of 279.99s. Comparing the correlation graphs for the different resolutions shows that there are fewer points present to characterise the exponential decline, so that for these sets, correlation times calculated for higher resolution data approach zero more rapidly than those computed for lower resolution data. The one minute CFs show *e*-folding values of $\simeq$ 388.6s. This is a clear indication that lower resolution data yield smoothed results and calls into question how reliably correlation scales can be found from even lower resolution data. The two-point and second-order structure defined CFs are expected to yield different results, as the former will be affected by the number of viable product pairs for averaging, and the latter relies on the SSF, which itself is affected by omissions as seen by the improved scatter for higher percentages of gaps observed in the previous section.

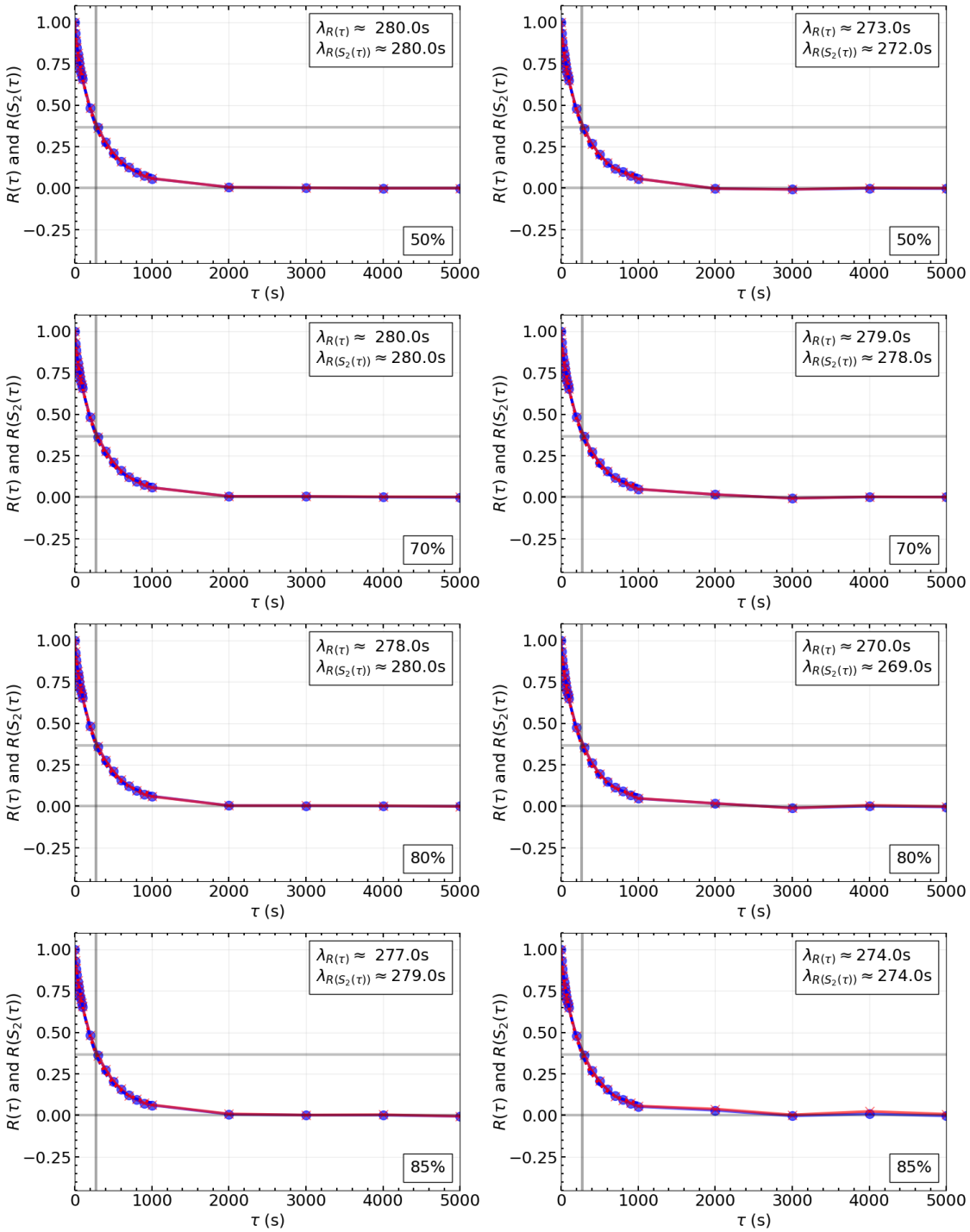

FIGURE 3.5: Normalized standard (blue) and SSF (red) CFs with *e*-folding values for one second resolution data-sets with increasing gap percentages (in descending order) for random (left column) and spacecraft-like (right column) placement of omissions.

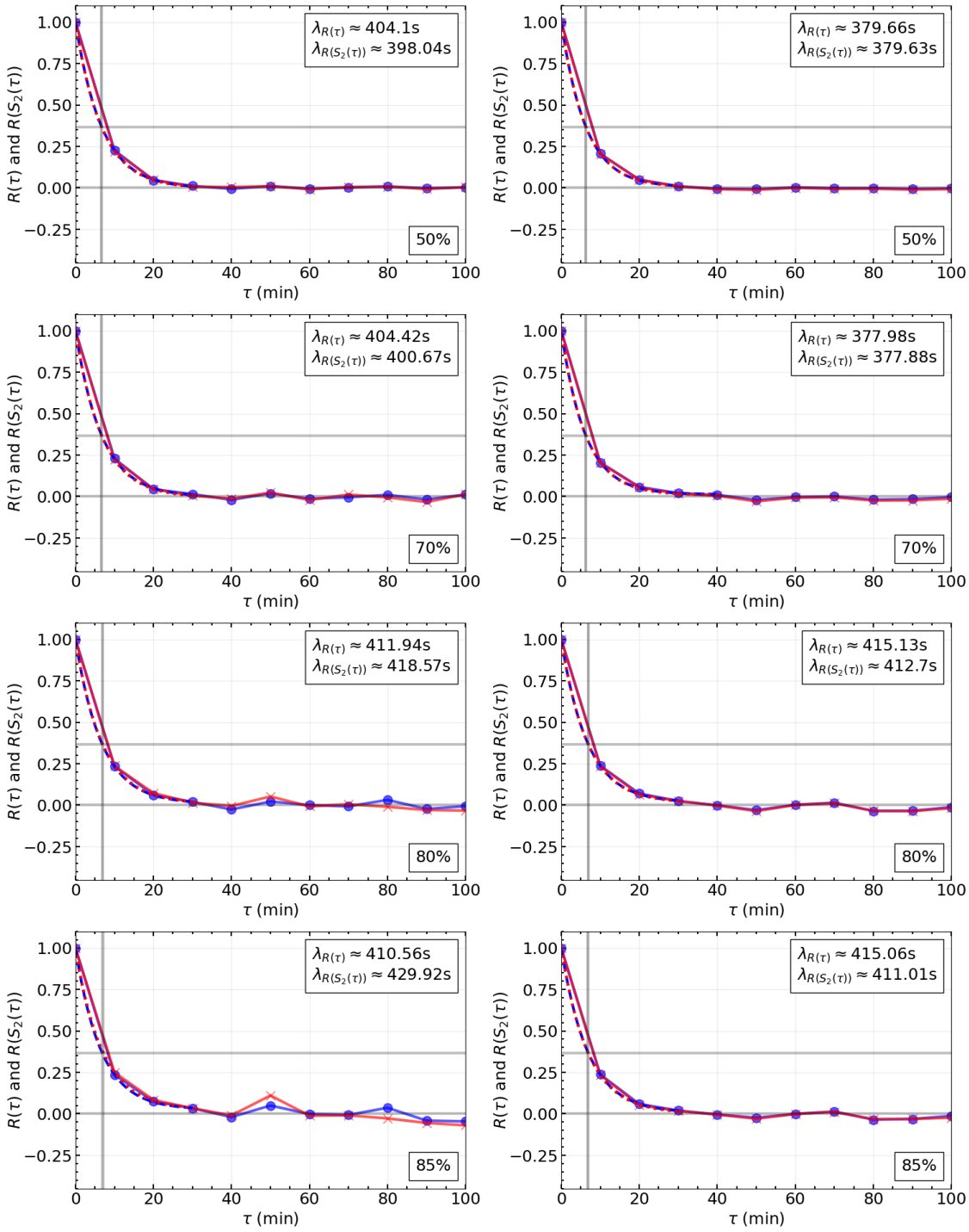

FIGURE 3.6: Normalized standard (blue) and SSF (red) CFs with *e*-folding values for minute averaged synthetic data. As in the previous figure (Figure 3.5), left and right columns display random and spacecraft-like gap placements in descending order in terms of percentage omissions.

Figures 3.5 and 3.6 show the results for higher percentages of gaps with the random gaps result in the left column and spacecraft-like gaps on the right. For the correlations of the one second resolution results, in Figure 3.5 the random and spacecraft-like omissions hold up very well at all data-sparsities, with the latter showing larger differences from the 0% case. Even when faced with omissions, the one second resolution data show no significant change in *e*-folding value with increasing gap percentages, with the values for both techniques at all percentage omissions being similar in Figure 3.5 and the top panel of Figure 3.4 (the 0% case).

When considering the minute averaged results in Figure 3.6 an interesting effect is seen almost immediately in comparison with the one second resolution results. When synthetic data with randomly placed omissions are considered, and with increasing percentages of omissions, the results are more erratic at lower omission percentages when compared with the results for more realistic gap placement at similar percentages. The nature of random placement of gaps allows for more even distribution of gaps throughout the data. This however has a detrimental effect on the exponential decline in the CFs and therefore has the potential to cause changes to the *e*-folding time. Spacecraft-like gap placement results seem to retain the overall behaviour as discussed for the second resolution data, and the results are affected to a lesser extent by the increase in percentage omissions. It is important to note that the increase in number of gaps and lowering of data resolution stretch the exponential portion of the CF, with the result that features that may be important, such as the scales where the function intersects the horizontal axis, are shifted significantly.

The apparent shift in the exponential portion of the standard CF is mainly due to the lowered resolution. Similarly, as shown in the previous section, the SSF is also dependent on the resolution, which would affect the calculation of its CF. Although the *e*-folding values of higher gap percentages are also not significantly changed from the 0% case, it should be pointed out that the *e*-folding values for the minute data overall are significantly different to those of the second resolution data. Furthermore, the averaging process has brought about the problem that detail in the initial decline was altered to such an extent as to raise concern as to whether reliable information can be obtained from this feature, as proposed by *Matthaeus et al.* [1999].

3.5 Effects of Data Gaps and Sparsity for Hourly Data

Here the results for hourly synthetic data are presented. Since the number of data points in the set is significantly reduced, the computation of these results is no longer done with a logarithmic step in separation interval sizes. This also allows for greater detail in Figure 3.7 which shows the results of the hourly resolution data-set for 0% and 70% omissions. The drop in total variance previously seen across all scales for the PVs and SSFs due to prior averaging is clearly present here, as well as the loss in detail at smaller lags. The variances approach the same maximum for both percentages of gaps with the presence of gaps causing the transition to energy-containing scales to occur at larger lags with some increased scatter in results across the whole set. The SSF shows a significant increase in scatter for increasing gap percentages. Two effects are present in Figure 3.7 when compared to the results presented in section 3.3. Firstly, the logarithmic step in the computation of the higher resolution results causes loss in detail in the figures of SSFs and PVs, such as the increased fluctuations at higher lag separations presented in Figure 3.7. It can be seen in Figure 3.7 that both the PV and SSF techniques show higher degrees of scatter at larger lags, with the results from the former technique being affected to a lesser extent. Thus, secondly,

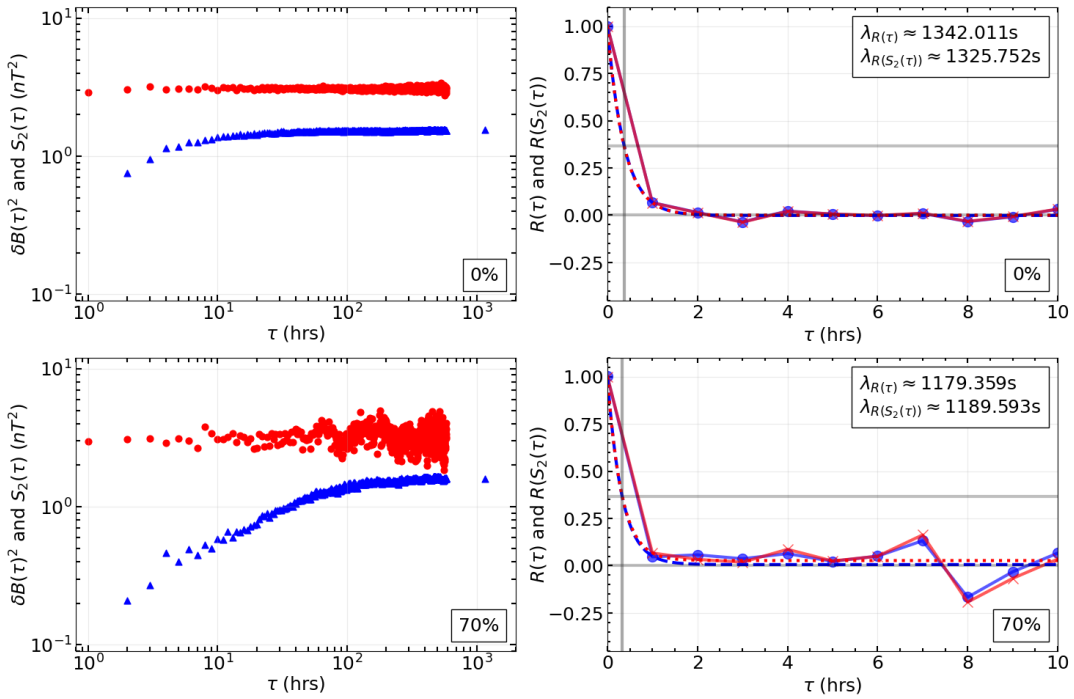

FIGURE 3.7: PV (blue triangles) technique and SSF (red dots) results for hourly averaged synthetic data for 0% and 70% omissions (left column), and corresponding normalized standard (blue) and SSF (red) CFs (right column). The logarithmic step in lag choices has been dropped in order to illustrate the effect of prior averaging and data gaps in greater detail.

the additional sub-intervals used in calculating averages for the PV technique results are able to smooth out the results, while the SSF suffers in the sense that for the largest of lags, there may simply not be any pairs separated by the given lag value. Even when there are pairs separated by a specific lag value, there may not be a sufficient number of pairs to obtain a reliably realistic average. Given the large amount of scatter seen at large lags in the results yielded by the SSF technique, the PV technique retains its characteristic behaviour to a greater degree in the face of the limitations that could be present in low resolution spacecraft data, and will be used in the rest of the study to calculate total variances, given the increased scatter at large lag separations visible in the SSF. The large scatter due to gaps for the SSF and the dependence of the correlation function calculated from it, immediately suggests that the CF so calculated is not suitable for use in this study.

The right panels of Figure 3.7 show the corresponding CFs. The results for both proposed techniques are very similar, with increasing fluctuations occurring in both functions at large lags and a slight difference from the standard CF occurring for higher percentages of gaps. Although not shown here, the effect is quickly compounded for even higher percentages of gaps by further exaggeration of the effects of data gaps due to the averaging of data discussed in the previous section. The correlation times are quite similar for both functions in both cases, with a slight decrease in correlation length with increasing omissions in the data. The correlation time in both cases is around 20 minutes, which, when compared with the results from higher resolutions, indicates that the lower resolution of the data inflates the correlation time, which suggests that correlation scales computed by both methods will be overestimates. Regardless of this, the standard two-point CF and the e-folding definition of the correlation scale of turbulence are selected to be used in further analysis, in order to attempt to glean whatever relevant information the CF might still be able to yield.

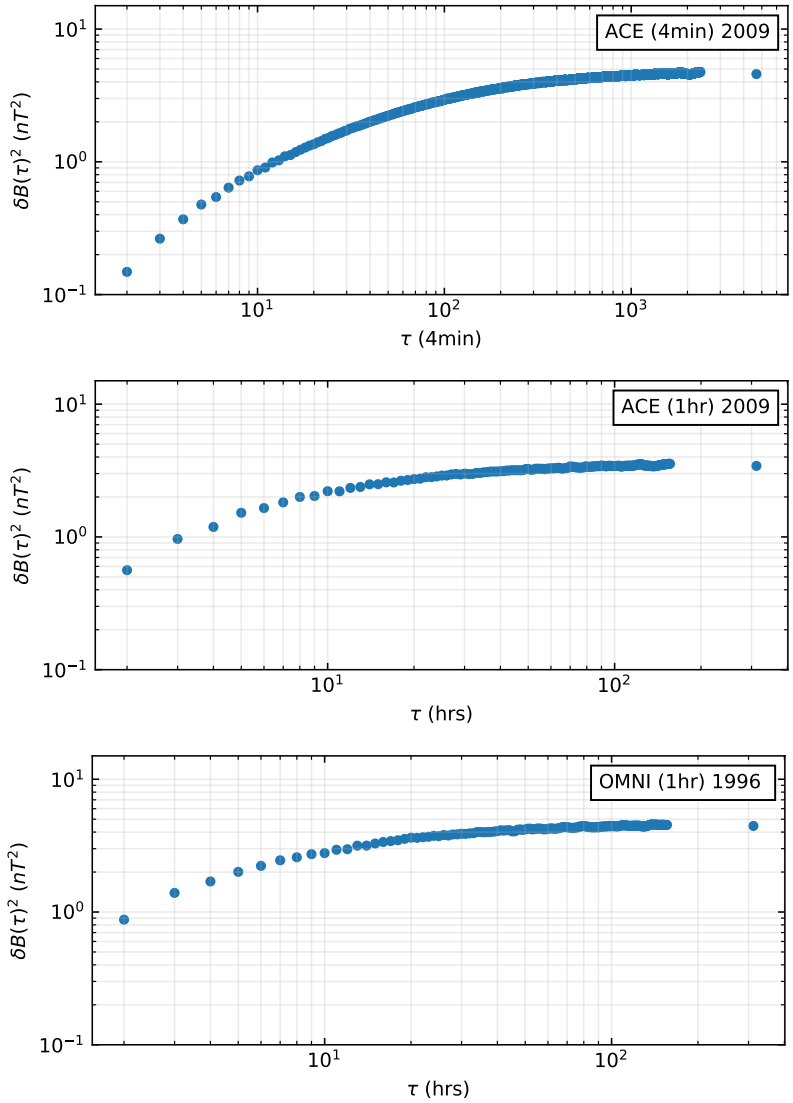

FIGURE 3.8: PVs calculated from 4-minute (top) and 1-hour (middle) resolution *ACE* data during 2009, near solar minimum. As well as a similar plot using *OMNI* data centered on the 1996 solar minimum (bottom).

3.6 Test of Selected Techniques on Spacecraft Data

In this section the selected analysis techniques are applied to modern spacecraft data in order to show how the results compare to the results of previous studies presented in the previous chapter. *Nel* [2015] used *ACE* data to motivate a choice for the resolution of data to be used in that particular study. Although the form of the results remains the same across all resolutions tested, the author reports significantly less fluctuations at larger separations and a drop in the total variance when lower resolution data is considered. *Nel* [2015] also made use of synthetic data to investigate the affect of the drop in total variance for increasing percentages of gaps, increasing up to approximately 81% omissions where a sharp decrease was reported. That author decided that data containing beyond 75% gaps were unfit for further analysis. In this study, with the limitations of the available data, the cut-off for the percentage of gaps for a given data-interval to be used is set to 85%, since the majority of the effects imposed by data on our selected techniques stem from their resolution instead of their sparsity.

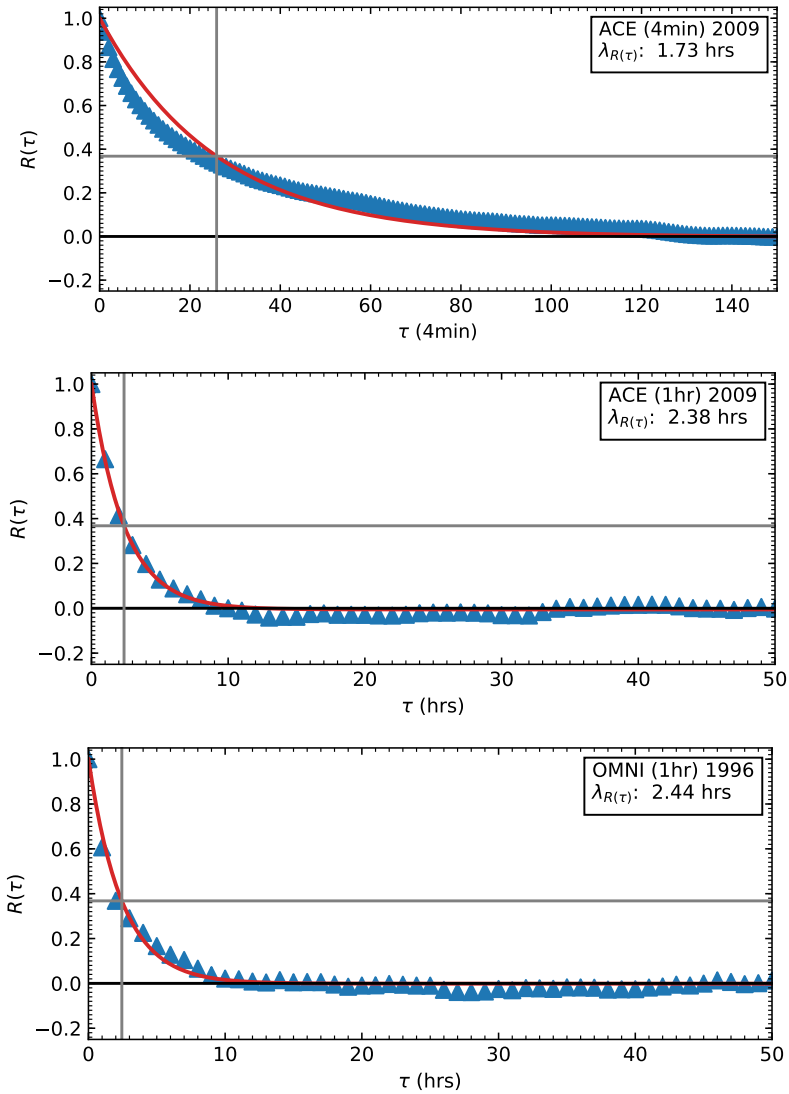

FIGURE 3.9: CFs and times of (25.90 4-minute units, equating to approximately 1.73 hrs) and (2.38 hrs) produced from 4-minute (top) and 1-hour (middle) resolution *ACE* data during 2009, and similarly constructed CF around the 1996 solar minimum, for hourly *OMNI* data (bottom) calculated and averaged over subsequent 13-day intervals. With an *e*-folding time of 2.44 hrs

The PVs and correlation lengths were determined for yearly data-sets of *OMNI* data during several solar minima to identify possible trends across minimum periods and to benchmark against possible systematic issues arising from the choice of analysis techniques made. This was also done for spacecraft data from *ACE* in 2009 to see how results compare with those from synthetic data. As such PVs and CFs were calculated, in the same manner as for the synthetic hourly resolution data, for consecutive 13-day intervals and averaged for yearly data-sets near solar minima and maxima, to show variations in results during different conditions in the solar wind. As an example Figures 3.8 and 3.9 show the PVs and CFs computed for 2009 from 4-minute and one hour resolution *ACE* data along with hourly *OMNI* 1996 results for each, respectively. The techniques show the approach toward their respective expected total variance at larger lags in Figure 3.8, with the total variance being less for the hourly results. Figure 3.9 shows the normalized two-point CFs for these resolutions with *e*-folding times of around 1.7 and 2.4 (for both *ACE* and *OMNI* results) 'hours', between the two resolutions, respectively. This agrees with the expectation that

computed correlation scales from lower resolution data are overestimated. Therefore an analysis of spacecraft data supports the conclusions drawn as to the importance of data cadence and sparsity on the techniques employed here using synthetic data.

3.7 Summary

The analyses of the unmodified synthetic magnetic field data, used in this chapter, by the PV and SSF techniques were found to behave as expected, both showing a Kolmogorov inertial range followed by a turnover and a flattening towards the approximated total variance, in the case of the PV, or twice that for the SSF. It was shown that prior averaging over the data-set, so as to effectively lower the resolution of the data, causes a drop in the values that both techniques approximate, which is in agreement with a similar inquiry by *Nel* [2015]. This lowering in resolution also smooths results at lower lag separations which abbreviates the inertial ranges of the techniques, reducing detail in this range and causing a loss of clarity as to the shape of the underlying turbulence spectrum. Both the PV and SSF seem to be relatively insensitive to omissions except at the very largest of percentages of missing data (exceeding 85%). There is however an observed fluctuation in SSF values at the highest of lags when omissions become more prevalent, while initial magnetic variances are lower in these cases for the PV technique. For spacecraft-like data, the PV technique shows a more gradual transition, taking place over a greater range of lag values, between inertial and energy-containing scales for increased gap percentages.

Data-sets of higher resolution have have more resulting points for their correlation function. This affects the exponential decline, typically causing the correlation time to approach zero more rapidly than for lower resolution data, making correlation lengthscales larger for the low resolution data. This result suggests that correlation lengthscales for hourly resolution data will be exaggerated when compared with higher resolution studies of the same time periods. Both CFs were found to be relatively insensitive to data sparsity, with the data sparsity causing fluctuations in the shape of The CF that may effect the e-folding times and thus the correlation lengthscales at the largest of omission percentages. The major observation concerning the CF here is that increased sparsity and lowered resolution tend to stretch the exponential portion of the function, thereby shifting features that may be important, such as zero-crossing scales. Analysis of hourly *ACE* and *OMNI* data, as well as of higher resolution (4 minute) *ACE* data, for significantly less sparse, more recent spacecraft observations, supports the conclusions drawn from analyses of synthetic data in terms of data resolution.

Since the PV technique retains its characteristic behaviour to a greater degree in the face of the limitations that arise from low data resolution, as opposed to the large amount of scatter present in the SSF at large lags for large percentages of omissions, it will be used to investigate the underlying turbulence in subsequent chapters. Although both CFs presented here are very similar, the direct calculation of the standard CF will be used in all analyses to follow, since this eliminates the need to compute the SSF.

Chapter 4

Turbulence Analysis of Historical Spacecraft Data

4.1 Introduction

This chapter presents the results from the analysis of spacecraft data with the analysis techniques selected in the previous chapter. Furthermore, the results here obtained are discussed and other avenues of investigation, specifically into the period of overlapping *Pioneer* data, are pursued. The first section shows tabulated results from various periods near solar minimum and maximum using hourly *OMNI* data. This also serves to set a framework for further results presented from the subsequent analysis of *Pioneer* spacecraft data. The second section shows the results calculated from *OMNI* and *Pioneer* data-sets following the rise from solar minimum in 1964 toward the polarity shift occurring at solar maximum in 1969. The final section of this chapter focuses on an analysis of the region of overlapping *Pioneer 6* and *7* spacecraft data during the 1960s.

4.2 Solar Cycle Dependence of Turbulence Quantities

The results from the chosen analysis techniques, the partial variance (PV) and standard correlation function (CF), on hourly averaged *OMNI* data near solar minima and maxima allow for comparison with published results discussed in prior chapters. Table 4.1 shows computed total variances and correlation lengths for yearly data-sets, following the same procedure as discussed in the last chapter for averaged 13-day intervals, and is accompanied by the two panels of Figure 4.1. The correlation lengths presented here were calculated after constructing CFs, examples of which can be seen in Figure 3.9. The observed solar wind speed varies by at least a factor of 2, especially during periods of solar maximum as discussed in Chapter 2, which can significantly influence the results presented in this study. Nevertheless, a long-term average value is employed here, as these effects would be smaller than those due to the resolution of the data used to calculate these correlation times. The *e*-folding time is given for each in Figure 3.9, while the values in the table have been converted to correlation lengths by multiplying the timescale with 400km.s^{-1}, representing the average solar wind speed at Earth. The first entry, 1964 is near solar minimum and has comparably lower values than the following entry from the 1970s (near maximum), for both the magnetic variance and correlation length. This compares well with the solar cycle dependent behaviour reported by *Nel* [2015] and *Burger and Engelbrecht* [2018] and suggests that the techniques yield similar trends in turbulence quantities with solar cycle as seen there. These are of course in contrast to the observations made by *Wicks et al.* [2010] and *Zhao et al.* [2018] that correlation lengths may not change much with solar cycle. The total variances appear to agree quite well with Figure 2.18, with the values being closer to the average value of approximately 11nT^2. As for the correlation times, the trend with solar cycle is apparent but the values are significantly larger than expected from Figure

TABLE 4.1: Total variances and correlation lengths computed for periods near solar minimum and maximum.

Year	$\delta B_N{}^2(nT^2)$	$\lambda_c(10^6 km)$
1964	5.43	2.376
1970	10.27	6.264
1976	5.51	3.355
1980	12.67	6.451
1986	6.87	4.838
1989	14.02	5.469
1996	4.45	3.514
2001	13.47	6.213
2009	3.06	2.750
2014	9.38	6.638

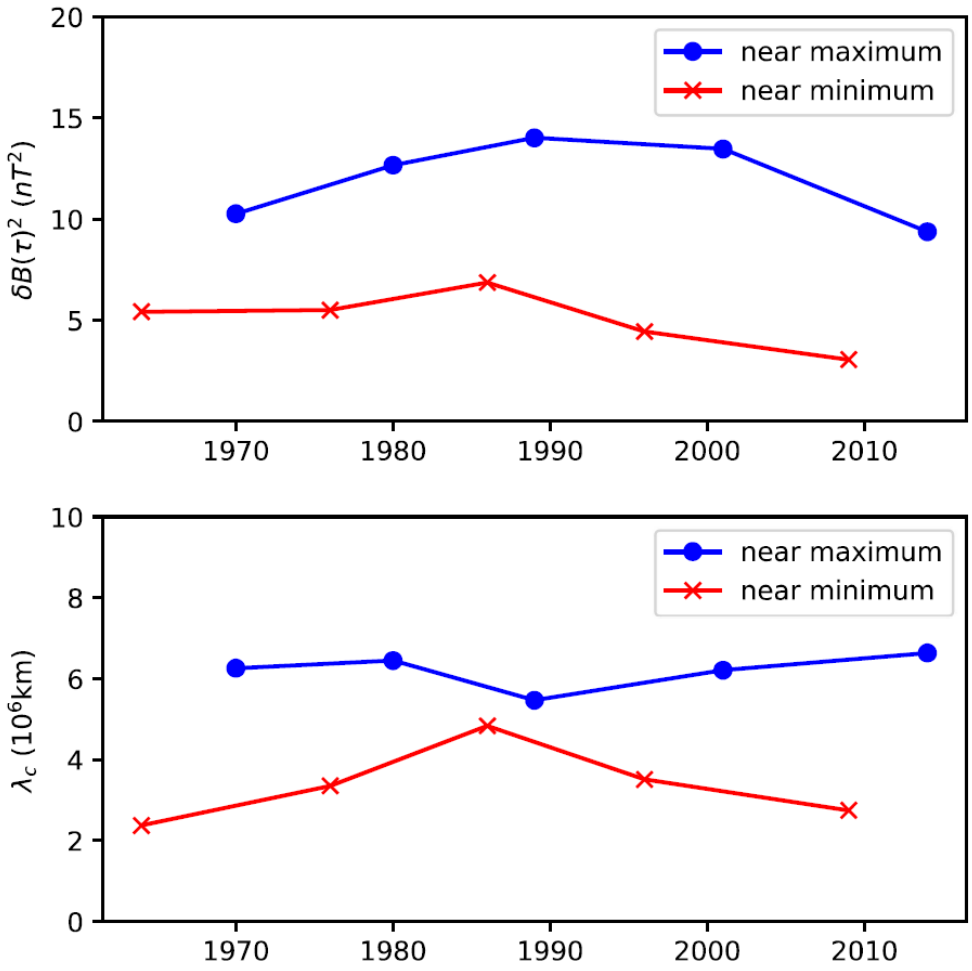

FIGURE 4.1: The top panel shows how the variance changed over time near solar maximum and minimum in blue and red, respectively. Similarly, the bottom panel shows the progression of the computed correlation scales shown in Table 4.1

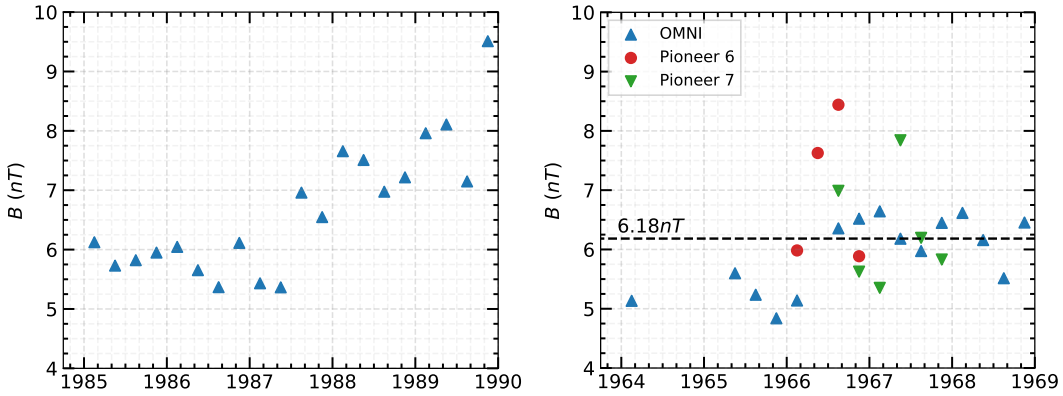

FIGURE 4.2: Three-month averaged magnetic field magnitudes from consecutive 13-day interval results from *OMNI* data in the latter half of the 1980s (left), and for *OMNI*, *Pioneer 6* and *7* data during the latter half of the 1960s (right).

2.22. From the result that the correlation lengths are overestimated by the CF applied to hourly resolution data, it is expected that correlation lengths obtained here will be larger than what is reported by studies using higher resolution data.

4.3 Early Spacecraft Data Results

This section presents the analysis of *OMNI* and *Pioneer 6* and *7* spacecraft data between 1964 and 1969, the period leading up to solar maximum polarity shift at the turn of the seventies. The years leading up to solar maximum were treated individually and analyses, using 27-day intervals and 13-day intervals of hourly *OMNI* and *Pioneer 6* and *7* data, were done to obtain 6-monthly averages. Further analysis includes 3-monthly and monthly averages in order to discern behaviour in greater detail.

Using available *OMNI* data of hourly resolution during the similar rise to solar maximum during the latter half of the 1980s (1985-1990) enables a comparison with a period of the same magnetic polarity ($A < 0$). From these results the behaviour of the period between 1964 and 1969 can be compared to a period for which the increase in magnetic field magnitude towards maximum behaves as expected. Figure 4.2 shows the averaged magnetic field magnitudes of quarterly-averaged 13-day intervals of *OMNI* (blue), *Pioneer 6* (red) and *Pioneer 7* (green) data for two five-year periods between 1985 and 1990, and 1964 and 1969, on the left and right, respectively. *OMNI* data magnetic field magnitude averages during the latter half of the 1980s (Figure 4.2) show an increase from around 5nT to 9.5nT, almost doubling the minimum value over the 5-year period to solar maximum. The magnetic field averages during the 1960s start around the same value near solar minimum, but do not show a similar increase toward solar maximum. *Pioneer 6* and *7* results over the period show a significant amount of omissions in individual 13-day intervals, reducing the number of data points their results contribute to the figure. The results from the *Pioneer* spacecraft tend to be higher or lower due to the larger number of gaps in the spacecraft data when compared with *OMNI* results. The Figure shows an average line at 6.18nT through the bulk of the average field magnitudes, which simply illustrates that the overall increase is significantly lower, at least in the latter half of the period, than seen for the results in the 1980s.

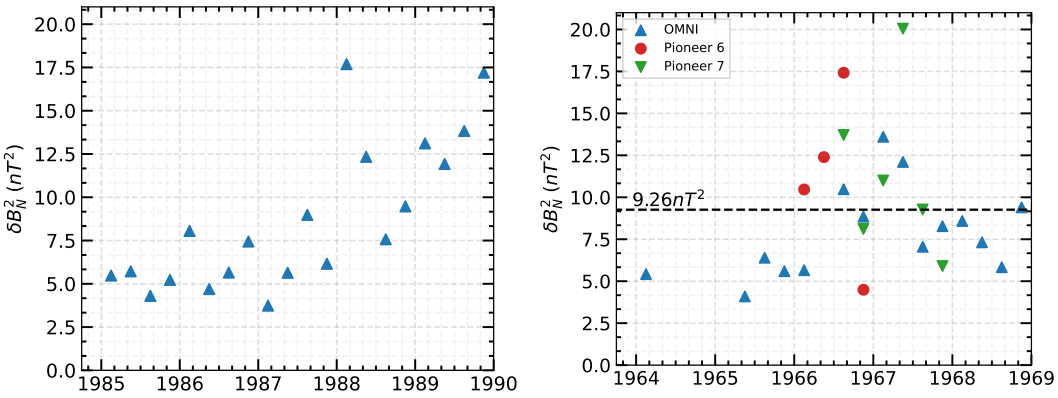

FIGURE 4.3: Three-month averaged magnetic variances from consecutive 13-day interval results from *OMNI* data in the latter half of the 1980s (left), and for *OMNI*, *Pioneer 6* and *7* data during the latter half of the 1960s (right).

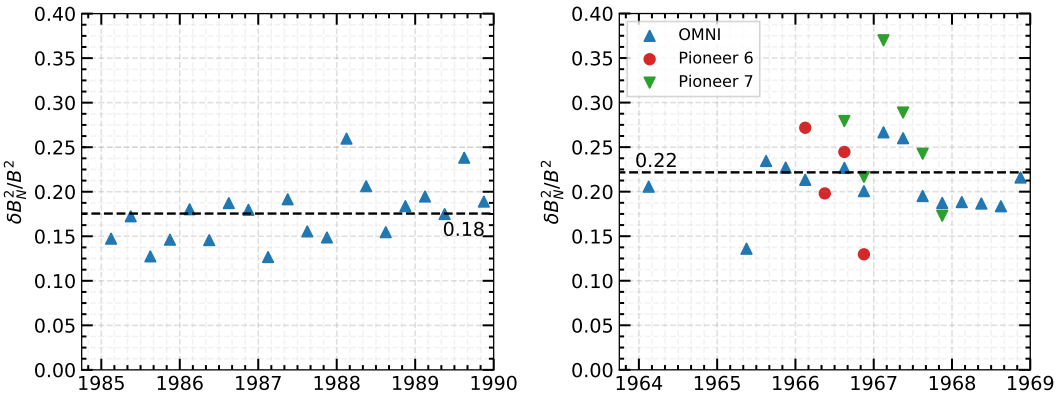

FIGURE 4.4: Three-month averaged normalized variance from consecutive 13-day interval results from *OMNI* data in the latter half of the 1980s (left), and for *OMNI*, *Pioneer 6* and *7* data during the latter half of the 1960s (right).

Figure 4.3 shows the corresponding magnetic variances for the averaged 13-day interval field magnitudes seen in Figure 4.2. The results from *OMNI* data during the 1980s show a clear increase from approximately $4nT^2$ in the first half of the 5-year period to around $17nT^2$ near solar maximum. Results during the 1960s show an increase from a similar initial variance toward the middle of the period in question before remaining fairly consistently below $10nT^2$ during the latter half of the interval. Here the effects of resolution and sparsity can be seen to affect the *Pioneer* data results, causing what points remain in Figure 4.3 to vary to a greater degree. The magnetic variances in Figure 4.3 reflect the behaviour of the magnetic field magnitudes in Figure 4.2, as expected due to the fact that the two quantities have been previously observed to track each other well (see Chapter 2, Figure 2.17 and *Matthaeus et al.* [1986]).

Figure 4.4 illustrates the normalized variance $\delta B_N^2/B_{mag}^2$, a ratio between the quantities in Figures 4.2 and 4.3. The ratios remained roughly constant during the 1960s and 1980s, with average values of 0.22 and 0.18, with an approximate 20% difference between them, making these results similar over the two time periods.

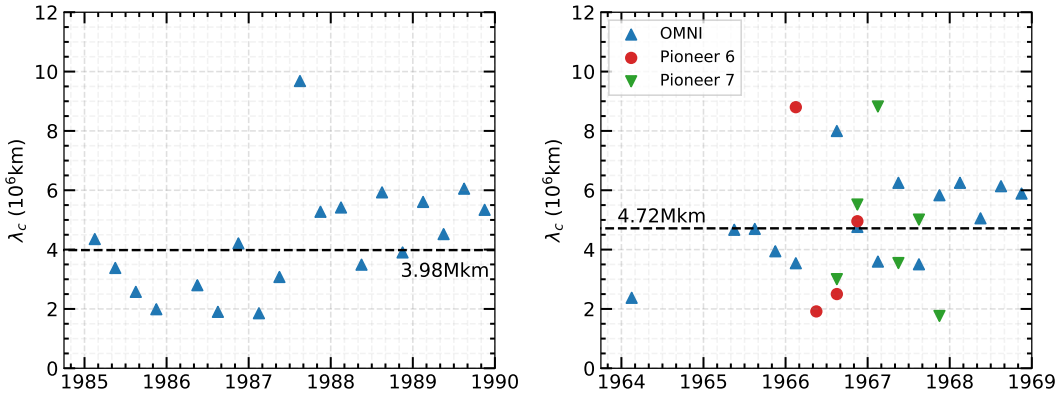

FIGURE 4.5: Three-month averaged correlation lengths from consecutive 13-day interval results from *OMNI* data in the latter half of the 1980s (left), and for *OMNI*, *Pioneer 6* and *7* data during the latter half of the 1960s (right).

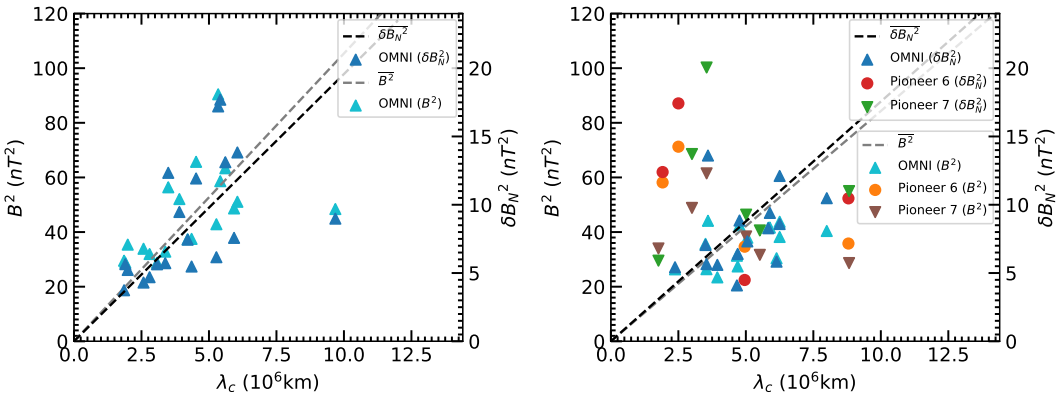

FIGURE 4.6: Squared magnetic field magnitudes and magnetic variances as a function of the correlation length, for 1980s (left) and 1960s periods (right). The grey and black dashed lines are average variance regression lines, forced through the origin, for the squared magnetic field magnitudes and variances.

Figure 4.5 shows corresponding correlation lengths over both periods. The values are expected to be overestimated due to data omissions and cadence, and the use of the chosen analysis techniques, as discussed previously. The overall behaviour does, however, fit the expected trend of an increase in correlation scale toward solar maximum, with results from the latter part of both time periods considered here being greater by at least a factor of two than the lowest values in the first half of the respective periods. This result is similar to what was reported by *Burger and Engelbrecht* [2018], and the trend with increase toward solar maximum for both periods is quite similar in Figure 4.5. The average correlation lengths of turbulent fluctuations over both periods are around $\sim 3.98 \times 10^6$km and $\sim 4.72 \times 10^6$km for the 1980s and 1960s data, respectively.

Figure 4.6 shows the behaviour of magnetic variances and magnetic field magnitudes with increasing correlation length. The *OMNI* variances and field magnitudes are represented by the blue and cyan triangles, for both periods, respectively. Similarly, the *Pioneer 6* and *7* data are shown in variance and magnetic field pairs red and orange circles, and green and brown down triangles, respectively. The scales for the magnetic field magnitude are on

the left-hand axis of each figure with the variance axis on the right hand side. The black and grey dashed lines are average regressions, forced through the origin, of variance and field magnitudes as function of the correlation length. The figures were constructed and presented in this manner, in order to compare the behaviour of the computed quantities with correlation length to those presented and discussed in Figure 2.23 in Chapter 2. The results presented in a similar manner here, also show a possible linear relationship between both the variance and square of the magnetic field, and the computed correlation length. Both quantities presented in the panels show significant scatter with the period during the 1960s having a higher degree of scatter when compared with the 1980s results. When focusing on *OMNI* data during both periods it is seen that a similar relationship exists for the increase in magnetic field magnitude and variance results with correlation lengthscale. This correlation between magnetic variance and correlation scale implies that both the magnetic field magnitude and variance should indeed show similar behaviour with solar cycle. In Figure 4.6 the *OMNI* results in the 1960s are lower overall when compared to the results from the 1980s, with the *Pioneer* results showing significant scatter, independent of the resolution effects on the data, since the 1980s data is of the same hourly resolution.

The degree to which the computed turbulence quantities differ between the two $A < 0$ time periods is presented in Figures 4.2 through 4.5. Excluding the normalized variance, which remains constant if the variance and field magnitude track each other, the increase towards the expected behaviour at solar maximum is seen from the turbulence analysis of the data in all of these figures. Variance, magnetic field magnitude and correlation lengths increase significantly throughout the late 1980s. This not so clearly seen in the same quantities during the latter part of the 1960s. Comparatively, turbulence quantities observed during the 1980s and 1960s differ in that those computed during the former period increase towards solar maximum, while those determined for the latter period appear not to. However, the turbulence quantities computed for both periods appear to track the behaviour of δB^2 and B^2 consistently, as evidenced by the relatively constant behaviour of the ratio $\delta B^2/B^2$, and the panels of Figure 4.6.

4.4 A Closer Look at *Pioneer 6* and *7* Observations

The *Pioneer 6* and *7* spacecraft were both operational for an overlapping period of time within the early period of interest to this study, which could conceivably allow for a limited comparison between the resulting turbulence quantities that are observed there. Such an analysis could be used to compare behaviour of turbulence quantities, not only in this early period of SW observations, but also at slightly different heliocentric distances. This would also allow for investigation as to the possible cause of some of the unexpectedly high variances in the results from the previous section. Regarding those results, there are two large heliospheric magnetic field (HMF) magnitudes contributed by *Pioneer 6* to Figure 4.2 that are most likely due to the small number of viable 13-day intervals available for averaging in that specific section of data. *Pioneer 7* contributions to Figure 4.3 are remarkably well behaved when compared to those from the other spacecraft. A possible reason for the largest value it contributes, near 8nT in the second quarter of 1967, is the occurrence of a known massive solar event in the month of May [see, e.g., *Lindgren*, 1968; *Knipp et al.*, 2016]. This spike in the *Pioneer 7* results is not discernible in *OMNI* data. It is known that *Pioneer 7* was magnetically well connected to the solar origin of the event and observed increased energetic proton flux considered to be due to the increased activity in the solar region at the time [see, e.g., *Knipp et al.*, 2016]. The question arises whether the increased magnetic field magnitude coupled with the increased variance for the same

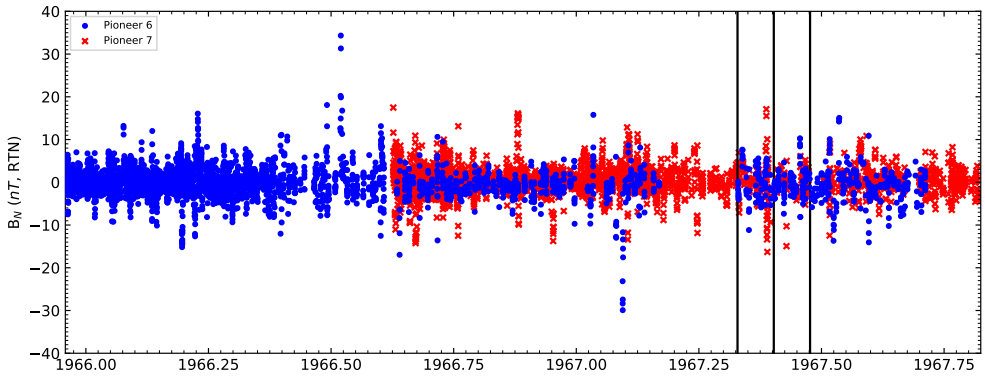

FIGURE 4.7: *Pioneer 6* and *7* N-component observations in blue and red respectively, the black vertical lines indicate the period of overlapping data around the massive solar event in the second quarter of 1967.

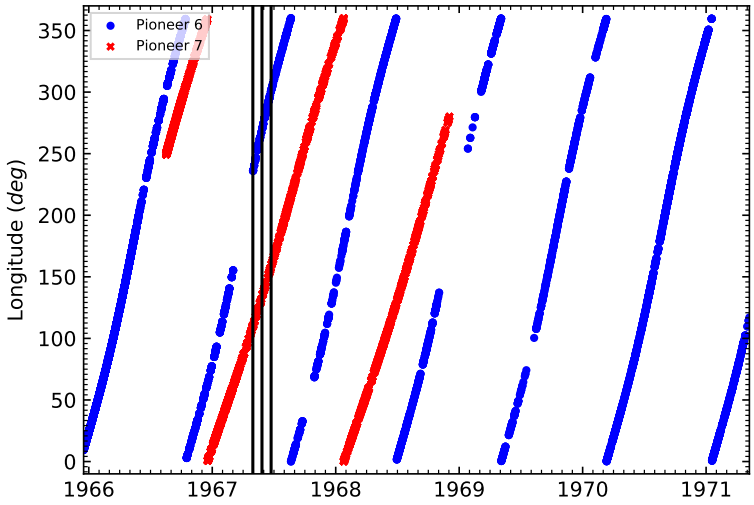

FIGURE 4.8: Spacecraft longitudes from the *Pioneer* spacecraft, with period selected for the solar event seen in Figure 4.7.

period in Figure 4.3, in the region of *Pioneer 7*, implies the observation of a large scale solar event through magnetic field data instead of by particle data. It should be mentioned, however, that during coronal mass ejections and/or other transient phenomena, the Parker HMF geometry is greatly disturbed and a very significant theta component to the field usually develops, which may strongly influence the analysis presented here. Therefore further study of these phenomena is required.

This section investigates what can be learnt from turbulence analysis targeting the *Pioneer* data in greater detail. Figure 4.7 shows all of the available *Pioneer 6* and *7*, N-component magnetic field data used in the study. This illustrates the (in)completeness of the data-sets, as a large gap in *Pioneer 6* observations is clearly visible prior to the first of May, which is the first vertical line from the left in Figure 4.7. The last vertical line from the left is 54 days later, on the 24th of June 1967, which provides a decent-sized interval centered on the 28th of May that will be used to study the well-documented solar event. Due to the low resolution of these data such a large interval was necessary to obtain sufficient information from the period in question. Figure 4.8 shows available longitude records from both spacecraft for

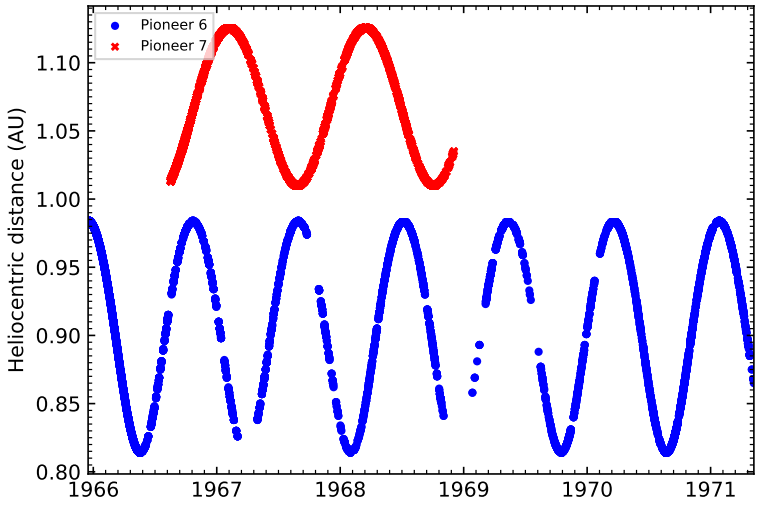

FIGURE 4.9: Heliocentric distance of both *Pioneer* spacecraft from available data.

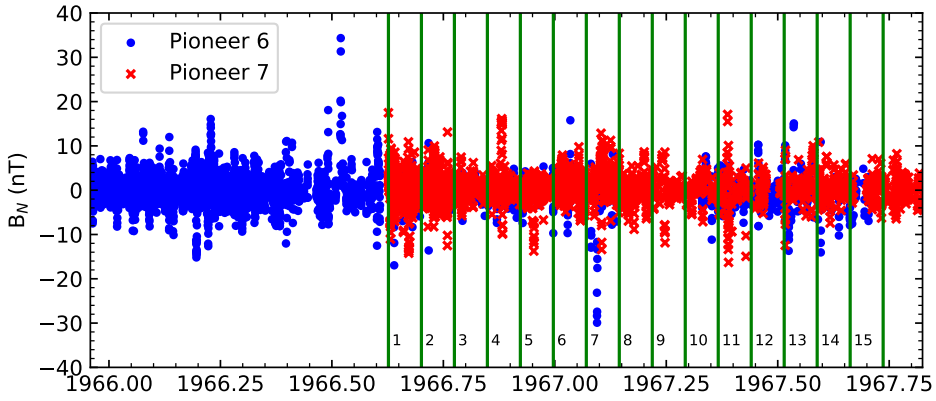

FIGURE 4.10: *Pioneer 6* and *7* magnetic field spacecraft data with 27-day interval divisions for use in this section. Intervals start where the overlapping part of *Pioneer* data commences.

the available data. The longitude records for the spacecraft are more complete than the magnetic field observations. Figure 4.9 show respective heliocentric distance records for both spacecraft and together with Figure 4.8 this gives an idea of the relative positions of the spacecraft, with *Pioneer 6* and *7* having average orbits at radial distances of 0.88AU and 1.06AU.

For the purposes of this investigation, the overlapping portions of *Pioneer 6* and *7* data were divided into 27-day intervals as shown in Figure 4.10. Analysis of 13-day intervals seemed to lack the necessary number of viable data points to achieve statistically significant variance averages, while 54-day intervals smooth the computed averages and to a large extent make specific event periods more difficult to distinguish from what could be considered normal behaviour. Figure 4.11 shows the averaged variance results for the 15 intervals of 27-day *Pioneer 6* and *7* data. The horizontal dashed line in Figure 4.11 represents the average magnetic variance recorded for the *Pioneer* spacecraft data. The solid vertical black lines are bounds set for what is considered to be the period of increased

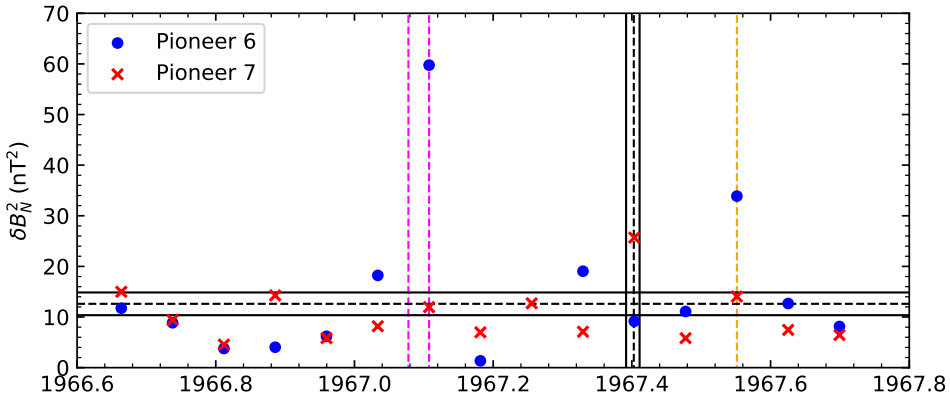

FIGURE 4.11: 27-day variance averages for the intervals shown in Figure 4.10, with horizontal average lines and positions of intervals well above average marked with the vertical dashed lines. The first of these events represents the seventh interval in Figure 4.10, while the second and third result from the eleventh and thirteenth intervals respectively.

solar activity corresponding to the 21st and 28th of May 1967 respectively, where between these dates multiple flare events initiated by solar storms originating from McMath region 8818 occurred [see, e.g., *Lindgren*, 1968; *Akasofu et al.*, 1969; *Knipp et al.*, 2016]. The dashed black line shows the 25th of May, which is the specific date of the large solar storm recorded during that period at Earth. The *Pioneer 7* result for the magnetic variance during this event period (the 11th interval in Figure 4.10) is significantly higher than average. In addition to the large magnetic variance calculated around this event, two other large deviations are illustrated by the dashed magenta and yellow lines, both of which correspond to large *Pioneer 6* results. After collating average magnetic variances over *Pioneer 6* and *7* data for similar longitudes and different radial distances, so that a function could be fit between values affected only by a radial separation between the spacecraft, the variance was found to scale as $\sim r^{-2.2}$, a result qualitatively in agreement with, albeit slightly less steep than, the radial dependence of this quantity seen in Voyager data at greater radial distances by *Zank et al.* [1996]. Nevertheless, it is important to note that this result is relatively uncertain due to the small radial separation between the two spacecraft. No significant periodicities were determined in the turbulence quantities for the data analysed here.

The first, and undoubtedly the largest of the variances, results from the seventh interval in Figure 4.10, which may be due to the associated coronal mass ejection of a solar flare event that occurred on the 28th of January 1967, and is thoroughly discussed by *Bukata et al.* [1969]. The last of the three high variances corresponds to the thirteenth of the intervals 4.10 and there is no major event recorded in the literature at the time which presents itself as an immediate cause, though it should be noted that the longitude difference between *Pioneer 6* and the Earth may suggest that an event occurred that was more prominent from the spacecraft's position, i.e. the event did not extend to the position of Earth or *Pioneer 7*. The *Pioneer* spacecraft's positions with respect to the Earth are shown in Figure 4.12, where the intervals of interest are labeled from 1 through 3. In this polar plot the filled areas, in order from the center, represent the bounds of the orbits of *Pioneer 6*, the Earth and *Pioneer 7*. Figure 4.12 shows that the longitude separation between both of the *Pioneer* spacecraft and the Earth was increasing during the course of the overlapping period of magnetic field data in 1967. Note that the positions of these spacecraft were taken from the same data-sets as for all other analyses, while Earth ephemeris data were taken from NASA's SPDF service at

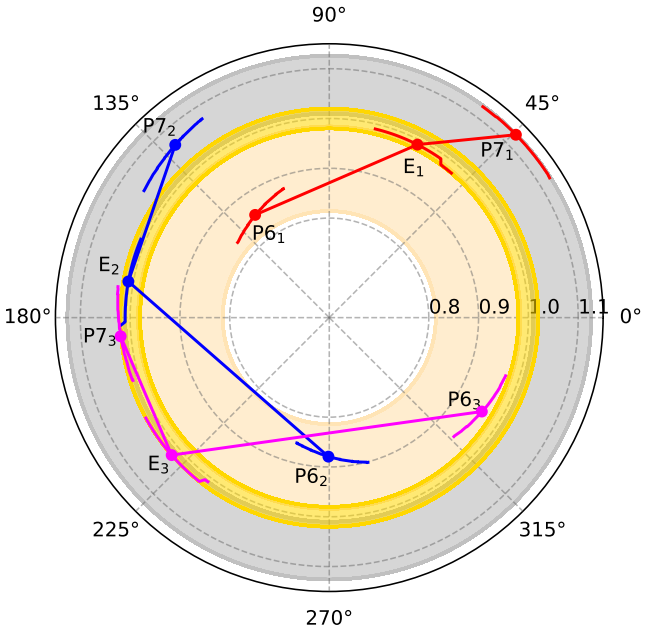

FIGURE 4.12: Polar plot of *Pioneer* spacecraft and the Earth's average positions during the three event time periods identified in Figure 4.11. The intervals are labeled with subscripts 1, 2 and 3 relating the chronological order in which they appear in Figure 4.11. The three colour bounds within the figure show the minimum and maximum heliocentric distance of *Pioneer 6*, the Earth and *Pioneer 7*, in that order from the interior outward. The spacecraft and the Earth's positions are connected with a same-colour line for each event in order to more clearly show the change in distance between the three.

https://omniweb.gsfc.nasa.gov/. The large separations in longitudes between the relevant observers suggest that for even the largest of solar events only some of the observers may encounter a specific solar event, should one have occurred. Such is probably the case for the first of these events, a solar flare event described by *Bukata et al.* [1969], as having occurred well beyond (approximately 60°) the western limb of the sun. As mentioned by *Bukata et al.* [1969], high energy flare events typically have short durations and a visible associated plage region, this latter feature not being the case for the one described there. Given the relative postitions of the *Pioneer* spacecraft and Earth in Figure 4.12, it is clear that the first event, detected at *Pioneer 6*, was not of sufficient extent to be detected at Earth or at *Pioneer 7*. Although the Sun may have had interesting events occurring at its surface, it proved difficult to determine a clear source event and date for the third event shown in Figure 4.11. With the positions for that specific 27-day interval shown in Figure 4.12 and *Pioneer 6* being separated from the Earth to an even greater extent than the first event, it is likely that *Pioneer 6* might have been the only observer of a similar solar event, well beyond the western limb of the Sun. The large longitude separation of around 107° from the Earth suggests that the third event may have originated from solar activity beyond the visible solar disk. The solar storms occurring during the latter part of May in 1967, and observed from Earth and by the magnetically well connected *Pioneer 7*, were clearly associated with McMath region 8818 visible on the solar disk [*Knipp et al.*, 2016]. The average longitude separation between the Earth and *Pioneer 7* for the May 1967 event period was ~ 38°, and since particle detections were made at both, this number can serve as a minimum lengthscale for the extent of the solar event, which would correspond to an arc length of ~ 0.66AU at 1AU. At the time *Pioneer 6* was approximately 100° away from the Earth, and since the analysis

done here does not indicate a significant increase in variance over the event period for this spacecraft, and no energetic particle increases have been reported for this spacecraft, it can be concluded that the event did not extend so far as to be detected by both spacecraft.

The panels of Figure 4.13 show the results from the PV technique applied to each 27-day event interval corresponding to the periods of events 1 through 3. While there are no clear changes in shape to the variance spectrum from nonevent intervals, a clear enhancement of the spectrum is seen for the specific spacecraft that saw increased energetic particle fluxes during event periods. The first and second panels have a larger total variance for *Pioneer 6* and *Pioneer 7* respectively, in agreement with the fact that those spacecraft were in preferential positions to detect those events at those specific time periods. The third panel shows a larger result for *Pioneer 6* magnetic variances, and shows similar behaviour to that recorded during the first event period, even though no increases in energetic particle fluxes were recorded, at least in the literature, for this spacecraft. The hallmark of a passing event would then be a significant increase in turbulence levels.

4.5 Summary

Analysis of hourly resolution, yearly spacecraft data-sets near solar minimum and maximum over several solar cycles by the techniques selected in Chapter 3 shows a solar cycle dependence in turbulence quantities, δB^2 and λ_c, in qualitative agreement with *Nel* [2015] and *Burger and Engelbrecht* [2018], with the solar cycle dependence of the variance being in qualitative agreement with *Zhao et al.* [2018]. In this Chapter the behaviour of turbulence quantities during the rise from solar minimum to solar maximum during the 1960s was compared to that of the 1980s, due to the fact that the behaviour during the 1980s is considered to be typical, and that this period is of the same heliospheric magnetic polarity (A<0). Comparing the results for turbulence quantities from these two periods shows that those resulting from the 1980s tend to increase towards solar maximum while those computed for the 1960s appear not to. Although their values differ, a similar trend can be seen for magnetic field magnitudes and variances for each period, which is reflected by the roughly constant ratios of $\delta B^2/B^2$ in Figure 4.4 that differ only by $\sim 20\%$ between the two periods.

As expected from the results of the previous chapter, the correlation lengthscales resulting from these analyses are overestimated, but they appear to increase by around a factor of two between solar minimum and maximum. The turbulence quantities obtained for both the 1960s and 1980s track the behaviour with B^2 consistently as shown by the behaviour of $\delta B^2/B^2$ and the Figure 4.6.

A deeper look into *Pioneer 6* and *7* data during the period of time that they were both operational, revealed three intervals with large variances. Two of these intervals were found to correspond to known solar events in the literature, raising the possibility that the third corresponds to a previously unknown event. The two known events correspond to the solar flare on the 28th of January 1967 discussed by *Bukata et al.* [1969], and the period of heightened solar activity and solar storms during May of the same year [*Knipp et al.*, 2016]. By collating average magnetic variances of *Pioneer 6* and *7* data for similar longitudes, a simple calculation of the radial dependence of magnetic variance was found to scale as $\sim r^{2.2}$, which qualitatively agrees with the result presented by *Zank et al.* [1996]. Additionally, no significant periodicities were determined in turbulence quantities in the overlapping portion of *Pioneer 6* and *7* data.

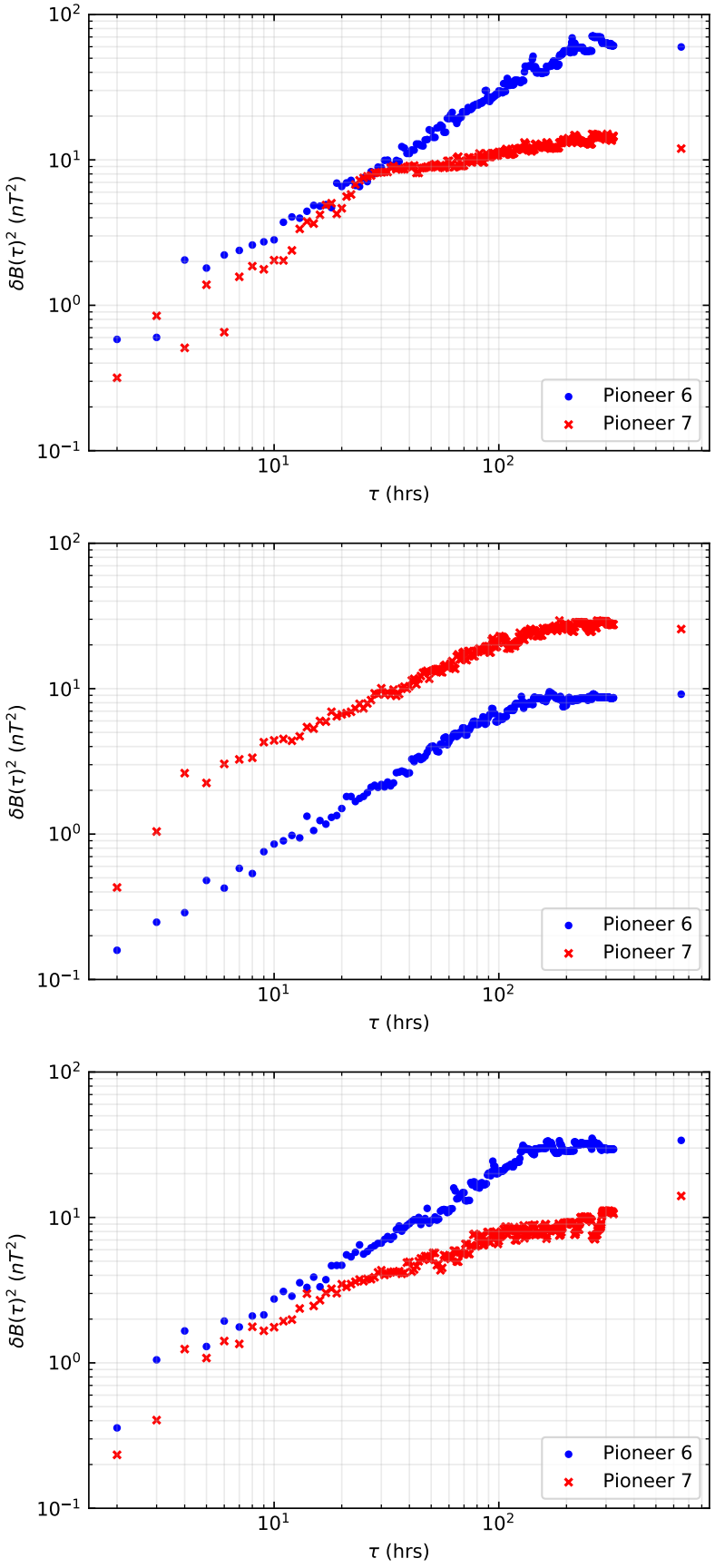

FIGURE 4.13: The results for the PVT applied on each of the 27-day intervals of interest, identified in Figure 4.11. These PVs are calculated in the same fashion as in prior results. The results show an overall enhancement of magnetic variance for the spacecraft that shows a peak in Figure 4.11, but no clear difference in the partial variance spectrum's shape.

Chapter 5

Cosmic-Ray Transport Coefficients and Modulation

5.1 Introduction

Given the behaviour of the turbulence quantities and heliospheric magnetic field (HMF) magnitude from the comparison of data from the 1960s and 1980s made in the previous chapter, the question arises as to the effect they may have on galactic cosmic-ray (CR) transport coefficients. Any change in diffusion and drift coefficients of CR particles would affect observed intensities at Earth by neutron monitors (NMs), and thus would shed light as to the reasons underlying the unexpected relationship between observed HMF magnitudes and CR intensities in the 1960s. One of the aims of this final chapter is then to compare transport coefficients for the periods of solar minimum and ascending to solar maximum during the 1960s and 1980s, calculated by use of the turbulence quantities gleaned from the preceding chapters. The 1980s is selected for this comparison since CR intensities and HMF magnitudes during in this period are considered to have behaved in a more typical manner (see Figure 2.9 in Chapter 2), as well as the fact that the two periods are both of negative heliospheric magnetic polarity ($A < 0$), to eliminate any possible effects due the HMF polarity.

This chapter begins with a brief introduction of the transport coefficients to be considered in this part of the study. An in-depth treatment of these coefficients, as well as the scattering theories they are derived from, is beyond the scope of this work. The interested reader is referred to, e.g., *Shalchi* [2009]; *Engelbrecht et al.* [2017]; *Shalchi* [2020a] for more thorough discussion of these topics. Given the limitations implicit to the use of the selected data analysis techniques previously discussed in terms of ascertaining accurate turbulence correlation lengthscales, a re-normalisation technique based on results for this quantity presented by various studies using more recent, multiple spacecraft data analysis techniques [see, e.g., *Wicks et al.*, 2010; *Weygand et al.*, 2011] will be introduced here. This is done in order to model this turbulence quantity as input for the transport coefficients for the time period of interest to this study, as potentially unrealistically large correlation scales would lead to potentially unrealistic diffusion coefficients. A study of the parallel and perpendicular diffusion coefficients, as well as drift coefficients calculated by use of the results presented in this study will follow. Then, using these results as effective values for all plasma quantities affecting the transport of CRs, their differential intensities can be computed on a year-by-year basis using the stochastic 3D *ab initio* modulation code presented by *Engelbrecht and Burger* [2015b]. The chapter ends with a discussion of the results of these calculations, and the implications they have for our understanding of CR modulation during the 1960s. The majority of the results presented here were published by *Engelbrecht and Wolmarans* [2020].

5.2 Computing Transport Coefficients

Many theories have been proposed to describe how charged particles are scattered in turbulent magnetic fields [see, e.g., *Shalchi*, 2009], but the expressions that they provide for parallel and perpendicular (to the background HMF) diffusion coefficients are usually quite complicated [see, e.g., *Engelbrecht and Burger*, 2013, 2015b; *Strauss et al.*, 2016; *Dempers and Engelbrecht*, 2020]. The transport coefficients chosen in this study will be those used by e.g. *Burger et al.* [2008]; *Moloto et al.* [2018, 2019]; *Caballero-Lopez et al.* [2019], and *Moloto and Engelbrecht* [2020]. These expressions are in reasonable agreement with numerical test particle simulations of diffusion and drift coefficients [see, e.g., *Minnie et al.*, 2007a,b; *Tautz and Shalchi*, 2012; *Shalchi*, 2020b] and when used in a CR modulation code, these expressions also lead to computed differential intensities that are in reasonable agreement with spacecraft observations over several solar cycles [see, e.g., *Moloto and Engelbrecht*, 2020].

The quasilinear theory expression proposed by *Burger et al.* [2008] that was constructed under the assumption of composite slab/2D turbulence [see, e.g., *Bieber et al.*, 1994] from the analytical expressions derived by *Teufel and Schlickeiser* [2003] models the proton mean free path (MFP) parallel to the HMF and is given by

$$\lambda_{\parallel} = \frac{3s}{(s-1)} \frac{R^2}{k_m} \frac{B_o^2}{\delta B_{slab}^2} \left[\frac{1}{4\pi} + \frac{2R^{-s}}{\pi(2-s)(4-s)} \right]. \tag{5.1}$$

This MFP was derived assuming a magnetostatic slab turbulence power spectrum with a *Kolmogorov* [1941] inertial range with spectral index $s = 5/3$ and a wavenumber-independent energy range (see Chapter 2), with the ranges transitioning at $k_m = 1/\lambda_{slab}$. Equation 5.1 is related to the diffusion coefficient by $\kappa = v\lambda_{\parallel}/3$. Furthermore, the quantity R is related to the maximal proton Larmor radius R_L by $R_L k_m$. Eq. 5.1 has often been used in *ab initio* CR modulation studies [e.g. *Engelbrecht and Burger*, 2013, 2015b]. Electron MFP expressions are affected by quantities relating to the dissipation range of the power spectrum *Bieber et al.* [1994], but not proton parallel MFP expressions [see, e.g., *Engelbrecht*, 2019], and thus will not be considered here.

The *Matthaeus et al.* [2003] nonlinear guiding centre theory expression for the MFP perpendicular to the field, modified by *Burger et al.* [2008] from *Shalchi et al.* [2004] to allow a variable ratio of slab and 2D variance, will be used in this part of the study. The perpendicular MFP expression, for a 2D turbulence power spectrum with a wavenumber-independent energy-containing range and a *Kolmogorov* [1941] inertial range, is then

$$\lambda_{\perp} = \left[\alpha^2 \sqrt{3\pi} \frac{2\nu - 1}{\nu} \frac{\Gamma(\nu)}{\Gamma(\nu - 1/2)} \frac{\delta B_{2D}^2}{B_0^2} \lambda_{2D} \right]^{2/3} \lambda_{\parallel}^{1/3}, \tag{5.2}$$

where $\nu = |s|/2$ and $\alpha^2 = 1/3$ [see *Matthaeus et al.*, 2003]. Note that a similar expression to Eq. 5.2 derived by *Zank et al.* [2004] is employed by *Zhao et al.* [2018] in their study of the solar cycle dependence of CR diffusion MFPs. These MFP expressions are shown as function of rigidity at Earth in Figure 5.1 (taken from *Caballero-Lopez et al.* [2019], using the values for the various turbulence quantities used by *Burger et al.* [2008]. The rigidity of a charged particle P is a measure of its resistance to deflection by a magnetic field based on its momentum, in this case the Parker HMF introduced in Section 2.4, and has units of energy per unit charge (GV) [*Moraal*, 2013; *Caballero-Lopez et al.*, 2019]. The *Palmer*

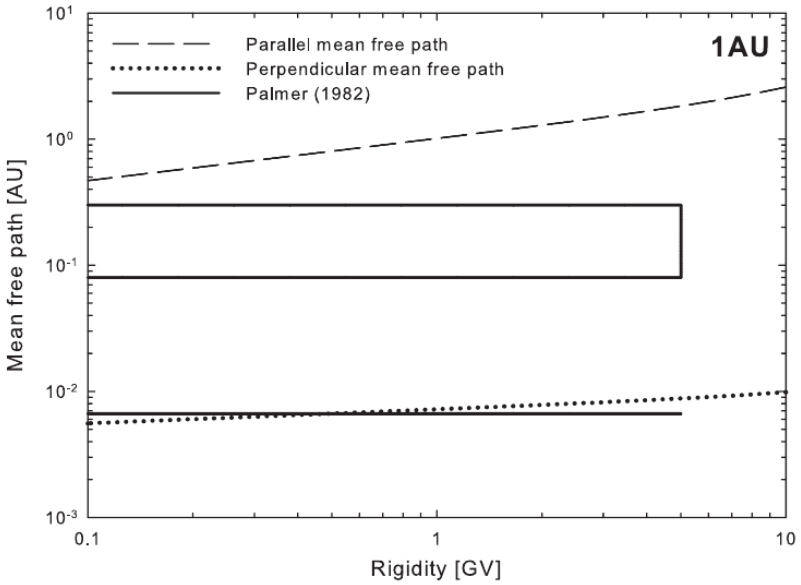

FIGURE 5.1: The parallel and perpendicular MFPs used here as function of rigidity at 1 AU, and computed using turbulence parameters as discussed by *Burger et al.* [2008]. The figure includes the *Palmer* [1982] consensus range values for these MFPs. Figure taken from *Caballero-Lopez et al.* [2019].

[1982] consensus range of values for MFPs at 1 AU are also included in the figure. It is to be noted that the MFPs in Figure 5.1 serve only as examples and that they would change as the turbulence quantities are changed. The parallel MFP exhibits the expected $\sim P^{1/3}$ dependence at these rigidities, while the perpendicular MFP displays an almost flat rigidity ($\sim P^{1/9}$) dependence. It is important to note that $\lambda_\perp$ is a function of $\lambda_\parallel^{1/3}$ of the parallel MFP (Eq. 5.1) from which it gains this rigidity dependence.

Cosmic-ray drifts in the heliosphere, due to gradients and curvatures such particles encounter in the HMF, as well as along the heliospheric current sheet (HCS), are reduced by sufficiently high levels of turbulence [e.g. *Bieber and Matthaeus*, 1997; *Burger et al.*, 2000; *Minnie et al.*, 2007b; *Burger and Visser*, 2010; *Tautz and Shalchi*, 2012; *Engelbrecht and Burger*, 2015a; *Engelbrecht et al.*, 2017, and references within]. In zero or weak scattering conditions, the drift lengthscale λ_D, related to the drift coefficient by $\kappa_A = v\lambda_D/3$, is equal to the maximal CR Larmor radius R_L [e.g. *Forman et al.*, 1974]. The expression for the turbulence-reduced drift scale used here was derived by *Engelbrecht et al.* [2017]. This expression provides results in agreement with the simulations of *Minnie et al.* [2007b]; *Tautz and Shalchi* [2012], and is given by

$$\lambda_D = R_L \left[1 + \frac{\lambda_\perp^2}{R_L^2} \frac{\delta B_T^2}{B_0^2} \right]^{-1}, \tag{5.3}$$

with $\delta B_T^2 = \delta B_{slab}^2 + \delta B_{2D}^2$ the total magnetic variance. The above expressions require realistic inputs for the magnetic variances and correlation scales. While the data analysis techniques outlined in the previous chapters provide acceptable values for the former quantity, the correlation scales they yield remain too large when compared with results reported by more recent studies that employ higher resolution data [e.g. *Wicks et al.*, 2010; *Weygand et al.*, 2011]. In order to adequately estimate the behaviour of the MFPs and drift scale, a viable estimation of the values of the correlation scales during the periods of interest needs to be calculated. This is the subject of the next section.

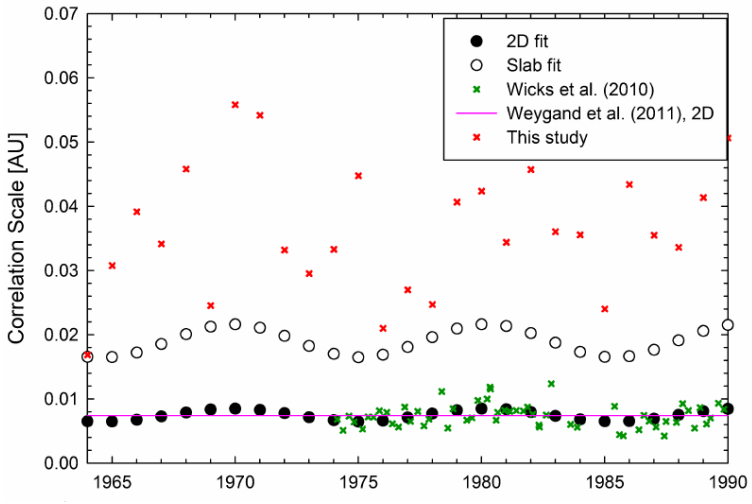

FIGURE 5.2: The correlation lengthscales computed here and those presented by *Wicks et al.* [2010], along with fits for slab and 2D correlation scales that will be used in later sections. This figure was presented by *Engelbrecht and Wolmarans* [2020].

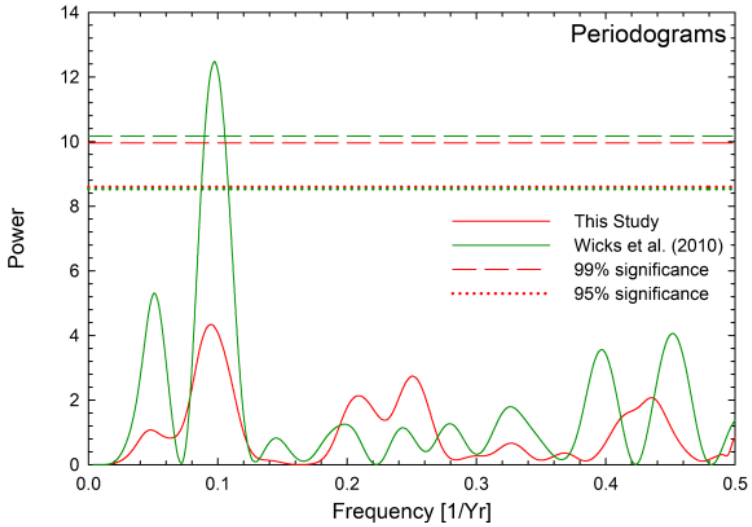

FIGURE 5.3: Lomb periodograms constructed from correlation lengthscales (those in Figure 5.2) presented here (red line) and those from *Wicks et al.* [2010] (green line). This figure was was taken from *Engelbrecht and Wolmarans* [2020].

5.3 An Appropriate Estimate for Correlation Scales

From early on in this study it has been made clear that use of lower resolution data yields correlation scales that differ significantly from what may be expected for the characteristic length scale of turbulence. Furthermore the time dependence for these correlation scales produced in this study, while in agreement with the solar cycle dependent behaviour shown by *Burger and Engelbrecht* [2018], may have suffered from an exaggeration of this quantity. This means that, in order to obtain realistic results from solutions to a CR modulation code, a more realistic approach to the correlation lengthscale is necessary, one which does not use the results of the analyses of the previous chapters as a basis.

Wicks et al. [2010] calculated correlation lengthscales as function of time from higher (1 minute) resolution spacecraft observations. Specifically *IMP8*, *ISEE3* and *OMNI* data were used. Figure 5.2 shows the correlation scales calculated in this study as well as those digitized from the results presented by *Wicks et al.* [2010]. From the figure it is clear that the correlation scales produced here are much larger by comparison. According to *Matthaeus et al.* [2005], where a multi-spacecraft analysis of correlation scales was presented, those authors reported a difference by a factor of 2-4 to many results reported from single spacecraft data analysis, regardless of resolution. Figure 5.3 shows the Lomb-Scargle periodograms produced from these two sets of correlation lengthscales. The results presented here show a peak at a periodicity of around 10.4 years, but this peak is well below the 95% significance level. On the other hand, the periodogram produced from the *Wicks et al.* [2010] results has a peak at around 10.2 years, well above the 99% significance, which is not reported in that study, but is mentioned by *Burger and Engelbrecht* [2018]. Due to the aforementioned problems with the correlation lengthscales presented here, the period of 10.2 years obtained from *Wicks et al.* [2010] data was used to construct a simple sinusoidal function of time, fit to that data and extrapolated back into the latter part of the 1960s. As the average value for the *Wicks et al.* [2010] results is close to the 0.0074 AU reported by *Weygand et al.* [2011] for the 2D correlation scale, the assumption was made that the fit to the *Wicks et al.* [2010] data corresponds to the 2D scale and that the slab correlation scale may be computed from it by multiplication of the factor 2.55 reported by *Weygand et al.* [2011] for the ratio of these lengthscales. Figure 5.2 shows yearly-averaged slab and 2D correlation scales produced from the sinusoidal fit to *Wicks et al.* [2010] data as discussed and extrapolated to the earlier periods of interest in this study.

5.4 Extrapolating Values of Turbulence Quantities Throughout the Heliosphere

Turbulence quantities such as magnetic variances and correlation scales can vary considerably throughout the heliosphere [see, e.g., *Zank et al.*, 1996; *Smith et al.*, 2001; *Bruno and Carbone*, 2013], it is therefore reasonable to expect that CR transport coefficients that depend on these quantities would also vary considerably [see, e.g., *Bieber et al.*, 2004; *Burger et al.*, 2008; *Engelbrecht and Burger*, 2015b]. It is not a straightforward exercise to model the spatial dependences of turbulence quantities in a self-consistent way, as this requires the solution of complicated turbulence transport models [see, e.g., *Breech et al.*, 2008; *Oughton et al.*, 2011; *Wiengarten et al.*, 2016; *Adhikari et al.*, 2017; *Zank et al.*, 2018], which is beyond the scope of this work. An alternative approach is to model the spatial dependences of variances and correlation scales using simple, observationally and theoretically motivated power laws, an approach taken by, e.g., *Burger et al.* [2008], *Qin and Shen* [2017], *Moloto et al.* [2018], *Engelbrecht et al.* [2019], and *Moloto and Engelbrecht* [2020] in numerical CR modulation studies. The approach followed here is similar to that taken by *Burger et al.* [2008], where the total variance is modelled as

$$\delta B_T^2(r,t) = \delta B_T^2(r_e,t)\left(\frac{r}{r_e}\right)^{-2.4} \tag{5.4}$$

with $\delta B_T^2(r_e,t)$ the total magnetic variance at Earth ($r = r_e = 1$ AU) as function of time t, as input from the observations discussed in the previous chapter. Slab and 2D variances are extracted from the above expression according to the 20/80 ratio for these quantities, following the result of *Bieber et al.* [1994]. The 2D correlation scale is modelled similarly, so

that

$$\lambda_{2D}(r,t) = \lambda_{2D}(r_e,t)\left(\frac{r}{r_e}\right)^{0.5}, \tag{5.5}$$

using values for $\lambda_{2D}(r_e,t)$ modelled as discussed in the previous section. The slab correlation scale is modelled as $\lambda_{sl}(r,t) = 2.55\lambda_{2D}(r,t)$, following the observations at Earth reported by *Weygand et al.* [2011]. The above expressions will be used to extrapolate 1 AU values of these turbulence quantities out to 100 AU. Beyond this distance, these fits would no longer be applicable, due to the changing nature of turbulence in the heliosheath [see, e.g., *Burlaga et al.*, 2018]. Note that, as a first approach, no latitudinal dependence is assumed in the extrapolations of turbulence quantities considered here.

5.5 Resulting Transport Coefficients

Diffusion and drift lengthscales as a function of rigidity (at 1AU) are shown in the top panel of Figure 5.4 for heliospheric and turbulence quantities during 1964. The *Palmer* [1982] consensus range values as shown by Figure 5.1 in Section 5.2 are shown here again to assist in comparing the computed result to those of [*Burger et al.*, 2008]. The parallel and perpendicular MFPs display the same rigidity dependences as shown there. The drift scale is essentially equal to the weak scattering value (R_L) at large rigidities, where it displays a P^1 dependence. At lower rigidities it declines from this scaling due to the influence of turbulence.

The two lower panels of Figure 5.4 display the yearly computed results for MFPs and drift scales of galactic CR protons between 1964 and 1990. These results were computed for an energy of 5 GeV corresponding to a rigidity of ~ 5.87 GV, which is larger than the vertical cutoff rigidity of the Hermanus NM experiment. This was done so that transport coefficients represented in the figure would give insight as to the coefficients of high energy CRs indirectly detected by this NM. The parallel MFP shows a clear variation with solar cycle and has comparatively larger values during solar minimum. This does not agree with the results of *Zhao et al.* [2018] who consider the time dependence of a similar quasilinear theory expression proposed by *Zank et al.* [1998]. The discrepancy between the results of that study and those in Figure 5.4 may be due to the consideration of a much lower rigidity of 445 MV by *Zhao et al.* [2018], because the first term on the right hand side of Eq. 5.1 has a greater effect on how the resulting expression behaves when higher rigidities are considered. Figure 5.4 also shows perpendicular MFPs and drift scales at Earth as function of time. At 5 GeV a clear solar cycle dependence is seen for $\lambda_\perp$ with results being larger during solar maximum. The *Zank et al.* [2004] perpendicular MFP used by *Zhao et al.* [2018] is similar to the one presented here, but *Zhao et al.* [2018] do not report on a significant variation in $\lambda_\perp$ with solar cycle, possibly due to their consideration of a lower rigidity (which would influence $\lambda_\parallel$) or due to the fact that the 2D correlation scale is assumed to display solar cycle dependent behaviour in this study. For all rigidities shown, the weak-scattering and turbulence-reduced drift scales (which are not included in Figure 5.4) are almost identical, and change with solar cycle. At periods of elevated solar activity these drift scales have smaller values, and they show relatively uniform behaviour during the 1960s when the HMF was relatively constant (see Figure 2.9). The perpendicular MFP is larger than the drift scale during solar maxima, which is consistent with expectations of diffusion-dominated CR transport as function of solar cycle [see, e.g., *Moloto and Engelbrecht*, 2020]. Finally, the CR transport coefficients produced here display temporal profiles that are qualitatively similar during the late 1960s and late 1980s.

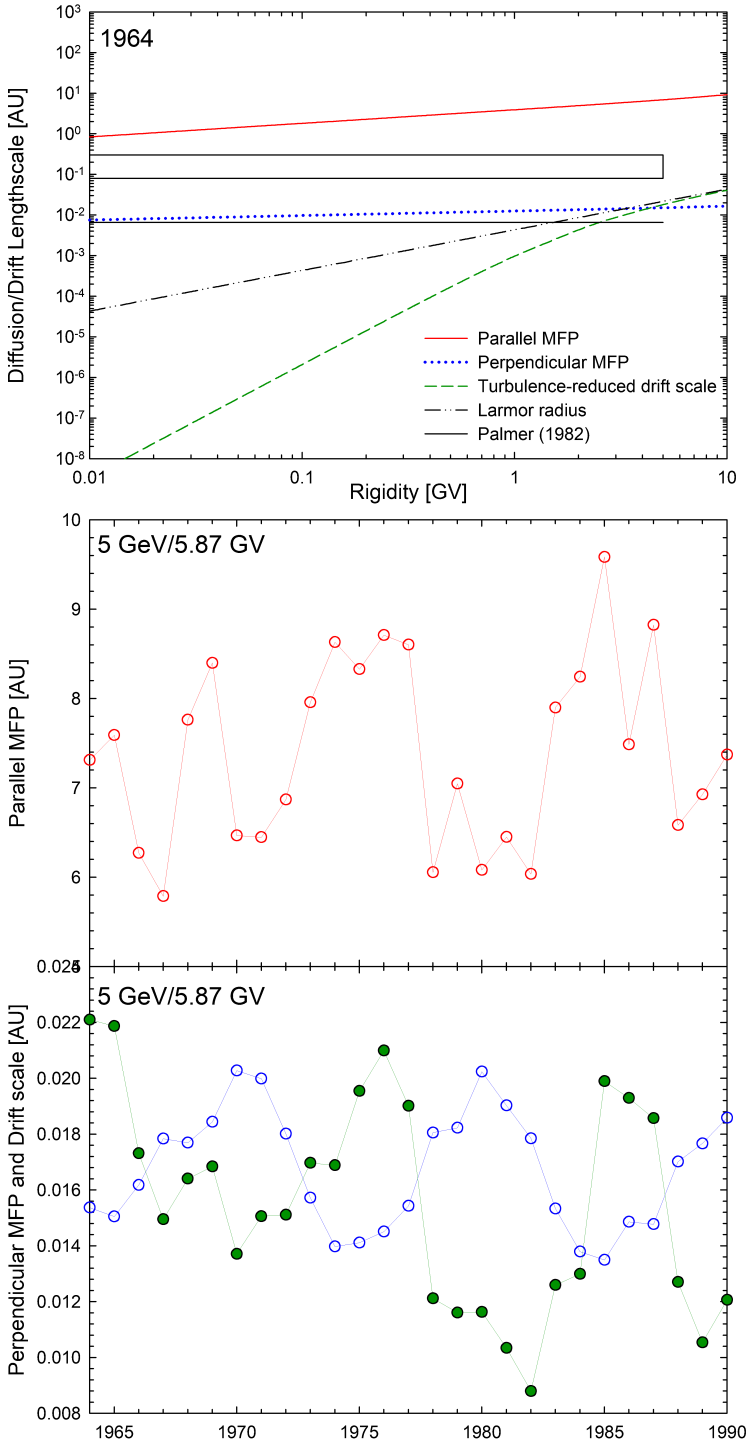

FIGURE 5.4: Diffusion and drift lengthscales used here as functions of rigidity at Earth for 1964 parameters (top panel). The *Palmer* [1982] consensus range values are again shown here to aid visual comparison. The galactic CR proton parallel MFPs at Earth as function of time at an energy of 5 GeV are shown in the middle panel. In the bottom panel, Perpendicular MFPs (blue) and turbulence-reduced drift scale (green) at Earth as function of time are shown, at 5 GeV. Figure taken from *Engelbrecht and Wolmarans* [2020].

Figure 5.5 serves to emphasize and illustrate differences in MFPs and drift scales by displaying the ratios of their computed values for years that correspond to their relative order in the rise in solar activity starting with 1964/1985 at solar minimum conditions and ending near solar maximum in 1969/1990. Due to the winding of the Parker field beyond 10 AU only the perpendicular MFP is discussed here, along with the drift scale, as the almost-azimuthal geometry of the Parker HMF beyond this distance implies that the transport of CRs would be dominated by these coefficients [see, e.g., *Engelbrecht and Burger*, 2015b; *Caballero-Lopez et al.*, 2019]. The perpendicular MFP ratios (top panels) and drift scale ratios (bottom panels) are shown in 5.5 as function of rigidity for two heliocentric distances, one at Earth (1AU, left panels) and the other at 100 AU (right panels). Here the behaviour of the ratios of perpendicular MFPs in the 1960s and their partners in the 1980s is shown in the top panels of Figure 5.5. At both distances these figures show that the perpendicular MFP ratios remain quite similar, with an eventual increase at the largest rigidities. This increase occurs at a lower rigidity for 100 AU, relative to that 1 AU. The ratios of drift scales are altered by turbulence at low rigidity. Therefore, the behavior of the ratios of drift scales is that of larger differences at low rigidities and smaller differences at high rigidities, becoming relatively flat beyond rigidities of 0.1 GV at 1 AU and 0.01 GV at 100 AU. The largest percentage differences in perpendicular MFPs at 1 AU is seen for the 1964/1985 result (below 16%). For results of the perpendicular MFPs computed at 100 AU the largest percentage difference (below 23%) is again seen when the 1964/1985 pair are compared. For the drift scale at both heliocentric distances, the greatest difference is seen for the last ratio pair (1969/1990), which is around 33%.

5.6 Qualitative Effects on the Modulation of Galactic CR Protons

In the previous section, transport coefficients were calculated for conditions prevalent in the 1960s and 1980s. This was done to compare them for a period displaying a relatively unusual relationship between observed CR intensities and HMF magnitudes with one in which this relationship is generally considered to have behaved in a more usual, roughly inverse, fashion. From the results presented thus far, the perpendicular MFPs during the late 1960s and those of the late 1980s were quite comparable. When considering drift scales at the higher rigidities for particles that would be detected by NM experiments, larger differences in the range of ~ 30%) were seen. The aim in this section is to determine if these differences could be used to shed some light as to the the unusual relationship observed between CR intensities and HMF magnitudes, during the latter part of the 1960s.

In order to achieve this the equation governing the transport of CRs of *Parker* [1965] must be solved with the inputs from the study presented in this Chapter. The Parker transport equation is given by

$$\frac{\partial f}{\partial t} = \nabla \cdot \left(\mathbf{K} \cdot \nabla f \right) - \mathbf{V}_{SW} \cdot \nabla f + \frac{1}{3} \left(\nabla \cdot \mathbf{V}_{SW} \right) \frac{\partial f}{\partial \ln p} + Q(\mathbf{r}, p, t), \tag{5.6}$$

which solves for the the omnidirectional CR distribution function $f(\mathbf{r}, p, t) = p^{-2} j_T$, which is a function of position $\mathbf{r}$, momentum p and time t [see, e.g., *Moraal*, 2013]. This relates to the CR differential intensity j_T of spaceceraft observations, instead of CR intensities as observed by NMs, but still allows for the qualitative comparison of the results measured using these different instruments [see, e.g., *Clem and Dorman*, 2000]. The terms on the right side of Eq. 5.6 describe the processes that affect CR modulation. The term $1/3 \left(\nabla \cdot \mathbf{V}_{SW} \right) \partial f / \partial \ln p$ describes the adiabatic energy changes that CRs may encounter within the heliosphere.

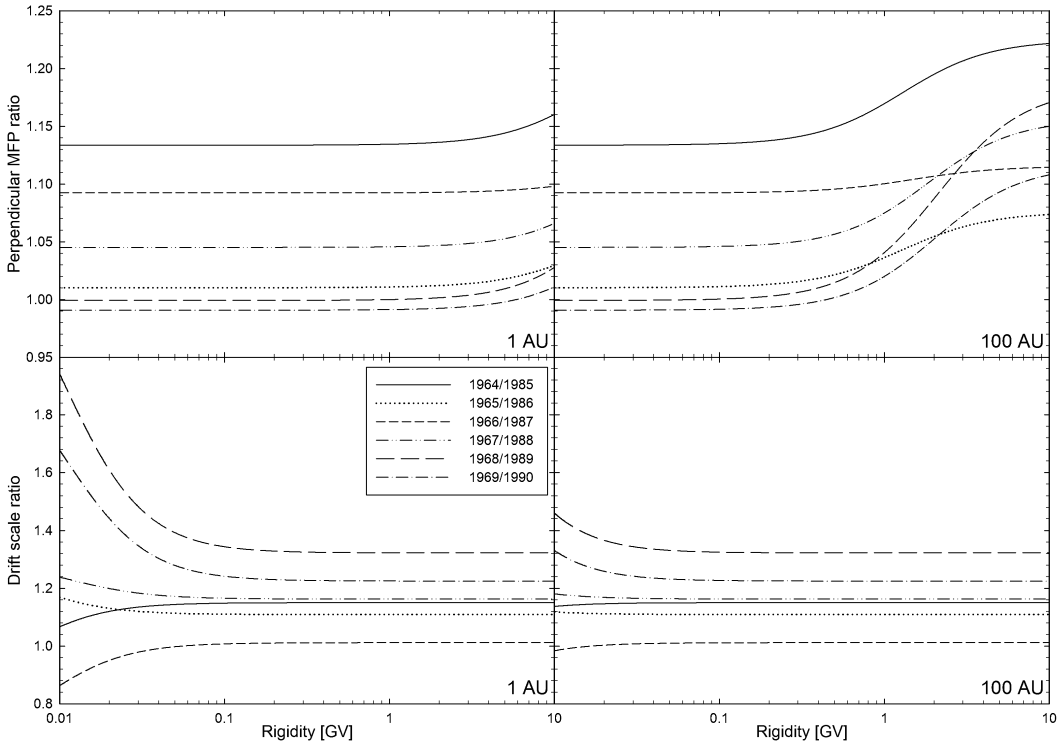

FIGURE 5.5: Perpendicular MFP (from Eq. 5.2, top panels) and drift scales (see Eq. 5.3 and R_L in Section 5.2, bottom panels) ratios at 1 (left panels) and 100 AU (right panels) as function of rigidity during the 1960s and 1980s, using turbulence quantities calculated from *OMNI* data used in this study. Figure taken from *Engelbrecht and Wolmarans* [2020]. See the in text discussion for more detail.

The SW, propagating at a velocity $\mathbf{V}_{SW}$, causes the outward convection of CRs, which is described by $\mathbf{V}_{SW} \cdot \nabla f$. CR diffusion, gradient and curvature drift of CRs due to the geometry of the HMF and the heliospheric current sheet [see, e.g., *Jokipii and Thomas*, 1981; *Kota and Jokipii*, 1983; *Burger et al.*, 2008; *Engelbrecht et al.*, 2019] are contained in $\nabla \cdot (\mathbf{K} \cdot \nabla f)$, where $\mathbf{K}$ is the CR diffusion tensor, which can be written in HMF-aligned coordinates in terms of parallel and perpendicular diffusion coeffients $\kappa_{\parallel}$ and $\kappa_{\perp}$ as well as drift coefficients κ_A as [e.g. *Burger et al.*, 2008]

$$\mathbf{K}' = \begin{bmatrix} \kappa_{\parallel} & 0 & 0 \\ 0 & \kappa_{\perp,2} & \kappa_A \\ 0 & -\kappa_A & \kappa_{\perp,3} \end{bmatrix} \tag{5.7}$$

The final term on the right side of Eq. 5.6, Q is provided in order to account for the presence of any sources and sinks for CRs in the heliosphere. When considering galactic CRs Q is taken to be zero, as will be done in this study.

The goal here is to solve Eq. 5.6 using a modified steady-state, stochastic CR modulation code from *Engelbrecht and Burger* [2015b], so as to incorporate the diffusion and drift lengthscales in Section 5.2 relevant to the 1960s and 1980s, similar to the approach of *Moloto et al.* [2018] and *Moloto et al.* [2019]. The interested reader is referred to *Yamada et al.* [1998]; *Zhang* [1999]; *Pei et al.* [2010]; *Strauss et al.* [2011]; *Bobik et al.* [2012]; *Dunzlaff et al.* [2015]; *Wawrzynczak et al.* [2015]; *Strauss and Effenberger* [2017] for a more complete discussion of stochastic solutions to the the Parker transport equation, which is beyond the scope of this work. The goal for this investigation is to compute CR intensities at sufficiently

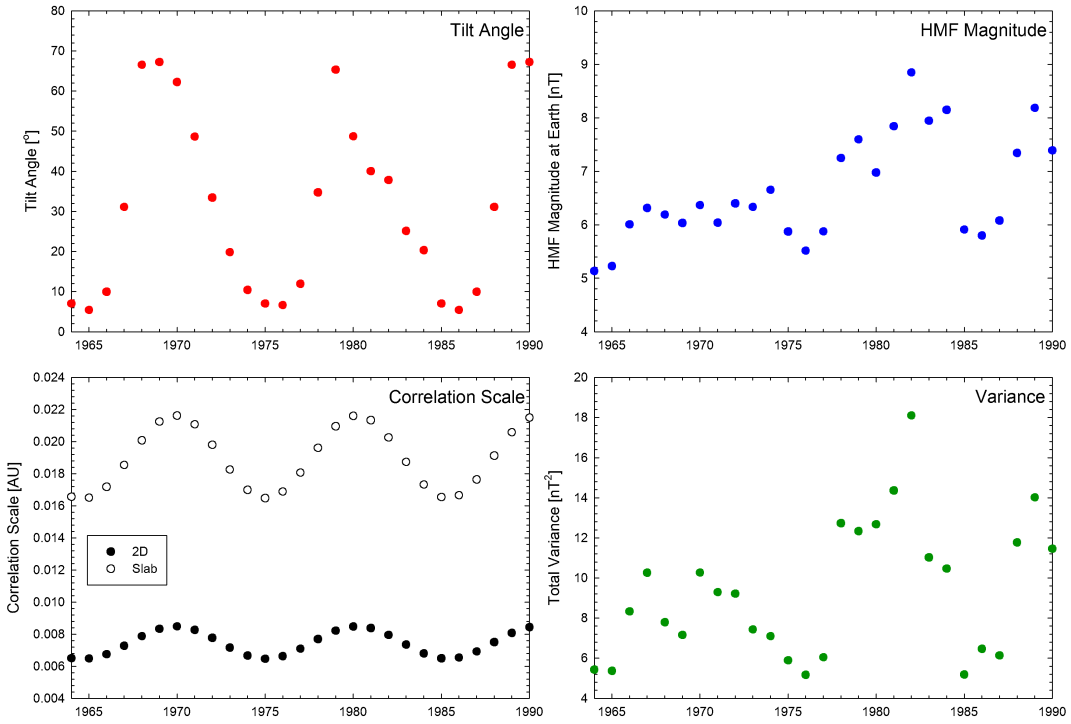

FIGURE 5.6: Heliospheric and turbulence quantities relevant to CR modulation with time. Top left: yearly averages of solar tilt angles, values beyond 1976 are calculated from Wilcox Solar Observatory radial model tilt angles [*Hoeksema*, 1992] (available at `http://wso.stanford.edu`), while angles of the 1960s are chosen to be the same as those corresponding to their partners in relation to solar activity as shown in Figure 5.5, in the 1980s. Tilt angles for the 1970s are interpolated using Eq. 5.9. Top right panel: Yearly-averaged *OMNI* HMF magnitudes at Earth. Bottom left panel: Slab and 2D correlation scales at Earth, calculated as described in Section 5.3. Bottom right panel: yearly averaged total magnetic variances calculated in this study.

high rigidities, so that they may be compared with NM observations. This would give insight as to the conditions of CR transport, relative to the anomalous HMF behaviour of the 1960s. In this study, no attempt is made to fit data, only to see whether use of the results of this study could reproduce the expected CR intensity behaviour as seen in NM data, when magnetic turbulence is taken into account.

The turbulence quantities, diffusion and drift coefficients used here are modelled exactly as described in prior Sections 5.4 and 5.2. With the uncertainty in the large-scale heliospheric quantities in the early periods of spacecraft observation, such as during the 1960s, with the heliospheric tilt angle as an example, their inputs will be modelled to be as simple as possible. Here, following the approach of *Caballero-Lopez et al.* [2004a], the assumptions of a Parker HMF and a solar-cycle average SW speed of 600 km/s are made. Heliosperic tilt angles are taken from the Wilcox Solar Observatory website (`http://wso.stanford.edu`), where after 1976 the yearly averaged values of observed tilt angles are computed using the radial model *Hoeksema* [see 1992]. Since tilt angle observations do not extend as far back as the late 1960s they are assumed to be the same as those during the late 1980s. Due to the lack of tilt angle observations in the former part of the 1970s a model of a fit to tilt angle observations with solar cycle proposed by *Burger et al.* [2008], modified to take into account

the upper limit of 75° in Wilcox observations, is employed here. This is done since the tilt angle expression of *Burger et al.* [2008] allows for a maximum tilt angle of 90° not seen in Wilcox tilt angle data. The tilt angle expression used to obtain the tilt angles necessary for the purposes of this study during the 1970s, is then [*Engelbrecht and Wolmarans*, 2020]

$$\begin{aligned} \alpha(T) &= \alpha_{min} + \left(\frac{\pi}{4.8} - \frac{\alpha_{min}}{2}\right) \\ &\times \begin{cases} 1 - cos\left(\frac{\pi}{4}T\right), 0 \leq T \leq 4 \\ 1 - cos\left(\frac{\pi}{7}(T-11)\right), 4 < T \leq 11 \end{cases} \end{aligned} \tag{5.8}$$

All of the angles input to this equation are in radians and T is simply the number of years after solar minimum. By this model and the tilt angle observations used, a record of tilt angles is constructed where the $\alpha_{min} = 7°$ and 75° are the values during full solar minimum and solar maximum, respectively.

The angular extent of the heliospheric current sheet is modelled using [see, e.g., *Kota and Jokipii*, 1983; *Burger et al.*, 2008; *Raath et al.*, 2015]

$$\theta = \frac{\pi}{2} - \tan^{-1}\left[\tan\alpha \sin\left(\phi_o + \frac{\Omega r}{V_{SW}}\right)\right], \tag{5.9}$$

with the term ϕ_o an angle that allows for the modification of the heliospheric current sheet orientation in the fixed observer frame (assumed to be 0° here), and Ω the solar rotation rate. Observations reported by *Slavin and Smith* [1983] for 1979 and 1980 are accounted for in this study to model the necessary changes in magnetic polarities here. The approach proposed by *Burger* [2012] was used to model the required drift velocities resulting from current sheet drift as well as drifts due to gradients and curvatures of the assumed Parker field. The final record of tilt angles produced, in order to gain insight as to the behaviour of CR intensities in the 1960s, is shown as a function of time in the top left panel of Figure 5.6. These tilt angles clearly display the solar cycle dependence expected for tilt angle observations, in line with the discussion of Figure 2.7 in Chapter 2. This figure also shows, for convenience, the other inputs used in the CR modulation model, which include the HMF magnitude (top right panel) as well as the magnetic correlation lengths and variances (bottom panels) discussed in previous sections.

The boundary spectrum model used in this study is defined to be near the termination shock (85 AU), based on the galactic CR proton observations of *Webber et al.* [2008]. This is required because it is known that a large amount of CR modulation occurs in the heliosheath [e.g. *Stone et al.*, 2013], which cannot be taken into account in this study because the implied assumption of dominant transverse turbulence made here due to the use of diffusion coefficients obtained from such assumptions is not valid in the region beyond the termination shock [see, e.g., *Burlaga et al.*, 2018]. Various studies of CR modulation use a similar approach to the boundary spectrum, as will be used here [see, e.g., *Engelbrecht and Burger*, 2015b; *Qin and Shen*, 2017; *Moloto et al.*, 2018; *Shen and Qin*, 2018; *Moloto and Engelbrecht*, 2020]. *Moloto et al.* [2018] proposed the input spectrum that will be applied here. This spectrum is given by

$$j_B(85\text{ AU}) = \frac{17.0(P/P_o)^{-2.4}}{2.2 + 2.1(P/P_o)^{-3}}, \tag{5.10}$$

which is in units of particles.m^{-2}.s^{-1}.sr^{-1}.MeV^{-1}. The rigidities P and $P_o = 1$ GV are in units of GV. In the boundary spectrum presented here, changes relating to solar cycle [see, e.g., *Webber et al.*, 2008] are not taken into account. This is done so that such changes do

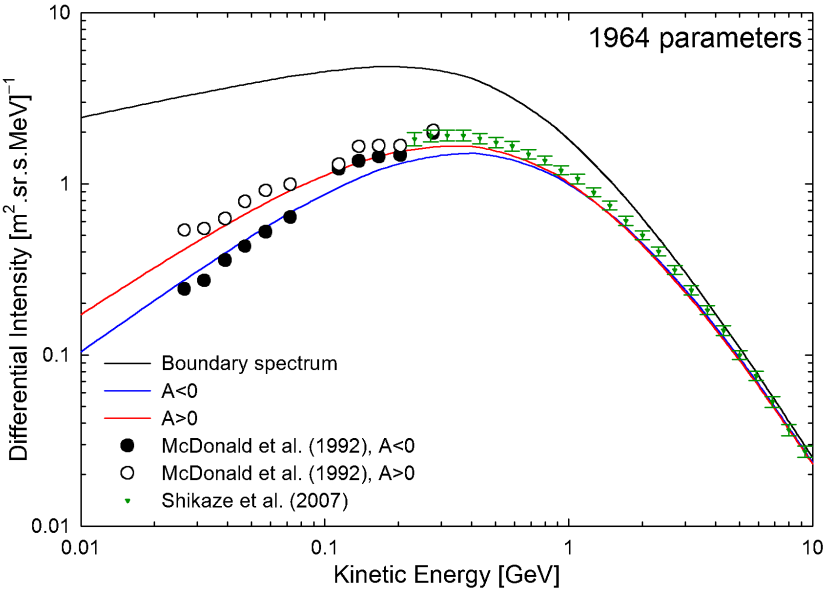

FIGURE 5.7: Galactic CR proton intensities as function of kinetic energy, computed in this study using heliospheric and turbulence parameters for 1964 for positive and negative magnetic polarities. The proton differential intensities observed at Earth reported for different periods of time by *McDonald et al.* [1992] ($A > 0$, 1977/1978 and $A < 0$ for 1987) and *Shikaze et al.* [2007] (for different solar activity periods between 1997 and 2002) are also shown. The boundary spectrum assumed in the modulation code at 85 AU (Eq. 5.10) is indicated by the black line. This figure is taken from *Engelbrecht and Wolmarans* [2020].

not bias the conclusions of this study. Solar cycle dependent changes in the termination shock location [see, e.g., *Washimi et al.*, 2017] are also not taken into account in this study.

The CR modulation code described here is run consecutively on a year-to-year basis, starting from 1964 up to and including 1990, using the yearly averaged heliospheric plasma quantities of Figure 5.6 as inputs. Uncertainties in heliospheric parameters, during the latter part of the 1960s and the first half of the 1970s, will not allow for smaller time resolutions to be used here. Fortunately, [*Strauss et al.*, 2011] have shown that galactic CRs remain in the heliosphere for extended periods (residence times of approximately one year), which may allow for a reasonable estimation to be made of the long term behaviour of CR intensities from the effective value approach presented here [see, e.g., *Moloto et al.*, 2018, and references therein]. Using the parameters for 1964 in this model, Figure 5.7 shows the calculated differential intensity spectra of galactic CR protons at 1AU as a function of the kinetic energy for both HMF polarity conditions, with the boundary spectrum (Eq. 5.10) used to compute them. The observations of *McDonald et al.* [1992] and *Shikaze et al.* [2007] are included for comparison. It is seen that the proton intensities from this study for the conditions prevailing in 1964 do not behave very differently to the spectra of *McDonald et al.* [1992] (taken during 1987 and 1977/1978) for the appropriate magnetic polarity. The 1964 spectrum calculated here is in fact quite similar tot the negative polarity solar minimum of 1987, which qualitatively agrees with the comparison of the 1960s and 1980s observations made by *McDonald et al.* [1992]. This also agrees with the observations of NMs, that display similar behaviour during the 1960s and the latter part of the 1980s.

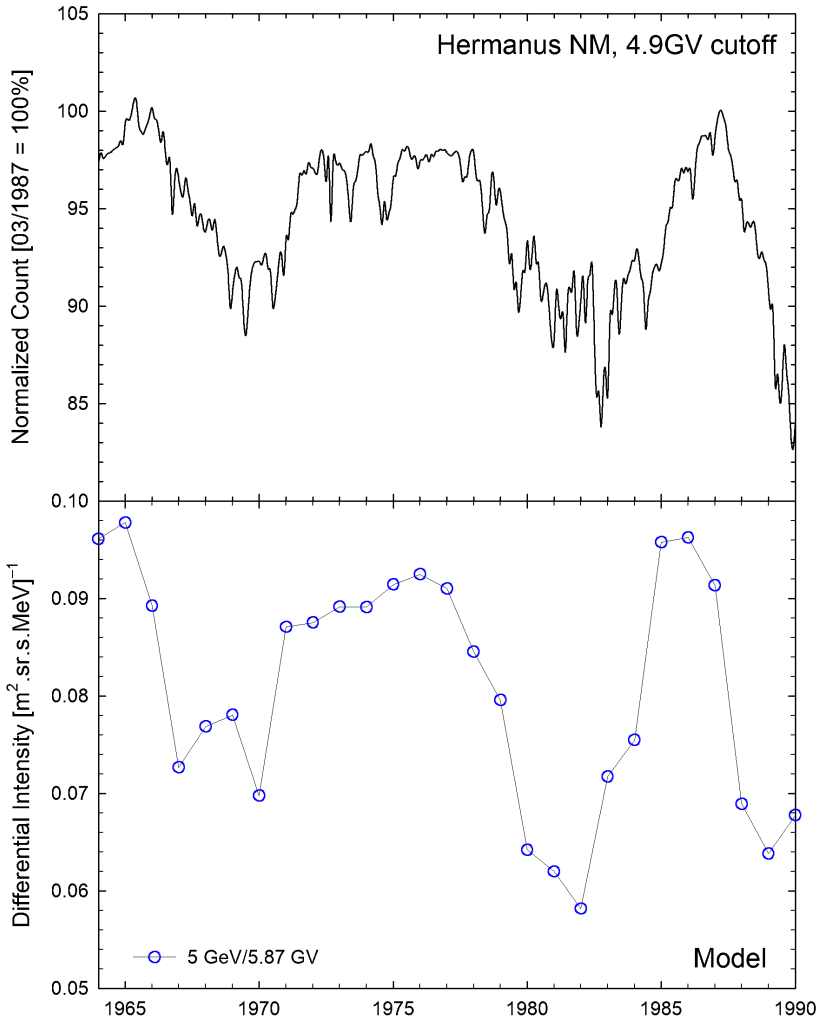

FIGURE 5.8: Hermanus NM count rates (vertical cutoff rigidity: 4.9 GV) between 1964 and 1990 are shown in the top panel (`http://natural-sciences.nwu.ac.za/neutron-monitor-data`). The bottom panel shows the galactic CR proton differential intensities at 5 GeV calculated by the model presented over the same span of time. The figure was taken from *Engelbrecht and Wolmarans* [2020].

Hermanus NM count rates and 5 GeV intensities computed using the modulation code are compared in the top and bottom panels of Figure 5.8. The selected energy value (5 GeV) corresponds to the rigidity of 5.87 GV which is larger than, but close enough as to be comparable to the cutoff rigidity of the NM experiment. The application of the model code presented in this study reveals a distinct solar cycle dependence in the computed intensities along with the expected peak and plateau time profiles expected of charge-sign dependent CR modulation in periods of different solar magnetic polarity [see, e.g., *Potgieter and Le Roux*, 1994]. The galactic proton differential intensity time profiles produced using this model are therefore in qualitative agreement with NM counts, apart from a bump in intensities around 1968/1969. Specifically, the time profile of the computed intensities during the late 1960s is similar to that computed for conditions corresponding to the late 1980s.

5.7 Summary

The effects on diffusion and drift coefficient expressions of galactic CR protons of the turbulence and large-scale plasma quantities obtained observationally during the 1960s and 1980s were investigated here. The differences in these quantities during the 1960s and 1980s were relatively small, and for diffusion coefficients in particular this was due to the dependence that these expressions have on the ratios of the magnetic variance and HMF magnitude, which were similar during these two periods.

Using observational values, or appropriate extrapolations for such values from observations, as yearly inputs for large and small scale heliospheric plasma quantities, the effect of varying such quantities on the modulation of galactic protons was investigated by use of a stochastic solver for the *Parker* [1965] transport equation. The computed intensities during the early 1960s and the proton differential intensity spectra observed in 1987 were very similar, which qualitatively agrees with results reported by *McDonald et al.* [1992]. Clear solar cycle and 22-year cycle dependences were seen in computed intensities at 5 GeV as function of time, displaying the characteristic solar minima profiles familiar in charge-sign dependent modulation and in qualitative agreement with observations made by NMs. For the latter parts of the two negative HMF polarity solar minima during the late 1960s and 1980s, the temporal intensity profiles were seen to be very similar. These results imply that the current model is capable of qualitatively reproducing the behaviour of CR intensities with time, even when the HMF magnitude observed at Earth was almost constant during the late 1960s. This reproduction of the behaviour of observed CR intensity by neutron monitors would not have resulted here if only the measurements of the HMF magnitude, without the influence of turbulence quantities on computed transport coefficients, were taken into account.

Even when considering that the HMF magnitude remained relatively low during the 1960s, the magnetic variances behaved similarly and thus the relevant transport parameters of galactic CRs during this early period were not seen to be very different to their counterparts during the 80s. As a consequence, the atypical relationship between CR intensities and HMF magnitudes during the late 1960s was not as anomalous as previously thought [see, e.g., *Wibberenz et al.*, 2002; *Agarwal and Mishra*, 2008].

Chapter 6

Summary and Conclusions

This study presents an inquiry as to the cosmic-ray modulation conditions during the latter half of the 1960s, a period in which the relationship between cosmic-ray intensities and heliospheric magnetic field observations is generally considered to have been anomalous. Various explanations have been given as to the cause of this behaviour detailed in the literature, none of which approach this period from the perspective of solar wind turbulence and its influence on cosmic-ray transport.

In order to investigate whether the influence of turbulence may be responsible for the departure from the otherwise anti-correlated relationship between intensities and the heliospheric magnetic field magnitude, *in situ* observations of the SW during this period needed to be analysed. However, measurements from the early space-age are characterized by frequent omissions in data and low resolutions relative to modern observations. These limitations hamper the analysis by higher-order techniques commonly applied in such studies. In order to glean some information as to the behaviour relevant to the transport of cosmic rays, lower-order analysis techniques were identified, and tested using synthetic turbulence data. It was concluded that the standard definition of the correlation function, as well as the construction of partial variances as a measure of the integrated power spectrum, would be most suited for analysis of early space-age spacecraft data.

These techniques were then applied to *OMNI* and *Pioneer 6* and *7* observations, taken during the late 1960s as well as during the latter half of the 1980s. A comparison of turbulence quantities in the 1980s was made due to the fact that the cosmic-ray/magnetic field relationship during this time was more typical than during the 1960s, and that both periods are of negative heliospheric magnetic field polarity. During the 1960s, it was found that magnetic variances behaved similarly to the magnetic field observations that remained quite low towards the approach of solar maximum. The same was seen to be true during the 1980s when a clear enhancement of the magnetic variances and the field magnitudes was observed along with increased solar activity. As a result the ratios between magnetic variance and the heliospheric magnetic field during both periods were not only relatively constant, but also quite similar.

A closer look at *Pioneer 6* and *7* observations during the period when both these spacecraft were operational revealed three intervals of greatly enhanced magnetic variance. Two of these periods correspond to known solar events described by *Bukata et al.* [1969] and *Knipp et al.* [2016]. The third interval cannot be connected to a known event in the literature, which raises the possibility that it corresponds to a previously unknown solar event.

To test whether the behaviour of the turbulence quantities obtained in this study would have an effect on cosmic-ray transport, these quantities were used as inputs for expressions describing the parallel and perpendicular diffusion coefficients of galactic cosmic-ray protons, as well as their turbulence-reduced drift coefficients. The coefficients used were selected on the basis that they have previously been used in cosmic-ray modulation studies, resulting in galactic cosmic-ray proton intensities in reasonable agreement with observations. It was found that differences in diffusion and drift coefficients during the 1960s and 1980s were not large, due to the relatively constant behaviour of the ratio of the magnetic variance to heliospheric magnetic field magnitude observed during these periods. These coefficients were then used as inputs for a 3D stochastic cosmic-ray modulation code, so that galactic cosmic-ray proton intensities could be calculated on a yearly basis, using observational and extrapolated effective values for the various plasma quantities that influence cosmic-ray transport. These results were compared with neutron monitor observations over several solar cycles, including the period in the late 1960s, and were found to be in qualitative agreement with these observations. Computed results displayed clear 11 and 22 year cyclic behaviour. This leads to the conclusion that the atypical relationship between observed cosmic-ray intensities and the heliospheric magnetic field magnitude does not necessarily imply that modulation conditions during the 1960s were anomalous, even though the heliospheric magnetic field magnitude behaved differently in that period. Taking into account turbulence conditions during that time leads to what could be considered to be 'typical' cosmic-ray modulation. This final result highlights the importance of taking into account the analysis of turbulence in studies of cosmic-ray transport as well as studies of the correlations between various heliospheric parameters and cosmic-ray intensities.

Acknowledgments

I would like to express my deepest gratitude toward Professor Nicholas Eugene Engelbrecht for his expert guidance, support and motivation, all of which was instrumental to the completion of this work. I give thanks to all members of the Center for Space Research and the Physics department at the Potchefstroom campus of the NWU, as well as associated support staff for the opportunity, outstanding quality of education and support they ceaselessly provide. Finally, I thank those closest to me as family and friends for their support and patience during the period in which this work was completed.

The financial assistance of the National Research Foundation (NRF) towards this research is hereby acknowledged. Opinions expressed and conclusions arrived at, are those of the author and are not necessarily to be attributed to the NRF.

Bibliography

Adhikari, L., G. P. Zank, P. Hunana, D. Shiota, R. Bruno, Q. Hu, and D. Telloni, 2017, II. transport of nearly incompressible magnetohydrodynamic turbulence from 1 to 75 au, *Astrophys. J.*, *841*(2): 85, doi:10.3847/1538-4357/aa6f5d.

Agarwal, R., and R. K. Mishra, 2008, Solar cycle phenomena in cosmic ray intensity up to the recent solar cycle, *Phys. Lett. B*, *664*(1-2): 31–34, doi:10.1016/j.physletb.2008.04.057.

Ahluwalia, H. S., 2000, On galactic cosmic ray flux decrease near solar minima and imf intensity, *Geophys. Res. Lett.*, *27*(11): 1603–1606, doi:10.1029/2000GL003759.

Akasofu, S.-I., P. D. Perreault, and S. Yoshida, 1969, The geomagnetic and cosmic-ray storm of May 25/26, 1967, *Solar Phys.*, *8*(2): 464–476.

Balogh, A., and V. Izmodenov, 2005, The heliosphere and its boundaries, *The solar system and beyond: ten years of ISSI*, *3*: 1151.

Batchelor, G. K., 1953, *The Theory of Homogeneous Turbulence*, Cambridge university press.

Bieber, J. W., and W. H. Matthaeus, 1997, Perpendicular diffusion and drift at intermediate cosmic-ray energies, *Astrophys. J.*, *485*(2): 655–659, doi:10.1086/304464.

Bieber, J. W., W. H. Matthaeus, C. W. Smith, W. Wanner, M.-B. Kallenrode, and G. Wibberenz, 1994, Proton and Electron Mean Free Paths: The Palmer Consensus Revisited, *Astrophys. J.*, *420*: 294–306, doi:10.1086/173559.

Bieber, J. W., W. Wanner, and W. H. Matthaeus, 1996, Dominant two-dimensional solar wind turbulence with implications for cosmic ray transport, *J. Geophys. Res.*, *101*(A2): 2511–2522, doi:10.1029/95JA02588.

Bieber, J. W., W. H. Matthaeus, A. Shalchi, and G. Qin, 2004, Nonlinear guiding center theory of perpendicular diffusion: General properties and comparison with observation, *Geophys. Res. Lett.*, *31*(10), L10805, doi:10.1029/2004GL020007.

Blackman, R. B., and J. W. Tukey, 1958, The Measurement of Power Spectra from the Point of View of Communications Engineering — Part I, *Bell System Technical Journal*, *37*(2): 485–569, doi:10.1002/j.1538-7305.1958.tb01530.x.

Bobik, P., et al., 2012, Systematic Investigation of Solar Modulation of Galactic Protons for Solar Cycle 23 Using a Monte Carlo Approach with Particle Drift Effects and Latitudinal Dependence, *Astrophys. J.*, *745*(2), 132, doi:10.1088/0004-637X/745/2/132.

Boschini, M. J., et al., 2017, Solution of Heliospheric Propagation: Unveiling the Local Interstellar Spectra of Cosmic-ray Species, *Astrophys. J.*, *840*(2), 115, doi:10.3847/1538-4357/aa6e4f.

Breech, B., W. H. Matthaeus, J. Minnie, J. W. Bieber, S. Oughton, C. W. Smith, and P. A. Isenberg, 2008, Turbulence transport throughout the heliosphere, *J. Geophys. Res. (Space Physics).*, *113*(A8), A08105, doi:10.1029/2007JA012711.

Bruno, R., and V. Carbone, 2013, The Solar Wind as a Turbulence Laboratory, *Living Rev. Solar Phys.*, *10*(1), 2, doi:10.12942/lrsp-2013-2.

Bukata, R. P., P. T. Gronstal, R. A. R. Palmeira, K. G. McCracken, and U. R. Rao, 1969, Neutron Monitor and Pioneer 6 and 7 Studies of the January 28, 1967 Solar Flare Event, *Solar Phys.*, *10*(1): 198–211, doi:10.1007/BF00146170.

Burger, R. A., 2012, Modeling Drift along the Heliospheric Wavy Neutral Sheet, *Astrophys. J.*, *760*(1), 60, doi:10.1088/0004-637X/760/1/60.

Burger, R. A., and N. E. Engelbrecht, 2018, Solar-Cycle Dependence of the Correlation Length for the N-Component of the Magnetic Field From IMP and ACE Observations From 1973 to 2016, in *AGU Fall Meeting Abstracts*, vol. 2018, pp. SH21C–3300.

Burger, R. A., and D. J. Visser, 2010, Reduction of Drift Effects due to Solar Wind Turbulence, *Astrophys. J.*, *725*(1): 1366–1372, doi:10.1088/0004-637X/725/1/1366.

Burger, R. A., M. S. Potgieter, and B. Heber, 2000, Rigidity dependence of cosmic ray proton latitudinal gradients measured by the Ulysses spacecraft: Implications for the diffusion tensor, *J. Geophys. Res.*, *105*(A12): 27,447–27,456, doi:10.1029/2000JA000153.

Burger, R. A., T. P. J. Krüger, M. Hitge, and N. E. Engelbrecht, 2008, A Fisk-Parker Hybrid Heliospheric Magnetic Field with a Solar-Cycle Dependence, *Astrophys. J.*, *674*(1): 511–519, doi:10.1086/525039.

Burlaga, L. F., V. Florinski, and N. F. Ness, 2018, Turbulence in the Outer Heliosheath, *Astrophys. J.*, *854*(1), 20, doi:10.3847/1538-4357/aaa45a.

Caballero-Lopez, R. A., H. Moraal, K. G. McCracken, and F. B. McDonald, 2004a, The heliospheric magnetic field from 850 to 2000 AD inferred from ^{10}Be records, *J. Geophys. Res. (Space Physics).*, *109*(A12), A12102, doi:10.1029/2004JA010633.

Caballero-Lopez, R. A., H. Moraal, and F. B. McDonald, 2004b, Galactic cosmic ray modulation: Effects of the solar wind termination shock and the heliosheath, *J. Geophys. Res. (Space Physics).*, *109*(A5), A05105, doi:10.1029/2003JA010358.

Caballero-Lopez, R. A., N. E. Engelbrecht, and J. D. Richardson, 2019, Correlation of Long-term Cosmic-Ray Modulation with Solar Activity Parameters, *Astrophys. J.*, *883*(1), 73, doi:10.3847/1538-4357/ab3c57.

Clem, J. M., and L. I. Dorman, 2000, Neutron Monitor Response Functions, *Space Sci. Rev.*, *93*: 335–359, doi:10.1023/A:1026508915269.

Corliss, W. R., 1972, *The interplanetary pioneers. Volume 1: Summary*, NASA, United States.

Cuoco, A., 2020, Signatures of dark matter in cosmic-ray observations, in *J. Phys.: Conf. Ser.*, vol. 1468, p. 012095, doi:10.1088/1742-6596/1468/1/012095.

Davidson, P., 2015, *Turbulence: An Introduction for Scientists and Engineers*, 2nd ed., Oxford Univeristy Press, doi:10.1093/acprof:oso/9780198722588.001.0001.

Decker, R. B., 1993, The role of magnetic loops in particle acceleration at nearly perpendicular shocks, *J. Geophys. Res.*, *98*(A1): 33–46, doi:10.1029/92JA01841.

Decker, R. B., and L. Vlahos, 1986, Numerical Studies of Particle Acceleration at Turbulent, Oblique Shocks with an Application to Prompt Ion Acceleration during Solar Flares, *Astrophys. J.*, *306*: 710, doi:10.1086/164381.

Dempers, N., and N. E. Engelbrecht, 2020, On the effects of dynamical turbulence on the perpendicular diffusion of low-energy cosmic ray electrons, *Adv. Space Res.*, *65*(8): 2072–2079, doi:10.1016/j.asr.2020.01.040.

Ditlevsen, P. D., 2010, *Turbulence and Shell Models*, Cambridge University Press.

Dunzlaff, P., R. D. Strauss, and M. S. Potgieter, 2015, Solving Parker's transport equation with stochastic differential equations on GPUs, *Comp. Phys. Comm.*, *192*: 156–165, doi: 10.1016/j.cpc.2015.03.008.

Engelbrecht, N. E., On the heliospheric diffusion tensor and its effect on 26-day recurrent cosmic-ray variations, Master's thesis, North-West University (Potchefstroom campus), 2008.

Engelbrecht, N. E., On the development and applications of a three-dimensional ab initio cosmic-ray modulation model, Ph.D. thesis, North-West University (Potchefstroom campus), 2013.

Engelbrecht, N. E., 2019, The Implications of Simple Estimates of the 2D Outerscale Based on Measurements of Magnetic Islands for the Modulation of Galactic Cosmic-Ray Electrons, *Astrophys. J.*, *872*(2), 124, doi:10.3847/1538-4357/aafe7f.

Engelbrecht, N. E., and R. A. Burger, 2013, An Ab Initio Model for Cosmic-ray Modulation, *Astrophys. J.*, *772*(1), 46, doi:10.1088/0004-637X/772/1/46.

Engelbrecht, N. E., and R. A. Burger, 2015a, A comparison of turbulence-reduced drift coefficients of importance for the modulation of galactic cosmic-ray protons in the supersonic solar wind, *Adv. Space Res.*, *55*(1): 390–400, doi:10.1016/j.asr.2014.09.019.

Engelbrecht, N. E., and R. A. Burger, 2015b, Sensitivity of Cosmic-Ray Proton Spectra to the Low-wavenumber Behavior of the 2D Turbulence Power Spectrum, *Astrophys. J.*, *814*(2), 152, doi:10.1088/0004-637X/814/2/152.

Engelbrecht, N. E., and R. D. Strauss, 2018, A Tractable Estimate for the Dissipation Range Onset Wavenumber Throughout the Heliosphere, *Astrophys. J.*, *856*(2), 159, doi:10.3847/1538-4357/aab495.

Engelbrecht, N. E., and C. P. Wolmarans, 2020, Towards a deeper understanding of historic cosmic ray modulation during solar cycle 20, *Adv. Space Res.*, *66*(11): 2722–2732, doi: 10.1016/j.asr.2020.09.022.

Engelbrecht, N. E., R. D. Strauss, J. A. le Roux, and R. A. Burger, 2017, Toward a Greater Understanding of the Reduction of Drift Coefficients in the Presence of Turbulence, *Astrophys. J.*, *841*(2), 107, doi:10.3847/1538-4357/aa7058.

Engelbrecht, N. E., S. T. Mohlolo, and S. E. S. Ferreira, 2019, An Improved Treatment of Neutral Sheet Drift in the Inner Heliosphere, *Astrophys. J. Lett.*, *884*(2), L54, doi: 10.3847/2041-8213/ab4ad6.

Exarhos, G., and X. Moussas, 1999, Time variations of the Magnetic Field at the Heliospheric Termination Shock - Galactic Cosmic-Ray modulation, *Solar Phys.*, *187*(1): 157–175, doi: 10.1023/A:1005184531882.

Ferreira, S. E. S., M. S. Potgieter, R. A. Burger, B. Heber, and H. Fichtner, 2001, Modulation of Jovian and galactic electrons in the heliosphere: 1. Latitudinal transport of a few MeV electrons, *J. Geophys. Res.*, *106*: 24,979–24,987.

Fisk, L. A., 1996, Motion of the footpoints of heliospheric magnetic field lines at the Sun: Implications for recurrent energetic particle events at high heliographic latitudes, *J. Geophys. Res.*, *101*(A7): 15,547–15,554, doi:10.1029/96JA01005.

Foias, C., O. Manley, R. M. S. Rosa, and R. Temam, 2001, *Navier-Stokes Equations and Turbulence*, Cambridge University Press.

Forman, M. A., J. R. Jokipii, and A. J. Owens, 1974, Cosmic-Ray Streaming Perpendicular to the Mean Magnetic Field, *Astrophys. J.*, *192*: 535–540, doi:10.1086/153087.

Forsyth, R. J., A. Balogh, E. J. Smith, G. Erdös, and D. J. McComas, 1996, The underlying Parker spiral structure in the Ulysses magnetic field observations, 1990-1994, *J. Geophys. Res.*, *101*(A1): 395–404, doi:10.1029/95JA02977.

Fraternale, F., L. Gallana, M. Iovieno, M. Opher, J. D. Richardson, and D. Tordella, 2016, Turbulence in the solar wind: spectra from Voyager 2 data at 5 AU, *Phys. Scr.*, *91*(2), 023011, doi:10.1088/0031-8949/91/2/023011.

Frisch, U., 1995, *Turbulence*, Cambridge University Press, Cambridge, UK.

Gleeson, L. J., and W. I. Axford, 1968, Solar Modulation of Galactic Cosmic Rays, *Astrophys. J.*, *154*: 1011–1026, doi:10.1086/149822.

Goldstein, M. L., and D. A. Roberts, 1999, Magnetohydrodynamic turbulence in the solar wind, *Phys. Plasmas*, *6*(11): 4154–4160, doi:10.1063/1.873680.

Goldstein, M. L., D. A. Roberts, and W. H. Matthaeus, 1995, Magnetohydrodynamic Turbulence In The Solar Wind, *Ann. Rev. Astron. Astrophys.*, *33*: 283–326, doi:10.1146/annurev.aa.33.090195.001435.

Hale, G. E., 1908, On the probable existence of a magnetic field in sun-spots, *Astrophys. J.*, *28*: 315–343.

Hathaway, D. H., 2015, The Solar Cycle, *Living Rev. Solar Phys.*, *12*(1), 4, doi:10.1007/lrsp-2015-4.

Hatton, C. J., 1980, Solar flares and the cosmic ray intensity, *Solar Phys.*, *66*: 159–165, doi:10.1007/BF00150526.

Hedgecock, P. C., 1975, Measurements of the Interplanetary Magnetic Field in Relation to the Modulation of Cosmic Rays, *Solar Phys.*, *42*(2): 497–527, doi:10.1007/BF00149929.

Hitge, M., and R. A. Burger, 2010, Cosmic ray modulation with a Fisk-type heliospheric magnetic field and a latitude-dependent solar wind speed, *Adv. Space Res.*, *45*(1): 18–27, doi:10.1016/j.asr.2009.07.024.

Hoeksema, J. T., 1992, Large-scale structure of the heliospheric magnetic field - 1976-1991, in *Solar Wind Seven Colloquium*, edited by E. Marsch & R. Schwenn, pp. 191–196.

Huang, Y. X., F. G. Schmitt, Z. M. Lu, P. Fougairolles, Y. Gagne, and Y. L. Liu, 2010, Second-order structure function in fully developed turbulence, *Phys. Rev. E*, *82*(2), 026319, doi:10.1103/PhysRevE.82.026319.

Jokipii, J. R., and J. Kóta, 2000, Galactic and Anomalous Cosmic Rays in the Heliosphere, *Astrophys. Space Sci.*, *274*: 77–96, doi:10.1023/A:1026535603934.

Jokipii, J. R., and B. Thomas, 1981, Effects of drift on the transport of cosmic rays. IV - Modulation by a wavy interplanetary current sheet, *Astrophys. J.*, *243*: 1115–1122, doi: 10.1086/158675.

Kallenrode, M.-B., 2001, *Space physics : an introduction to plasmas and particles in the heliosphere and magnetospheres*, Springer.

King, J. H., and N. E. Papitashvili, 2005, Solar wind spatial scales in and comparisons of hourly Wind and ACE plasma and magnetic field data, *J. Geophys. Res. (Space Physics).*, *110*(A2), A02104, doi:10.1029/2004JA010649.

Knipp, D. J., et al., 2016, The May 1967 great storm and radio disruption event: Extreme space weather and extraordinary responses, *Space Weather*, *14*(9): 614–633, doi:10.1002/2016SW001423.

Kolmogorov, A. N., 1941, Local structure of turbulence in an incompressible viscous fluid at very high Reynolds numbers, *Dokl. Akad. Nauk SSSR*, *30*: 301–305, doi:10.1098/rspa.1991.0075, [Reprinted in Proc. R. Soc. London, Ser. A **434**, 9–13 (1991)].

Kóta, J., 2013, Theory and Modeling of Galactic Cosmic Rays: Trends and Prospects, *Space Sci. Rev.*, *176*(1-4): 391–403, doi:10.1007/s11214-012-9870-8.

Kota, J., and J. R. Jokipii, 1983, Effects of drift on the transport of cosmic rays. VI - A three-dimensional model including diffusion, *Astrophys. J.*, *265*: 573–581, doi:10.1086/160701.

Krüger, T. P. J., The effect of a Fisk-Parker hybrid magnetic field on cosmic rays in the heliosphere, Master's thesis, North-West University, 2005.

Langner, U. W., and M. S. Potgieter, 2004, Solar wind termination shock and heliosheath effects on the modulation of protons and antiprotons, *J. Geophys. Res. (Space Physics).*, *109*(A1), A01103, doi:10.1029/2003JA010158.

Le Roux, J. A., and M. S. Potgieter, 1995, The Simulation of Complete 11 and 22 Year Modulation Cycles for Cosmic Rays in the Heliosphere Using a Drift Model with Global Merged Interaction Regions, *Astrophys. J.*, *442*: 847–851, doi:10.1086/175487.

Leamon, R. J., W. H. Matthaeus, C. W. Smith, G. P. Zank, D. J. Mullan, and S. Oughton, 2000, MHD-driven Kinetic Dissipation in the Solar Wind and Corona, *Astrophys. J.*, *537*: 1054–1062, doi:10.1086/309059.

Lin, S.-J., X.-J. Bi, and P.-F. Yin, 2019, Investigating the dark matter signal in the cosmic ray antiproton flux with the machine learning method, *Phys. Rev. D*, *100*(10), 103014, doi:10.1103/PhysRevD.100.103014.

Lindgren, S. T., 1968, The Solar Particle Events of May 23 and May 28, 1967, *Solar Phys.*, *5*(3): 382–409, doi:10.1007/BF00147152.

Lockwood, J. A., and W. R. Webber, 1979, Cosmic ray modulation during solar activity cycle 20, *J. Geophys. Res.*, *84*(A1): 120–124, doi:10.1029/JA084iA01p00120.

Manuel, R., Time-dependent modulation of cosmic rays in the outer heliosphere, Ph.D. thesis, North-West University (Potchefstroom campus), 2013.

Manuel, R., S. E. S. Ferreira, and M. S. Potgieter, 2014, Time-Dependent Modulation of Cosmic Rays in the Heliosphere, *Solar Phys.*, *289*(6): 2207–2231, doi:10.1007/s11207-013-0445-y.

Matthaeus, W. H., and M. L. Goldstein, 1982, Measurement of the rugged invariants of magnetohydrodynamic turbulence in the solar wind, *J. Geophys. Res.*, *87*(A8): 6011–6028, doi:10.1029/JA087iA08p06011.

Matthaeus, W. H., and M. Velli, 2011, Who needs turbulence?, *Space Sci. Rev.*, *160*: 145–168, doi:10.1007/s11214-011-9793-9.

Matthaeus, W. H., M. L. Goldstein, and J. H. King, 1986, An interplanetary magnetic field ensemble at 1 AU, *J. Geophys. Res.*, *91*(A1): 59–69, doi:10.1029/JA091iA01p00059.

Matthaeus, W. H., M. L. Goldstein, and D. A. Roberts, 1990, Evidence for the presence of quasi-two-dimensional nearly incompressible fluctuations in the solar wind, *J. Geophys. Res.*, *95*: 20,673–20,683, doi:10.1029/JA095iA12p20673.

Matthaeus, W. H., C. W. Smith, and J. W. Bieber, 1999, Correlation lengths, the ultra-scale and the spatial structure of interplanetary turbulence, in *Solar Wind Nine*, vol. 511, edited by S. Habbal, R. Esser, J. V. Hollweg, and P. A. Isenberg, AIP, Woodbury, NY.

Matthaeus, W. H., G. Qin, J. W. Bieber, and G. P. Zank, 2003, Nonlinear Collisionless Perpendicular Diffusion of Charged Particles, *Astrophys. J. Lett.*, *590*(1): L53–L56, doi: 10.1086/376613.

Matthaeus, W. H., S. Dasso, J. M. Weygand, L. J. Milano, C. W. Smith, and M. G. Kivelson, 2005, Spatial correlation of solar-wind turbulence from two-point measurements, *Phys. Rev. Lett.*, *95*: 231,101, doi:10.1103/PhysRevLett.95.231101.

Matthaeus, W. H., J. W. Bieber, D. Ruffolo, P. Chuychai, and J. Minnie, 2007a, Spectral Properties and Length Scales of Two-dimensional Magnetic Field Models, *Astrophys. J.*, *667*(2): 956–962, doi:10.1086/520924.

Matthaeus, W. H., B. Breech, P. Dmitruk, A. Bemporad, G. Poletto, M. Velli, and M. Romoli, 2007b, Density and Magnetic Field Signatures of Interplanetary 1/f Noise, *Astrophys. J. Lett.*, *657*(2): L121–L124, doi:10.1086/513075.

Matthaeus, W. H., D. C. Montgomery, M. Wan, and S. Servidio, 2012, A review of relaxation and structure in some turbulent plasmas: magnetohydrodynamics and related models, *J. Turb.*, *13*(1), 37, doi:10.1080/14685248.2012.704378.

McComas, D. J., et al., 1998, Ulysses' return to the slow solar wind, *Geophys. Res. Lett.*, *25*: 1–4.

McComas, D. J., et al., 2000, Solar wind observations over Ulysses' first full polar orbit, *J. Geophys. Res.*, *105*: 10 419–10 434.

McDonald, F. B., H. Moraal, J. P. L. Reinecke, N. Lal, and R. E. McGuire, 1992, The Cosmic Radiation in the Heliosphere at Successive Solar Minima, *J. Geophys. Res.*, *97*(A2): 1557–1570, doi:10.1029/91JA02389.

McDonough, J. M., 2007, Introductory lectures on turbulence: physics, mathematics and modeling.

Meyer-Vernet, N., 2007, *Basics of the Solar of the Wind*, Cambridge University Press.

Minnie, J., J. W. Bieber, W. H. Matthaeus, and R. A. Burger, 2007a, On the Ability of Different Diffusion Theories to Account for Directly Simulated Diffusion Coefficients, *Astrophys. J.*, *663*(2): 1049–1054, doi:10.1086/518765.

Minnie, J., J. W. Bieber, W. H. Matthaeus, and R. A. Burger, 2007b, Suppression of Particle Drifts by Turbulence, *Astrophys. J.*, *670*(2): 1149–1158, doi:10.1086/522026.

Moloto, K. D., The effect of the heliospheric current sheet on cosmic-ray modulation, Ph.D. thesis, North-West University (South Africa), Potchefstroom Campus, 2015.

Moloto, K. D., and N. E. Engelbrecht, 2020, A Fully Time-dependent Ab Initio Cosmic-Ray Modulation Model Applied to Historical Cosmic-Ray Modulation, *Astrophys. J.*, *894*(2), 121, doi:10.3847/1538-4357/ab87a2.

Moloto, K. D., N. E. Engelbrecht, and R. A. Burger, 2018, A Simplified Ab Initio Cosmic-ray Modulation Model with Simulated Time Dependence and Predictive Capability, *Astrophys. J.*, *859*(2), 107, doi:10.3847/1538-4357/aac174.

Moloto, K. D., N. E. Engelbrecht, R. D. Strauss, D. M. Moeketsi, and J. P. van den Berg, 2019, Numerical integration of stochastic differential equations: A parallel cosmic ray modulation implementation on Africa's fastest computer, *Adv. Space Res.*, *63*(1): 626–639, doi:10.1016/j.asr.2018.08.048.

Moraal, H., 2013, Cosmic-Ray Modulation Equations, *Space Sci. Rev.*, *176*(1-4): 299–319, doi:10.1007/s11214-011-9819-3.

Nel, A., The solar-cycle dependence of the heliospheric diffusion tensor, Master's thesis, North-West University, 2015.

Opher, M., 2016, The Heliosphere: What Did We Learn in Recent Years and the Current Challenges, *Space Sci. Rev.*, *200*(1-4): 475–494, doi:10.1007/s11214-015-0186-3.

Opher, M., A. Loeb, J. Drake, and G. Toth, 2020, A small and round heliosphere suggested by magnetohydrodynamic modelling of pick-up ions, *Nat. Astron.*, *4*: 675–683, doi:10.1038/s41550-020-1036-0.

Oughton, S., P. Dmitruk, and W. H. Matthaeus, 2006, A two-component phenomenology for homogeneous magnetohydrodynamic turbulence, *Phys. Plasmas*, *13*(4): 042,306–042,306, doi:10.1063/1.2188088.

Oughton, S., W. H. Matthaeus, C. W. Smith, B. Breech, and P. A. Isenberg, 2011, Transport of solar wind fluctuations: A two-component model, *J. Geophys. Res. (Space Physics).*, *116*(A8), A08105, doi:10.1029/2010JA016365.

Oughton, S., W. H. Matthaeus, M. Wan, and K. T. Osman, 2015, Anisotropy in solar wind plasma turbulence, *Phil. Trans. R. Soc. A*, *373*(2041): 20140,152–20140,152, doi:10.1098/rsta.2014.0152.

Owens, M., and R. Forsyth, 2013, The heliospheric magnetic field, *Living Rev. Solar Phys.*, *10*(1): 5, doi:https://doi.org/10.12942/lrsp-2013-510.12942/lrsp-2013-5.

Palmer, I. D., 1982, Transport coefficients of low-energy cosmic rays in interplanetary space, *Rev. Geophys. Space Phys.*, *20*: 335–351, doi:10.1029/RG020i002p00335.

Parker, E. N., 1958, Dynamics of the interplanetary gas and magnetic fields, *Astrophys. J.*, *128*: 664–676.

Parker, E. N., 1965, The passage of energetic charged particles through interplanetary space, *Planet. Space Sci.*, *13*(1): 9–49, doi:10.1016/0032-0633(65)90131-5.

Pei, C., J. W. Bieber, R. A. Burger, and J. Clem, 2010, A general time-dependent stochastic method for solving Parker's transport equation in spherical coordinates, *J. Geophys. Res. (Space Physics).*, *115*(A12), A12107, doi:10.1029/2010JA015721.

Phillips, J. L., et al., 1995, Ulysses solar wind plasma observations from pole to pole, *Geophys. Res. Lett.*, *22*(23): 3301–3304, doi:10.1029/95GL03094.

Pierce, J. R., 2017, Cosmic rays, aerosols, clouds, and climate: Recent findings from the CLOUD experiment, *J. Geophys. Res. (Atmospheres).*, *122*(15): 8051–8055, doi:10.1002/2017JD027475.

Pogorelov, N. V., et al., 2017, Heliosheath Processes and the Structure of the Heliopause: Modeling Energetic Particles, Cosmic Rays, and Magnetic Fields, *Space Sci. Rev.*, *212*(1-2): 193–248, doi:10.1007/s11214-017-0354-8.

Potgieter, M., S. Ferreira, and D. Toit Strauss, 2011, Galactic Cosmic Rays in the Dynamic Heliosphere, in *Cosmic Rays for Particle and Astroparticle Physics*, edited by S. Giani, C. Leroy, and P. G. Rancoita, pp. 441–453, doi:10.1142/9789814329033_0055.

Potgieter, M. S., 2014, The charge-sign dependent effect in the solar modulation of cosmic rays, *Adv. Space Res.*, *53*(10): 1415–1425, doi:10.1016/j.asr.2013.04.015.

Potgieter, M. S., and S. E. S. Ferreira, 2001, Modulation of cosmic rays in the heliosphere over 11 and 22 year cycles: a modelling perspective, *Adv. Space Res.*, *27*(3): 481–492, doi:10.1016/S0273-1177(01)00080-1.

Potgieter, M. S., and J. A. Le Roux, 1994, The Long-Term Heliospheric Modulation of Galactic Cosmic Rays according to a Time-dependent Drift Model with Merged Interaction Regions, *Astrophys. J.*, *423*: 817, doi:10.1086/173860.

Potgieter, M. S., R. A. Burger, and S. E. S. Ferreira, 2001, Modulation of Cosmic Rays in the Heliosphere From Solar Minimum to Maximum: a Theoretical Perspective, *Space Sci. Rev.*, *97*: 295–307, doi:10.1023/A:1011837303094.

Potgieter, M. S., E. E. Vos, M. Boezio, N. De Simone, V. Di Felice, and V. Formato, 2014, Modulation of Galactic Protons in the Heliosphere During the Unusual Solar Minimum of 2006 to 2009, *Solar Phys.*, *289*: 391–406, doi:10.1007/s11207-013-0324-6.

Qin, G., and Z. N. Shen, 2017, Modulation of Galactic Cosmic Rays in the Inner Heliosphere, Comparing with PAMELA Measurements, *Astrophys. J.*, *846*(1), 56, doi:10.3847/1538-4357/aa83ad.

Quenby, J. J., 1984, The Theory of Cosmic-Ray Modulation, *Space Sci. Rev.*, *37*(3-4): 201–267, doi:10.1007/BF00226364.

Raath, J. L., R. D. Strauss, and M. S. Potgieter, 2015, New insights from modeling the neutral heliospheric current sheet, *Astrophys. Space Sci.*, *360*: 56–68, doi:10.1007/s10509-015-2556-4.

Reames, D. V., 2020, Solar Energetic Particles (Second Edition), *arXiv e-prints*, arXiv:2010.08517.

Reinecke, J. P. L., and M. S. Potgieter, 1994, An explanation for the difference in cosmic ray modulation at low and neutron monitor energies during consecutive solar minimum periods, *J. Geophys. Res.*, *99*(A8): 14,761–14,768, doi:10.1029/94JA00792.

Richardson, J. D., and E. C. Stone, 2009, The Solar Wind in the Outer Heliosphere, *Space Sci. Rev.*, *143*(1-4): 7–20, doi:10.1007/s11214-008-9443-z.

Schlickeiser, R., 2002, *Cosmic Ray Astrophysics*, Springer, Berlin.

Schwadron, N. A., 2002, An explanation for strongly underwound magnetic field in co-rotating rarefaction regions and its relationship to footpoint motion on the the sun, *Geophys. Res. Lett.*, *29*(14), 1663, doi:10.1029/2002GL015028.

Schwadron, N. A., A. J. Boyd, K. Kozarev, M. Golightly, H. Spence, L. W. Townsend, and M. Owens, 2010, Galactic cosmic ray radiation hazard in the unusual extended solar minimum between solar cycles 23 and 24, *Space Weather*, *8*(A6), S00E04, doi:10.1029/2010SW000567.

Shalchi, A., 2009, *Nonlinear Cosmic Ray Diffusion Theories, Astrophysics and Space Science Library*, vol. 362, Springer, Berlin, doi:10.1007/978-3-642-00309-7.

Shalchi, A., 2020a, Perpendicular Transport of Energetic Particles in Magnetic Turbulence, *Space Sci. Rev.*, *216*(2), 23, doi:10.1007/s11214-020-0644-4.

Shalchi, A., 2020b, Heuristic Description of Perpendicular Particle Transport in Turbulence with Super-diffusive Magnetic Field Lines, *Astrophys. J.*, *898*(2), 135, doi:10.3847/1538-4357/ab9c1d.

Shalchi, A., J. W. Bieber, and W. H. Matthaeus, 2004, Analytic Forms of the Perpendicular Diffusion Coefficient in Magnetostatic Turbulence, *Astrophys. J.*, *604*(2): 675–686, doi:10.1086/382128.

Shen, Z. N., and G. Qin, 2018, Modulation of Galactic Cosmic Rays in the Inner Heliosphere over Solar Cycles, *Astrophys. J.*, *854*(2), 137, doi:10.3847/1538-4357/aaab64.

Shikaze, Y., et al., 2007, Measurements of 0.2 20 GeV/n cosmic-ray proton and helium spectra from 1997 through 2002 with the BESS spectrometer, *Astropart. Phys.*, *28*(1): 154–167, doi:10.1016/j.astropartphys.2007.05.001.

SILSO World Data Center.

Slavin, J. A., and E. J. Smith, 1983, Solar cycle variations in the interplanetary magnetic field., in *NASA Conference Publication*, *NASA Conference Publication*, vol. 228, p. 0.323.

Smith, C. W., W. H. Matthaeus, G. P. Zank, N. F. Ness, S. Oughton, and J. D. Richardson, 2001, Heating of the low-latitude solar wind by dissipation of turbulent magnetic fluctuations, *J. Geophys. Res.*, *106*(A5): 8253–8272, doi:10.1029/2000JA000366.

Smith, C. W., K. Hamilton, B. J. Vasquez, and R. J. Leamon, 2006, Dependence of the Dissipation Range Spectrum of Interplanetary Magnetic Fluctuationson the Rate of Energy Cascade, *Astrophys. J. Lett.*, *645*(1): L85–L88, doi:10.1086/506151.

Smith, E. J., 2001, The heliospheric current sheet, *J. Geophys. Res.*, *106*(A8): 15,819–15,832, doi:10.1029/2000JA000120.

Steyn, P. J., and R. A. Burger, 2020, A Generalized Fisk-type HMF: Implications of Spatially Dependent Photospheric Differential Rotation, *Astrophys. J.*, *902*(1), 33, doi:10.3847/1538-4357/abb2a5.

Stone, E. C., A. C. Cummings, F. B. McDonald, B. C. Heikkila, N. Lal, and W. R. Webber, 2013, Voyager 1 Observes Low-Energy Galactic Cosmic Rays in a Region Depleted of Heliospheric Ions, *Science*, *341*(6142): 150–153, doi:10.1126/science.1236408.

Strauss, R. D., M. S. Potgieter, A. Kopp, and I. Büsching, 2011, On the propagation times and energy losses of cosmic rays in the heliosphere, *J. Geophys. Res. (Space Physics).*, *116*(A12), A12105, doi:10.1029/2011JA016831.

Strauss, R. D., M. S. Potgieter, I. Büsching, and A. Kopp, 2012a, Modelling heliospheric current sheet drift in stochastic cosmic ray transport models, *Astrophys. Space Sci.*, *339*(2): 223–236, doi:10.1007/s10509-012-1003-z.

Strauss, R. D., M. S. Potgieter, and S. E. S. Ferreira, 2012b, Modeling ground and space based cosmic ray observations, *Adv. Space Res.*, *49*(2): 392–407, doi:10.1016/j.asr.2011.10.006.

Strauss, R. D., J. A. le Roux, N. E. Engelbrecht, D. Ruffolo, and P. Dunzlaff, 2016, Non-Axisymmetric Perpendicular Diffusion of Charged Particles and their Transport Across Tangential Magnetic Discontinuities, *Astrophys. J.*, *825*(1), 43, doi:10.3847/0004-637X/825/1/43.

Strauss, R. D. T., and F. Effenberger, 2017, A Hitch-hiker's Guide to Stochastic Differential Equations. Solution Methods for Energetic Particle Transport in Space Physics and Astrophysics, *Space Sci. Rev.*, *212*(1-2): 151–192, doi:10.1007/s11214-017-0351-y.

Strauss, R. D. T., N. Dresing, and N. E. Engelbrecht, 2017, Perpendicular Diffusion of Solar Energetic Particles: Model Results and Implications for Electrons, *Astrophys. J.*, *837*(1), 43, doi:10.3847/1538-4357/aa5df5.

Tautz, R. C., and A. Shalchi, 2012, Drift Coefficients of Charged Particles in Turbulent Magnetic Fields, *Astrophys. J.*, *744*(2), 125, doi:10.1088/0004-637X/744/2/125.

Teufel, A., and R. Schlickeiser, 2003, Analytic calculation of the parallel mean free path of heliospheric cosmic rays. II. Dynamical magnetic slab turbulence and random sweeping slab turbulence with finite wave power at small wavenumbers, *Astron. Astrophys.*, *397*: 15–25, doi:10.1051/0004-6361:20021471.

Vogt, A., B. Heber, A. Kopp, M. S. Potgieter, and R. D. Strauss, 2018, Jovian electrons in the inner heliosphere. Proposing a new source spectrum based on 30 years of measurements, *Astron. Astrophys.*, *613*, A28, doi:10.1051/0004-6361/201731736.

Washimi, H., T. Tanaka, and G. P. Zank, 2017, Time-varying Heliospheric Distance to the Heliopause, *Astrophys. J. Lett.*, *846*(1), L9, doi:10.3847/2041-8213/aa8556.

Wawrzynczak, A., R. Modzelewska, and A. Gil, 2015, A stochastic method of solution of the Parker transport equation, in *J. Phys.: Conf. Ser.*, vol. 632, p. 012084, doi:10.1088/1742-6596/632/1/012084.

Webber, W. R., A. C. Cummings, F. B. McDonald, E. C. Stone, B. Heikkila, and N. Lal, 2008, Galactic cosmic ray H and He nuclei energy spectra measured by Voyagers 1 and 2 near the heliospheric termination shock in positive and negative solar magnetic polarity cycles, *J. Geophys. Res.*, *113*(A10), A10108, doi:10.1029/2008JA013395.

Weygand, J. M., W. H. Matthaeus, S. Dasso, and M. G. Kivelson, 2011, Correlation and Taylor scale variability in the interplanetary magnetic field fluctuations as a function of solar wind speed, *J. Geophys. Res. (Space Physics).*, *116*(A8): A08,102, doi:10.1029/2011JA016621.

Wibberenz, G., I. G. Richardson, and H. V. Cane, 2002, A simple concept for modeling cosmic ray modulation in the inner heliosphere during solar cycles 20-23, *J. Geophys. Res. (Space Physics).*, *107*(A11), 1353, doi:10.1029/2002JA009461.

Wicks, R. T., M. J. Owens, and T. S. Horbury, 2010, The Variation of Solar Wind Correlation Lengths Over Three Solar Cycles, *Solar Phys.*, *262*(1): 191–198, doi:10.1007/s11207-010-9509-4.

Wiengarten, T., S. Oughton, N. E. Engelbrecht, H. Fichtner, J. Kleimann, and K. Scherer, 2016, A Generalized Two-component Model of Solar Wind Turbulence and ab initio Diffusion Mean-Free Paths and Drift Lengthscales of Cosmic Rays, *Astrophys. J.*, *833*(1), 17, doi:10.3847/0004-637X/833/1/17.

Yamada, Y., S. Yanagita, and T. Yoshida, 1998, A stochastic view of the solar modulation phenomena of cosmic rays, *Geophys. Res. Lett.*, *25*(13): 2353–2356, doi:10.1029/98GL51869.

Zank, G. P., 2014, Transport Processes in Space Physics and Astrophysics, *877*, doi:10.1007/978-1-4614-8480-6.

Zank, G. P., W. H. Matthaeus, and C. W. Smith, 1996, Evolution of turbulent magnetic fluctuation power with heliospheric distance, *J. Geophys. Res.*, *101*(A8): 17,093–17,108, doi:10.1029/96JA01275.

Zank, G. P., W. H. Matthaeus, J. W. Bieber, and H. Moraal, 1998, The radial and latitudinal dependence of the cosmic ray diffusion tensor in the heliosphere, *J. Geophys. Res.*, *103*(A2): 2085–2098, doi:10.1029/97JA03013.

Zank, G. P., G. Li, V. Florinski, W. H. Matthaeus, G. M. Webb, and J. A. Le Roux, 2004, Perpendicular diffusion coefficient for charged particles of arbitrary energy, *J. Geophys. Res.*, *109*(A4), A04107, doi:10.1029/2003JA010301.

Zank, G. P., L. Adhikari, P. Hunana, S. K. Tiwari, R. Moore, D. Shiota, R. Bruno, and D. Telloni, 2018, Theory and transport of nearly incompressible magnetohydrodynamic turbulence. IV. Solar coronal turbulence, *Astrophys. J.*, *854*: 32, doi:10.3847/1538-4357/aaa763.

Zhang, M., 1999, A Markov Stochastic Process Theory of Cosmic-Ray Modulation, *Astrophys. J.*, *513*(1): 409–420, doi:10.1086/306857.

Zhao, L. L., L. Adhikari, G. P. Zank, Q. Hu, and X. S. Feng, 2018, Influence of the Solar Cycle on Turbulence Properties and Cosmic-Ray Diffusion, *Astrophys. J.*, *856*(2), 94, doi:10.3847/1538-4357/aab362.